Primal-dual active set methods for Allen-Cahn variational inequalities

Lavinia Sarbu

Thesis submitted for the degree of Doctor of Philosophy

University of Sussex

July 2010

Declaration

I hereby declare that this thesis has not been and will not be submitted in whole or in part to another University for the award of any other degree.

Signature:

Acknowledgments

It would not have been possible to write this thesis without the help and support of the kind people around me.

First and foremost, I owe my deepest gratitude to my supervisor, Dr. Vanessa Styles, who supported me throughout my thesis with her knowledge, patience and encouragement. Without her this thesis would not have been possible. One simply could not wish for a better or kinder supervisor.

I would like to thank my collaborators and advisors, Prof. Luise Blank, Prof. Harald Garcke and Dr. Martin Stoll, who helped me with insightful ideas and valuable suggestions in numerous discussions. I was very fortunate to receive their support and guidance during my research.

Many thanks to Raquel and Mel who I shared an office with at different times during my PhD. It was great to have such nice people around me. I also want to thank my other colleagues, especially Adrian, Daniela, James, and Tristan, and all the other faculty members who helped creating a nice and warm working atmosphere. Special thanks also to the support staff for their constant assistance and help.

This work was funded by the Department of Mathematics through a Graduate Teaching Assistantship. This grant also gave me the opportunity to travel to conferences and more importantly it allowed me to focus on my research.

I would also like to thank all my friends and housemates who have made my time in Brighton such an enjoyable and memorable experience. Special thanks to my dear friends Hannah, Liz, Matt, and Ryan for all the fun times we had and for keeping me sane whilst writing this thesis. I am also grateful to my loyal friends back home in Germany.

My deepest debt of gratitude is to my parents for their unlimited love and support. They encouraged me throughout the years of my study.

Primal-dual active set methods for Allen-Cahn variational inequalities

Lavinia Sarbu

Submitted for the degree of Doctor of Philosophy
University of Sussex, July 2010

Abstract

This thesis aims to introduce and analyse a primal-dual active set strategy for solving Allen-Cahn variational inequalities. We consider the standard Allen-Cahn equation with non-local constraints and a vector-valued Allen-Cahn equation with and without non-local constraints. Existence and uniqueness results are derived in a formulation involving Lagrange multipliers for local and non-local constraints. Local Convergence is shown by interpreting the primal-dual active set approach as a semi-smooth Newton method. Properties of the method are discussed and several numerical simulations in two and three space dimensions demonstrate its efficiency.

In the second part of the thesis various applications of the Allen-Cahn equation are discussed. The non-local Allen-Cahn equation can be coupled with an elasticity equation to solve problems in structural topology optimisation. The model can be extended to handle multiple structures by using the vector-valued Allen-Cahn variational inequality with non-local constraints. Since many applications of the Allen-Cahn equation involve evolution of interfaces in materials an important extension of the standard Allen-Cahn model is to allow materials to exhibit anisotropic behaviour. We introduce an anisotropic version of the Allen-Cahn variational inequality and we show that it is possible to apply the primal-dual active set strategy efficiently to this model. Finally, the Allen-Cahn model is applied to problems in image processing, such as segmentation, denoising and inpainting.

The primal-dual active set method proves flexible and reliable for all the applications considered in this thesis.

Contents

List of Tables

List of Figures

Chapter 1

Introduction

The Allen-Cahn equation was introduced by Allen and Cahn [4] to model the motion of antiphase boundaries in crystalline solids. It describes the curvature dependent evolution of an interface separating two bulk regions. More precisely, the interface moves with normal velocity $v = -\kappa$ where κ is the mean curvature, which is defined as the sum of all principle curvatures. Hence, this evolution is referred to as *mean curvature flow*.

Such systems arise naturally in various fields including materials science, image processing, biology and geology. One example in materials science is grain boundary motion [4, 43]. Grain boundaries in alloys are interfaces separating crystals of different phases or crystals of the same phase with differing orientations. Associated with the grain boundary is a surface energy which gives rise to a thermodynamic restoring force. For a constant surface energy density this is simply the surface tension force which is proportional to the mean curvature and hence the resulting evolution is mean curvature flow.

A more recent area where mean curvature flow is used is image processing [32]. An important task in image processing is to extract the contours of the objects in the image. Moreover, it is desirable that during this process noise in the initial image is suppressed. Algorithms based on mean curvature flow can be used for these tasks and they can also be used to progressively modify the contours to a form which is more manageable for pattern recognition and interpretation [44]. Other important applications for mean curvature flow in image processing include image segmentation and inpainting [18, 77].

Mean curvature flow can be coupled to conservation of volume, which can be seen as being equivalent to mass conservation, to model minimal surfaces [57].

There are two main strategies to model mean curvature flow, the so-called 'sharp' and 'diffuse' interface models, see [43] for an overview. Sharp interface models assume the interface to have zero thickness. The interface can be described for example using a parametric equation or as the graph of a function. Diffuse interface

approaches such as the phase field approach model the interface to have a small finite thickness. In this thesis we consider the phase field approach which we will describe in more detail in the next section.

1.1 Phase field model

Let Ω be an open and bounded domain in $\mathbb{R}^d$ and let $\Gamma(t)$ be a hypersurface moving through Ω that separates two bulk regions.
In the phase field model the sharp interface $\Gamma(t)$ is modelled by a diffuse transition layer with width of order ε, where $0 < \varepsilon \ll 1$. An order parameter or phase field function $u : \Omega \times (0,T) \longrightarrow \mathbb{R}$ is introduced which indicates the phase of a material and changes its value rapidly in the transition layer.
The model is based on the non-convex Ginzburg-Landau energy

$$E(u) := \int_\Omega (\tfrac{\gamma\varepsilon}{2}|\nabla u|^2 + \tfrac{\gamma}{\varepsilon}\psi(u))dx \tag{1.1}$$

where $\gamma > 0$ is a parameter related to the interfacial energy. The potential term $\psi : \mathbb{R} \longrightarrow \mathbb{R}_0^+ \cup \{\infty\}$ is assumed to have two global minima at the points -1 and 1 such that the values ± 1 describe the pure phases. Examples are the smooth double well potential $\psi(u) = (1-u^2)^2$ or the double obstacle potential

$$\psi(u) = \begin{cases} \frac{1}{2}(1-u^2) & \text{if} \quad |u| \le 1\,, \\ \infty & \text{if} \quad |u| > 1\,. \end{cases} \tag{1.2}$$

This double obstacle potential was introduced in the gradient theory of phase transitions in [11, 23, 24]. Introducing

$$\psi_0(u) := \tfrac{1}{2}(1-u^2)$$

and the indicator function

$$I_{[-1,1]}(u) := \begin{cases} 0 & \text{if} \quad |u| \le 1\,, \\ \infty & \text{if} \quad |u| > 1\,, \end{cases}$$

we can rewrite (1.2) as

$$\psi(u) = \psi_0(u) + I_{[-1,1]}(u)\,. \tag{1.3}$$

In order to have $E(u)$ of moderate size u favours the values ± 1 due to the potential

function. On the other hand given the gradient term $\int_\Omega |\nabla u|^2$, oscillations between the values ± 1 are energetically not favourable.
Given an initial phase distribution $u(.,0) = u_0 : \Omega \to \mathbb{R}$ at time $t = 0$ the interface motion can be modelled by the steepest descent of E with respect to the L^2–norm which results in the Allen-Cahn equation [112]. In the case of a smooth potential ψ we obtain, after a suitable rescaling of time,

$$\varepsilon \partial_t u = \gamma \varepsilon \Delta u - \tfrac{\gamma}{\varepsilon} \psi'(u) \quad \text{for } x \in \Omega \text{ and } t > 0$$

together with Neumann boundary conditions $\frac{\partial u}{\partial \nu} = 0$ on $\partial\Omega$, where ν is the outer unit normal to Ω. If ψ has the form (1.3) we obtain, see [25],

$$\varepsilon(\partial_t u, \chi - u) + \gamma\varepsilon(\nabla u, \nabla(\chi - u)) + \tfrac{\gamma}{\varepsilon}(\psi_0'(u), \chi - u) \geq 0 \tag{1.4}$$

which has to hold for almost all t and all $\chi \in H^1(\Omega)$ with $|\chi| \leq 1$. Here and in what follows $(f, g) := \int_\Omega f(x)g(x)\,dx$ with $f, g \in L^2(\Omega)$ denotes the L^2–inner product.
Often we consider systems in which the total spatial amount of the phases are conserved. In this case we study the steepest descent of E under the constraint $\fint_\Omega u dx = m$ where $m \in (-1, 1)$ is a fixed number and $\fint_\Omega f(x)dx := \frac{1}{|\Omega|}\int_\Omega f(x)dx$ with $|\Omega|$ being the Lebesgue measure of Ω. In the case of a smooth potential ψ we obtain (see [112, 57])

$$\varepsilon \partial_t u = \gamma \varepsilon \Delta u - \tfrac{\gamma}{\varepsilon} \psi'(u) + \tfrac{\gamma}{\varepsilon} \fint_\Omega \psi'(u) dx\,.$$

Assuming homogeneous Neumann boundary conditions it follows that

$$\tfrac{d}{dt}\int_\Omega u dx = 0 \quad \text{and} \quad \tfrac{d}{dt} E(u) \leq 0\,.$$

In the case of an obstacle potential we need to solve, for given initial data $u_0 \in H^1(\Omega)$ with $|u_0| \leq 1$ a.e. in Ω, the following problem [25]:

(P_m) Find $u \in H^1(\Omega_T)$ such that $\fint_\Omega u(x,t)dx = m$, $u(.,0) = u_0$, $|u| \leq 1$ a.e. in $\Omega_T := \Omega \times (0,T)$ and

$$\varepsilon(\partial_t u, \chi - u) + \gamma\varepsilon(\nabla u, \nabla(\chi - u)) + \tfrac{\gamma}{\varepsilon}(\psi_0'(u), \chi - u) \geq 0 \tag{1.5}$$

which has to hold for almost all t and all $\chi \in H^1(\Omega)$ with $|\chi| \leq 1$ and $\fint_\Omega \chi = m$.

1.2 Numerical methods for the Allen-Cahn equation

Most of the existing literature [45, 59, 81, 95] concentrates up to now on the explicit and semi-implicit time discretisation of the Allen-Cahn equation. For the discretisation in space either finite differences or finite elements are used [31, 39, 43]. More recently research focuses on the double obstacle since the order parameter is strictly 1 or -1 in the bulk regions and this can be used to reduce computation times.

One standard approach uses that the fully discrete variational inequality (1.4) satisfies a minimum principle and hence the solution in the new time step can be computed by first calculating a $\tilde{u}^{n+1}$ and then projecting componentwise onto the interval $[-1, 1]$ [48, 113]. For an implicit discretisation in time a projected SOR algorithm can be used [48, 43]. Due to its simplicity this approach has been widely used.

For explicit time discretisations it is known [43] that the interface cannot move more than one element per time step, thus it is only necessary to compute the order parameter u on the closure of the transition layer. This has been exploited in the dynamic mesh algorithm by Nochetto, Paolini and Verdi [95]. They carry a mesh only in the transition layer and add or remove triangles where necessary. Elliott and Gardiner [46] use a similar technique for their 'mask' method where they use a fixed mesh but only compute nodal values of u on the transition layer. For uniform meshes, where stiffness and mass matrices require minimal storage, this method proves very efficient. However, the explicit time discretisation has the usual stability restriction for parabolic problems, $\tau \leq Ch^2$, where τ denotes the time step and h the mesh size [101].

There are a variety of other numerical methods. Kornhuber [82, 83] used monotone multigrid methods to solve elliptic variational inequalities arising from obstacle problems. The monotone multigrid algorithm is based on a subspace correction approach where the subspace is decomposed into smaller spaces, which leads to a polygonal Gauss-Seidel relaxation as the fine grid smoother. This idea has been extended for the vector-valued Allen-Cahn equation [84]. A review on various multigrid methods for obstacle problems can be found in [66]. A new approach by Gräser [65] uses a non-smooth Newton method which is based on the formulation of the problem as an unconstrained minimisation problem. This strategy is applicable for more general set-valued saddle point problems, see [67].

So far there are no computational comparisons between these various methods available. It would be of great interest to compare our primal-dual active set method to the multigrid methods used by Kornhuber [84, 67].

For the non-local Allen-Cahn variational inequality so far only explicit methods have

been used, see [25, 57].
In this work we focus on implicit discretisations in time which allow much larger time steps than explicit discretisations. The Allen-Cahn variational inequality can be interpreted as the first order optimality condition of a minimisation problem. Active set methods have widely been used in optimisation and optimal control. We use the primal-dual active set method introduced by Bergounioux, Ito and Kunisch [15]. This method has been shown to be equivalent to a semi-smooth Newton method [72] which we exploit to show local convergence.

1.3 Outline of the thesis

In Chapter 2 we introduce a Lagrange multiplier method to handle the inequality constraint $|u| \leq 1$ and the volume constraint $\fint_\Omega u = m$ and we reformulate the Allen-Cahn variational inequality (1.5) as a complementarity problem. Existence and uniqueness of the solution u and the Lagrange multipliers is shown using a regularisation technique. We discretise in time using backward Euler and in space using finite elements and apply the primal-dual active set method. Interpreting the approach as a semi-smooth Newton method we can show local convergence. We discuss some of the features of the primal-dual active set method and compare numerical results to analytically known solutions.
In Chapter 3 we introduce the (non-local) vector-valued Allen-Cahn equation. Using similar techniques as in Chapter 2 we derive a complementarity formulation for which we can show existence and uniqueness of the solution. We apply the primal-dual active set strategy on the fully discrete problem. Using problems where the analytical solution is known we show the efficiency and accuracy of our method. Further simulations illustrate the flexibility of our method by considering more complex processes, such as soap bubble configurations and grain growth.
Since the main computational effort of the primal-dual active set method lies in solving a linear system we focus on efficient solvers in Chapter 4. We consider various linear algebra solvers and discuss their advantages and disadvantages. We also investigate preconditioning for the linear systems.
In Chapter 5 we discuss some applications of Allen-Cahn variational inequalities. First we use the non-local Allen-Cahn equation to solve problems in structural topology optimisation. Phase field models have successfully been used for this sort of problem, but up to now the fourth order Cahn-Hilliard equation has been used. We demonstrate that a non-local Allen-Cahn variational inequality can be used instead which reduces computational costs and thus makes the phase field approach more efficient. We also show how the model can be extended to handle multiple structures by using the vector-valued non-local Allen-Cahn. Since in many applications

the materials under consideration are anisotropic, we apply the primal-dual active set strategy to the anisotropic Allen-Cahn equation and we present some numerical simulations in two and three space dimensions. Finally, we discuss some examples from image processing. We use the vector-valued Allen-Cahn equation for image segmentation of grayscale and colour images. We also look at image inpainting where we replace the Cahn-Hilliard equation, that has been widely used, by a non-local Allen-Cahn equation.

We conclude with Chapter 6 where we briefly summarise our main results and discuss some possible areas of further research.

Chapter 2

Allen-Cahn variational inequality with non-local constraints

In this chapter we focus on developing an algorithm to solve the Allen-Cahn variational inequality (1.5). First, we reformulate the problem with the help of Lagrange multipliers corresponding to the inequality and equality constraints. We show existence and uniqueness of the solution and the Lagrange multipliers and we introduce a primal-dual active set strategy which is then applied to the discrete problem. We demonstrate the efficiency and accuracy of the method using problems where the analytical solution is known and we show numerically that the method is mesh independent.

2.1 Formulation as a complementarity problem

As a first step we reformulate the problem (P_m) on page 3 in the following lemma with the help of Lagrange multipliers μ_+ and μ_- corresponding to the inequality constraints $u \leq 1$ and $u \geq -1$ and a Lagrange multiplier λ corresponding to the constraint $\fint_\Omega u dx = m := \fint_\Omega u_0 dx$.
As a general assumption we require:

$(\mathcal{A}_m)$ *The domain $\Omega \subset \mathbb{R}^d$ is bounded and either convex or has a $C^{1,1}$-boundary. Furthermore the initial data $u_0 \in H^1(\Omega)$ fulfil $|u_0| \leq 1$ a.e. and $\fint_\Omega u_0 = m$ for a given $m \in (-1, 1)$.*

Lemma 2.1.1. *Let $T > 0$ be a positive time and let the assumptions $(\mathcal{A}_m)$ hold. A function $u \in L^2(0, T; H^2(\Omega)) \cap H^1(\Omega_T)$ solves (1.5), if there exists $\mu_+, \mu_- \in L^2(\Omega_T)$*

and $\lambda \in L^2(0,T)$ *such that*

$$\lambda = \varepsilon^2 \partial_t u - \gamma\varepsilon^2 \Delta u + \gamma \psi_0'(u) + \mu_+ - \mu_- \quad \text{a.e. in } \Omega_T\,, \tag{2.1}$$

$$u(0) = u_0,\ \frac{\partial u}{\partial \nu} = 0 \quad \text{a.e. on } (\partial\Omega)_T := \partial\Omega \times (0,T)\,, \tag{2.2}$$

$$\fint_\Omega u dx = m \quad \text{for almost all } t \in [0,T]\,, \tag{2.3}$$

$$|u| \le 1 \quad \text{a.e. in } \Omega_T\,, \tag{2.4}$$

$$\mu_+(u-1) = 0,\ \mu_-(u+1) = 0 \quad \text{a.e. in } \Omega_T\,, \tag{2.5}$$

$$\mu_+ \ge 0, \mu_- \ge 0 \quad \text{a.e. in } \Omega_T\,. \tag{2.6}$$

Proof: Let $\eta \in H^1(\Omega)$ be such that $|\eta| \le 1$ a.e. in Ω and $\fint_\Omega \eta = m$. Testing (2.1) with $(\eta - u)$ gives

$$0 = \int_\Omega (\varepsilon^2 \partial_t u - \varepsilon^2 \gamma \Delta u + \gamma \psi_0'(u))(\eta - u) + \int_\Omega \mu_+(\eta - u) - \int_\Omega \mu_-(\eta - u)$$

for almost every $t \in (0,T)$. Using the properties of η and (2.5)-(2.6) gives for almost all $t \in (0,T)$

$$\mu_+(\eta - u) \le 0,\ \mu_-(\eta - u) \ge 0 \quad \text{a.e. in } \Omega\,.$$

After integration by parts in space and dividing by $\varepsilon > 0$ we obtain

$$0 \le \int_\Omega (\varepsilon \partial_t u + \tfrac{\gamma}{\varepsilon} \psi_0'(u))(\eta - u) + \gamma\varepsilon \int_\Omega \nabla u \cdot \nabla(\eta - u)$$

for almost all $t \in (0,T)$ which is precisely (1.5).

□

2.2 Existence and uniqueness

The primal-dual active set method that we propose will heavily depend on the Lagrange multipliers μ_-, μ_+, λ. Hence we show the existence of a solution u to the system (2.1)-(2.6) together with unique Lagrange multipliers μ_-, μ_+ and λ. In the proof of the existence theorem we handle the linear equality constraint $\fint_\Omega u = m$ by projection and use a penalty approach for the inequality constraint $|u| \le 1$, see also [7, 23]. In particular we replace the indicator function in ψ by terms penalising deviations of u from the interval $[-1,1]$.

Therefore, we define $\psi_+(z) := \max(z-1,0)^2$, $\psi_-(z) := \min(z+1,0)^2$ for all $z \in \mathbb{R}$ and $\psi_\delta(z) := \psi_0(z) + \frac{1}{\delta}(\psi_+(z) + \psi_-(z)) + 1 \quad$ for $\delta > 0$. For $\delta \in (0,2)$ it can be shown that $\psi_\delta''(z) \ge -1$ and $\psi_\delta(z) \ge 0$, for all $z \in \mathbb{R}$. Note that for $\delta \to 0$ the function

$\psi_\delta - 1$ converges to the double obstacle potential (1.2). We need to add 1 in the definition of ψ_δ in order to insure that $\psi_\delta(z) \geq 0$ for all $z \in \mathbb{R}$.
Now, we consider the L^2–gradient flow of

$$E_\delta(u) := \int_\Omega (\tfrac{\gamma\varepsilon}{2}|\nabla u|^2 + \tfrac{\gamma}{\varepsilon}\psi_\delta(u))dx$$

under the mean value constraint. This leads to the semilinear parabolic equation

$$\varepsilon^2 \partial_t u_\delta = \gamma\varepsilon^2 \Delta u_\delta - \gamma\psi_\delta'(u_\delta) + \fint_\Omega \gamma\psi_\delta'(u_\delta)dx \quad \text{a.e. in } \Omega_T\,, \tag{2.7}$$

$$u_\delta(0) = u_0, \qquad \tfrac{\partial u_\delta}{\partial \nu} = 0 \quad \text{on } (\partial\Omega)_T\,. \tag{2.8}$$

The main challenge is to control approximate versions of the Lagrange multipliers which is non-standard due to the coupling of non-local equality and local inequality constraints.

Theorem 2.2.1. *Let the assumptions $(\mathcal{A}_m)$ hold and let $T > 0$. Then there exists a unique solution $(u, \mu_+, \mu_-, \lambda)$ of (2.1)-(2.6) with the following properties*

$$u \in L^2(0,T;H^2(\Omega)) \cap L^\infty(0,T;H^1(\Omega)) \cap H^1(\Omega_T)\,,$$
$$\mu_+, \mu_- \in L^2(\Omega_T)\,,$$
$$\lambda \in L^2(0,T)\,.$$

Proof: Step 1: Existence of a solution u_δ to (2.7)
We show the existence of a solution u_δ to (2.7), (2.8) by a Galerkin approach, following e.g. Evans [54, Section 7.1]. Since such an approach is standard we only briefly describe the arguments and focus on specific aspects that appear in our case due to the non-local structure. We choose $\{w_j\}_{j\in\mathbb{N}_0}$ to be the eigenfunctions of the operator $-\Delta$ [54, Section 6.5] which can be normalised such that $(w_i, w_j) = \delta_{ij}$. Furthermore, we choose w_0 to be constant. A Galerkin approximation is then given as

$$u^N(x,t) = \sum_{j=0}^{N} c_j^N(t) w_j(x)\,, \tag{2.9}$$

$$\varepsilon^2(\partial_t u^N, w_j) + \gamma\varepsilon^2(\nabla u^N, \nabla w_j) + \gamma(\psi_\delta'(u^N), w_j) = 0 \text{ for } j = 1,\dots,N \text{ and } t \geq 0\,, \tag{2.10}$$

$$c_j^N(0) = (u_0, w_j) \quad \text{for } j = 0,\dots,N\,, \tag{2.11}$$

$$c_0^N(t) = c_0^N(0) \quad \text{for } t \geq 0\,. \tag{2.12}$$

To obtain equations (2.10) and (2.12) we first substitute (2.9) into (2.7) and use the weak formulation. Then noting that for $j = 1, ..., N$ the mean value term vanishes

because the $w_j, j = 1, ..., N$ are orthogonal to constants gives (2.10) and for $j = 0$ the only term that does not vanish is $(\delta_t u^N, w_0)$ which leads to $(c_0^N)'(t) = 0$ and hence (2.12) follows. Standard ODE theory gives local existence up to some time $\tilde{T}$ to the initial value problem (2.9)-(2.12). Multiplying (2.10) by $(c_j^N)'(t)$, summation and integration gives

$$\varepsilon \int_{\Omega_{\tilde{T}}} (\partial_t u^N)^2 + E_\delta(u^N(\tilde{T})) = E_\delta(u^N(0))\,. \tag{2.13}$$

We note that $E_\delta(u^N(0))$ is bounded independent of N since we can use that

$$\|u^N(0)\|_{L^2}^2 \leq \sum_{j=0}^{N} |c_j^N(0)|^2 \|w_j\|_{L^2}^2 = \sum_{j=0}^{N} |(u_0, w_j)|^2 \leq \|u_0\|_{L^2}^2.$$

This energy estimate can be used to show boundedness of the local ODE solution and hence global existence to (2.9)-(2.12) on $[0, T]$.

Step 2: Regularity of a solution u_δ

Standard compactness and regularity arguments, see e.g. Evans [54, Section 7.1], give in the limit $N \to \infty$ the existence of a solution $u_\delta \in L^2(0,T;H^2(\Omega)) \cap H^1(\Omega_T) \cap L^\infty(0,T;H^1(\Omega))$ of (2.7), (2.8) satisfying $\int_\Omega u_\delta(t) = \int_\Omega u_0$ for all $t \in [0,T]$. In particular we obtain

$$\varepsilon \int_{\Omega_T} (\partial_t u_\delta)^2 + E_\delta(u_\delta(T)) \leq E_\delta(u_0) \tag{2.14}$$

for all $\delta > 0$. Since $\psi_\delta'(u_\delta) = -u_\delta + \frac{2}{\delta}\max(u_\delta - 1, 0) + \frac{2}{\delta}\min(u_\delta + 1, 0)$ and $u_\delta \in L^2(0,T;H^2(\Omega))$ it follows in particular that $\psi_\delta'(u_\delta) \in L^2(0,T;H^1(\Omega))$. Hence we can multiply (2.7) by $-\Delta u_\delta$ and integrate by parts to obtain

$$\begin{aligned}\varepsilon^2 \tfrac{d}{dt}\tfrac{1}{2}\int_\Omega |\nabla u_\delta|^2 + \varepsilon^2\gamma\int_\Omega |\Delta u_\delta|^2 + \gamma\int_\Omega \tfrac{1}{\delta}(\psi_+''(u_\delta) + \psi_-''(u_\delta))|\nabla u_\delta|^2 &= -\int_\Omega \gamma\psi_0''(u_\delta)|\nabla u_\delta|^2 \\ &= \int_\Omega \gamma|\nabla u_\delta|^2\,.\end{aligned}$$

Note that $\psi_+''(z) \geq 0$ and $\psi_-''(z) \geq 0$ for all $z \in \mathbb{R}$. Hence, using a Grönwall argument for the inequality

$$\varepsilon^2 \tfrac{d}{dt}\tfrac{1}{2}\int_\Omega |\nabla u_\delta|^2 \leq \int_\Omega \gamma|\nabla u_\delta|^2$$

gives that $\|\nabla u_\delta(t)\|_{L^2} \leq C$ for a.e. $t \in (0,T)$. Using now the Poincaré inequality gives that $(u_\delta)_{\delta\in(0,2)}$ is uniformly bounded in $L^\infty(0,T;H^1(\Omega))$. Furthermore, Δu_δ is uniformly bounded in $L^2(\Omega_T)$. Now elliptic regularity theory [68, Chapter 2] gives that $(u_\delta)_{\delta>0}$ is uniformly bounded in $L^2(0,T;H^2(\Omega)) \cap L^\infty(0,T;H^1(\Omega)) \cap H^1(\Omega_T)$. When passing to the limit in (2.7) we would like to obtain the Lagrange multipliers

$\mu_\pm$ as the limit of $\frac{\gamma}{\delta}\psi_\pm(u_\delta)$ and λ as the limit of $\fint_\Omega \gamma\psi'_\delta(u_\delta)$, as δ tends to zero. To this end we need to estimate

$$\lambda_\delta := \fint_\Omega \gamma\psi'_\delta(u_\delta)dx$$

in $L^2(0,T)$ uniformly in δ.
Step 3: Prove that $\lambda_\delta \in L^2(0,T)$ uniformly for $\delta \in (0,2)$
Multiplying (2.7) by $u_\delta \pm 1$ gives after integration by parts using $\int_\Omega \partial_t u_\delta = 0$ and $\fint_\Omega u_\delta = m$:

$$\int_\Omega \varepsilon^2 \partial_t u_\delta u_\delta + \gamma\varepsilon^2 \int_\Omega |\nabla u_\delta|^2 + \int_\Omega \gamma\psi'_\delta(u_\delta)(u_\delta \pm 1) = \lambda_\delta(m \pm 1)|\Omega| \,. \tag{2.15}$$

Since $\psi''_\delta \geq -1$ we obtain that $\psi_\delta(z) + \frac{1}{2}z^2$ is convex in z which gives that

$$\psi'_\delta(u_\delta)(u_\delta \mp 1) + u_\delta(u_\delta \mp 1) \geq \psi_\delta(u_\delta) - \psi_\delta(\pm 1) + \tfrac{1}{2}u_\delta^2 - \tfrac{1}{2}(\pm 1)^2$$

and hence

$$\psi'_\delta(u_\delta)(u_\delta \mp 1) + \tfrac{1}{2}(u_\delta \mp 1)^2 \geq \psi_\delta(u_\delta) - \psi_\delta(\pm 1) \,. \tag{2.16}$$

We consider now the two identities in (2.15) separately. In the first case we can estimate λ_δ as follows

$$\begin{aligned}
\lambda_\delta &= \tfrac{1}{(m+1)|\Omega|}\left(\int_\Omega \varepsilon^2 \partial_t u_\delta u_\delta + \gamma\varepsilon^2 \int_\Omega |\nabla u_\delta|^2 + \int_\Omega \gamma\psi'_\delta(u_\delta)(u_\delta + 1)\right) \\
&\geq \tfrac{C}{(m+1)|\Omega|}\left(-\|\partial_t u_\delta\|_{L^2}\|u_\delta\|_{L^2} - \tfrac{1}{2}\int_\Omega (u_\delta - 1)^2 + \int_\Omega \psi_\delta(u_\delta)\right) \\
&\geq \tfrac{C}{(m+1)|\Omega|}\left(-\|\partial_t u_\delta\|_{L^2}\|u_\delta\|_{L^2} - 1 - \|u_\delta\|_{L^2}^2\right)
\end{aligned}$$

where we used (2.16), $\psi_\delta(z) \geq 0$ for all $z \in \mathbb{R}$ and $\delta \in (0,2)$ and $\psi_\delta(\pm 1) = 1$. The constant C depends on ε and γ but does not depend on δ. We treat the second case similarly and derive

$$\begin{aligned}
\lambda_\delta &= \tfrac{1}{(m-1)|\Omega|}\left(\int_\Omega \varepsilon^2 \partial_t u_\delta u_\delta + \gamma\varepsilon^2 \int_\Omega |\nabla u_\delta|^2 + \int_\Omega \gamma\psi'_\delta(u_\delta)(u_\delta - 1)\right) \\
&\leq \tfrac{C}{|m-1||\Omega|}\left(\|\partial_t u_\delta\|_{L^2}\|u_\delta\|_{L^2} + \|\nabla u_\delta\|_{L^2} - \int_\Omega \psi'_\delta(u_\delta)(u_\delta - 1)\right) \\
&\leq \tfrac{C}{|m-1||\Omega|}\left(\|\partial_t u_\delta\|_{L^2}\|u_\delta\|_{L^2} + \|\nabla u_\delta\|_{L^2} + \tfrac{1}{2}\int_\Omega (u_\delta + 1)^2 - \int_\Omega \psi_\delta(u_\delta)\right) \\
&\leq \tfrac{C}{|m-1||\Omega|}\left(\|\partial_t u_\delta\|_{L^2}\|u_\delta\|_{L^2} + 1 + \|u_\delta\|_{L^2}^2\right)
\end{aligned}$$

where we used that $m - 1 < 0$ and $\|\nabla u_\delta\|_{L^2} \leq C$. Together with $|m-1| > 1 - |m|$

and $m+1 > 1-|m|$ we can estimate λ_δ as follows

$$|\lambda_\delta| \leq \tfrac{C}{(1-|m|)|\Omega|}(\|\partial_t u_\delta\|_{L^2}\|u_\delta\|_{L^2} + \|u_\delta\|_{L^2}^2 + 1)$$

Now we square the above inequality and integrate it with respect to time. Using Young's inequality and denoting by C a generic constant that can depend on ε, γ and $|\Omega|$ we obtain

$$\begin{aligned}
\int_0^T |\lambda_\delta|^2 dt &\leq C\left(\int_0^T \|\partial_t u_\delta\|_{L^2}^2\|u_\delta\|_{L^2}^2 dt + \int_0^T \|u_\delta\|_{L^2}^4 dt + \int_0^T 1 dt\right) \\
&\leq C\left(\|u_\delta\|_{L^\infty(0,T;H^1(\Omega))}^2 \int_0^T \|\partial_t u_\delta\|_{L^2}^2 dt + T\|u_\delta\|_{L^\infty(0,T;H^1(\Omega))}^4 + T\right) \\
&\leq C
\end{aligned}$$

where we used that u_δ is uniformly bounded in $L^\infty(0,T;H^1(\Omega)) \cap H^1(0,T;L^2(\Omega))$ for $\delta \in (0,2)$. Hence we obtain

$$\lambda_\delta \in L^2(0,T) \quad \text{uniformly for } \delta \in (0,2)\,.$$

We refer to [7] where similar arguments have been used for a Cahn-Hilliard system with logarithmic free energy.

Step 4: Existence of $u \in L^2(0,T;H^2(\Omega)) \cap H^1(\Omega_T) \cap L^\infty(0,T;H^1(\Omega))$, $\mu \in L^2(\Omega)$ and $\lambda \in L^2(0,T)$ solving (2.1)-(2.6)

Using standard compactness results [100, Chapter 4] we obtain the existence of a subsequence, still denoted by (u_δ), and a $u \in L^2(0,T;H^2(\Omega)) \cap H^1(\Omega_T) \cap L^\infty(0,T;H^1(\Omega))$, such that

$$\begin{aligned}
u_\delta &\rightharpoonup u \quad \text{in } L^2(0,T;H^2(\Omega))\,, \\
u_\delta &\rightharpoonup u \quad \text{in } H^1(\Omega_T)\,, \\
u_\delta &\to u \quad \text{in } L^2(0,T;H^1(\Omega))\,, \\
u_\delta &\overset{*}{\rightharpoonup} u \quad \text{in } L^\infty(0,T;H^1(\Omega))\,, \\
u_\delta &\to u \quad \text{a.e. in } \Omega_T\,.
\end{aligned}$$

The third convergence result follows from the previous two [85]. The energy estimate (2.14) gives furthermore

$$\int_\Omega (\psi_+(u_\delta) + \psi_-(u_\delta)) \leq c(\varepsilon,\gamma,u_0)\delta$$

for almost all $t \in [0,T]$. Since $u_\delta \to u$ a.e. in Ω_T we obtain from Fatou's Lemma

$$\begin{aligned}\int_\Omega (\max(u,1)^2 + \min(u,-1)^2) &= \int_\Omega \lim_{\delta\to 0}(\max(u_\delta,1)^2 + \min(u_\delta,-1)^2) \\ &\le \liminf_{\delta\to 0} \int_\Omega (\psi_+(u_\delta) + \psi_-(u_\delta)) \\ &\le \lim_{\delta\to 0} c(\varepsilon,\gamma,u_0)\delta = 0\,.\end{aligned}$$

We hence obtain $|u| \le 1$ a.e. in Ω_T.
Defining

$$\mu_{\delta,\pm} := \pm\tfrac{\gamma}{\delta}\psi'_\pm(u_\delta)$$

we can rewrite (2.7) as

$$\lambda_\delta = \varepsilon^2\partial_t u_\delta - \gamma\varepsilon^2\Delta u_\delta + \gamma\psi'_0(u_\delta) + \mu_{\delta,+} - \mu_{\delta,-}\,. \tag{2.17}$$

Since $\mu_{\delta,+}\cdot\mu_{\delta,-} = 0$ we obtain from (2.17) and the a priori estimates on u_δ and λ_δ that

$$\|\mu_{\delta,+}\|_{L^2(\Omega_T)} + \|\mu_{\delta,-}\|_{L^2(\Omega_T)} \le c(\varepsilon,\gamma,u_0)\,.$$

Hence there exists $\mu_+, \mu_- \in L^2(\Omega_T)$ such that for a subsequence

$$\mu_{\delta,\pm} \rightharpoonup \mu_\pm \quad \text{in } L^2(\Omega_T) \quad \text{as } \delta \searrow 0\,.$$

Since $\mu_\pm$ are the weak limits of nonnegative functions we obtain $\mu_\pm \ge 0$ a.e. Passing to the limit in a weak formulation of (2.17) now gives (2.1) and (2.2). (2.3) follows since $u_\delta \to u$ in $L^2(\Omega_T)$. In addition, using the monotonicity of ψ'_+ and $\psi'_+(1) = 0$ we obtain

$$\begin{aligned}\mu_{\delta,+}(u_\delta - 1) &= \tfrac{\gamma}{\delta}\psi'_+(u_\delta)(u_\delta - 1) \\ &= \tfrac{\gamma}{\delta}(\psi'_+(u_\delta) - \psi'_+(1))(u_\delta - 1) \ge 0\,.\end{aligned}$$

Since $u_\delta \to u$ and $\mu_{\delta,+} \rightharpoonup \mu$ in $L^2(\Omega_T)$ we obtain

$$\int_{\Omega_T} \mu_+(u-1) = \lim_{\delta\to 0} \int_{\Omega_T} \mu_{\delta,+}(u_\delta - 1) \ge 0\,.$$

Since $(u-1) \le 0$ and $\mu_+ \ge 0$ we hence deduce

$$\mu_+(u-1) = 0 \text{ a.e. in } \Omega_T\,.$$

Step 5: Uniqueness of u, μ_+, μ_-, and λ
Assume that there are two solutions $(u^1, \mu_+^1, \mu_-^1, \lambda^1)$ and $(u^2, \mu_+^2, \mu_-^2, \lambda^2)$. Then we define $\overline{u} = u^1 - u^2$, $\overline{\mu}_\pm = \mu_\pm^1 - \mu_\pm^2$, $\overline{\lambda} = \lambda^1 - \lambda^2$. Multiplying the difference of the

equation (2.1) for u^1 and u^2 with $\overline{u}$ gives after integration and using $\int_\Omega \overline{u} = 0$

$$\varepsilon^2 \tfrac{d}{dt}\int_\Omega (\overline{u})^2 + \gamma\varepsilon^2 \int_\Omega |\nabla \overline{u}|^2 + \int_\Omega (\mu_+^1 - \mu_+^2)(u^1 - u^2) \\ -\int_\Omega (\mu_-^1 - \mu_-^2)(u^1 - u^2) = \gamma \int_\Omega (\overline{u})^2 \,.$$

Using that $(\mu_+^1 - \mu_+^2)(u^1 - u^2) = \mu_+^1(u^1 - 1) - \mu_+^1(u^2 - 1) + \mu_+^2(u^2 - 1) - \mu_+^2(u^1 - 1)$ and $-(\mu_-^1 - \mu_-^2)(u^1 - u^2) = -\mu_-^1(u^1 + 1) + \mu_-^1(u^2 + 1) - \mu_-^2(u^2 + 1) + \mu_-^2(u^1 + 1)$ it follows from the complementary conditions (2.4)-(2.6) that these two terms are non-negative. We hence deduce

$$\varepsilon^2 \tfrac{d}{dt}\int_\Omega |\overline{u}|^2 + \gamma\varepsilon^2 \int_\Omega |\nabla \overline{u}|^2 \leq \gamma \int_\Omega |\overline{u}|^2 \,.$$

A Grönwall argument now gives uniqueness of u. Hence $\mu_+ - \mu_- - \lambda$ is uniquely given through equation (2.1). Using that $u \in L^2(0,T;H^2(\Omega))$ and hence u is continuous for $d \leq 3$, we find for all $t \in [0,T]$ a $\rho > 0$ such that

$$A_\rho := |\{x \in \Omega |\, |u(x,t)| < 1 - \rho\}| > 0 \,.$$

Hence we obtain that for almost all $t \in [0,T]$ the Lagrange multiplier $\lambda(t)$ is uniquely given through

$$\lambda(t) = \tfrac{1}{A_\rho}\int_\Omega (\varepsilon^2 \partial_t u - \gamma\varepsilon^2 \Delta u + \gamma \psi_0'(u)) dx \,.$$

Finally, we obtain that μ_+ and μ_- are uniquely given as

$$\begin{aligned} \mu_+ &= (\lambda - \varepsilon^2 \partial_t u + \gamma\varepsilon^2 \Delta u - \gamma\psi_0'(u))_+ \,, \\ \mu_- &= (-\lambda + \varepsilon^2 \partial_t u - \gamma\varepsilon^2 \Delta u + \gamma\psi_0'(u))_+ \end{aligned}$$

where $(z)_+ := \max(z, 0)$. Here we use the fact that

$$\lambda = \varepsilon^2 \partial_t u - \gamma\varepsilon^2 \Delta u + \gamma\psi_0'(u) \quad \text{a.e. on } \{|u| < 1\} \,.$$

□

Remark 2.2.2. *i) The variational inequality (1.5) has a unique solution. This follows from a testing procedure similar to the one in Theorem 2.2.1.*
ii) If $(\mathcal{A}_m)$ holds we obtain that there exists a solution of (P_m) if and only if (2.1)-(2.6) is solvable. In particular, if there is a solution u of (P_m) Lagrange multipliers μ_+, μ_-, λ exist such that (2.1)-(2.6) hold. This follows from the unique solvability of (P_m), Theorem 2.2.1 and Lemma 2.1.1.

Similar to Lemma 2.1.1 and Theorem 2.2.1 we can prove the following theorem for

(1.4) without local constraints, i.e. the standard Allen-Cahn equation.

Theorem 2.2.3. *Let $\Omega \subset \mathbb{R}^d$ be a bounded domain which is convex or has a $C^{1,1}$–boundary and let $u_0 \in H^1(\Omega)$ such that $|u_0| \leq 1$ a.e. in Ω. Then there exists a unique solution to the Allen-Cahn variational inequality (1.4) without mass conservation and there exist unique Lagrange multipliers $\mu_+, \mu_- \in L^2(\Omega_T)$ such that the initial and boundary conditions (2.2), the complementary conditions (2.4)-(2.6) and*

$$0 = \varepsilon^2 \partial_t u - \gamma\varepsilon^2 \Delta u + \gamma\psi_0'(u) + \mu_- - \mu_- \quad \text{a.e. in } \Omega_T$$

hold.

2.3 Primal-dual active set (PDAS) method

For the numerical approximation of solutions u of (1.5) we introduce a primal-dual active set method or equivalently a semi-smooth Newton method [72]. Both are well known in the context of optimisation with partial differential equations as constraints [76, 99, 113]. A good introduction to optimisation can be found in [93, 113].
We present a time discretisation of the Allen-Cahn system (2.18) and reformulate the complementarity conditions in the form of primal-dual active sets. Finally, even though the method is not applicable to the time-discrete problem, we introduce for ease of understanding the idea of the resulting iterative solution for the time-discrete problem, which will be applied to the fully discrete problem in the next section.
We denote the time-step by τ, which can be a variable time-step, $t_0 = 0$, $t_n := t_{n-1} + \tau$ and $u^n \approx u(., t_n)$. Then the time discretisation of (P_m) is obtained using an Euler scheme. In this thesis we focus on the implicit discretisation leading to the following formulation:
Given u^{n-1} find $u = u^n \in H^1(\Omega)$ such that $\fint_\Omega u dx = m$, $|u| \leq 1$ a.e. in Ω and

$$\tfrac{\varepsilon}{\tau}(u - u^{n-1}, \chi - u) + \gamma\varepsilon(\nabla u, \nabla(\chi - u)) + \tfrac{\gamma}{\varepsilon}(\psi_0'(u), \chi - u) \geq 0 \tag{2.18}$$

for all $\chi \in H^1(\Omega)$ with $|\chi| \leq 1$ and $\fint_\Omega \chi dx = m$.
For simplicity we denote by u the time-discrete solution at time t_n. This discretisation can also be seen as the first order optimality condition of the following quadratic optimisation problem

$$\begin{aligned} &\min \left\{ \tfrac{\gamma\varepsilon}{2}\|\nabla u\|_{L^2}^2 + \tfrac{\gamma}{\varepsilon}\int_\Omega \psi_0(u) + \tfrac{\varepsilon}{2\tau}\|u - u^{n-1}\|_{L^2}^2 \right\} \\ &\text{s.t.} \quad |u| \leq 1 \ \text{ and } \ \fint_\Omega u dx = m. \end{aligned} \tag{2.19}$$

As in Lemma 2.1.1 one can reformulate (2.18) by using $1/\varepsilon$ scaled Lagrange multipliers $\mu_\pm$ on Ω for the inequality constraints $|u| \leq 1$, $\mu := \mu_+ - \mu_-$ and $\lambda \in \mathbb{R}$ for $\fint_\Omega u = m$ and obtain:

$$\mu = \lambda - \tfrac{\varepsilon^2}{\tau}(u - u^{n-1}) + \varepsilon^2\gamma\Delta u - \gamma\psi_0'(u) \qquad \text{a.e. in } \Omega\,, \tag{2.20}$$

$$\frac{\partial u}{\partial \nu} = 0 \qquad \text{a.e. on } \partial\Omega\,, \tag{2.21}$$

$$\fint_\Omega u dx = m\,, \tag{2.22}$$

together with the complementarity conditions

$$|u| \leq 1 \qquad \text{a.e. in } \Omega\,, \tag{2.23}$$

$$\mu_+(u-1) = 0,\ \mu_-(u+1) = 0 \qquad \text{a.e. in } \Omega\,, \tag{2.24}$$

$$\mu_+ \geq 0,\ \mu_- \geq 0 \qquad \text{a.e. in } \Omega\,. \tag{2.25}$$

Now the idea is to reformulate the complementarity conditions using active sets based on the primal variable u and the dual variables $\mu_\pm$. Then, for any $c > 0$, (2.23)-(2.25) is equivalent to:

$$u = 1 \ \text{ a.e. in } \mathcal{A}^+; \quad u = -1 \ \text{ a.e. in } \mathcal{A}^-; \tag{2.26}$$

$$\mu = 0 \ \text{ a.e. in } \mathcal{I} := \Omega \setminus (\mathcal{A}^+ \cup \mathcal{A}^-) \tag{2.27}$$

$$\text{with} \quad \begin{aligned} \mathcal{A}^+ &= \{x \in \Omega \mid c\,(u(x)-1) + \mu(x) > 0\} \\ \mathcal{A}^- &= \{x \in \Omega \mid c\,(u(x)+1) + \mu(x) < 0\} \end{aligned}\,. \tag{2.28}$$

The sets $\mathcal{A}^-$ and $\mathcal{A}^+$ are called active sets, meaning that the inequality constraint $|u(x)| < 1$ is active, and the set $\mathcal{I}$ is called inactive. For the Allen-Cahn equation the inactive set $\mathcal{I}$ represents the interface.
A further equivalent formulation of (2.23)-(2.25) is given by the following equation

$$\mathcal{H}(u,\mu) := \mu - \max(0, \mu + c\,(u-1)) + \min(0, \mu + c\,(u+1)) = 0. \tag{2.29}$$

The equivalence of the complementarity conditions (2.23)-(2.25), the active and inactive set formulation (2.26)-(2.28) and the equation (2.29) is obtained by noting the following:
From (2.29) we obtain that if $u + \frac{\mu}{c} \in [-1,1]$ then $\mu = 0$ and hence $u \in [-1,1]$. If $u + \frac{\mu}{c} > 1$ we obtain $\mu = c(\frac{\mu}{c} + u - 1) = \mu + c(u-1)$ which implies $u = 1$ and $\mu > 0$. If $u + \frac{\mu}{c} < -1$ we obtain $\mu = c(\frac{\mu}{c} + u + 1) = \mu + c(u+1)$ which implies $u = -1$ and $\mu < 0$.
On the other hand we obtain (2.29) by noting that $\mu = \max(\mu, 0) + \min(\mu, 0)$ and

using the complementarity conditions (2.23)-(2.25).
If the sets $\mathcal{A}^{\pm}$ were known, we would only have to solve a system of equations, namely (2.20)-(2.22) together with (2.26), (2.27). In particular, given (2.26), (2.27) the system (2.20)-(2.22) on Ω reduces to an equation for $\lambda \in \mathbb{R}$ and for u on the interface $\mathcal{I}$:

$$0 = \lambda - \tfrac{\varepsilon^2}{\tau}(u - u^{n-1}) + \varepsilon^2\gamma\Delta u - \gamma\psi_0'(u) \qquad \text{a.e. in } \mathcal{I}\,, \quad (2.30)$$

$$\frac{\partial u}{\partial \nu} = 0 \quad \text{a.e. on } \partial\mathcal{I} \cap \partial\Omega\,, \qquad u = \pm 1 \quad \text{a.e. on } \partial\mathcal{I} \cap \partial\mathcal{A}^{\pm}\,, \quad \fint_{\Omega} u = m\,. \quad (2.31)$$

Now given u and λ one can determine μ on $\mathcal{A}^{\pm}$ using (2.20).
This leads to the idea of the **Primal-Dual Active Set (PDAS) algorithm**:
Given initial active sets $\mathcal{A}_0^{\pm}$ iterate the following steps for $k \geq 0$

1. *Set $u^k = \pm 1$ on $\mathcal{A}_k^{\pm}$ and $\mu^k = 0$ on $\mathcal{I}_k$,*
2. *Solve (2.30)-(2.31) for $\lambda^k \in \mathbb{R}$ and u^k on $\mathcal{I}_k$,*
3. *Determine μ^k on $\mathcal{A}_k^{\pm}$ using (2.20),*
4. *Determine the new active sets $\mathcal{A}_{k+1}^{\pm}$,*
5. *Stop the iteration if $\mathcal{A}_{k+1}^{\pm} = \mathcal{A}_k^{\pm}$, otherwise set $k = k + 1$ and goto 1.*

This algorithm is formally equivalent to a Newton algorithm applied to (2.1)-(2.3) and (2.29), see [72]. However, the method is more driven by the current active set than by the current values of u, μ and λ in the sense that different u^k and μ^k can lead to the same active sets $\mathcal{A}^{\pm}$ and hence in the next iteration u^{k+1}, μ^{k+1} and λ^{k+1} are the same.
In general, active set methods converge faster when good initial active sets are provided. For the Allen-Cahn equation this is the case due to the evolution in time. This is why we chose an active set method over other numerical methods in optimisation such as interior point methods or sequential quadratic programming (SQP) methods [93].
As mentioned in the beginning of this section we cannot apply the primal-dual active set method to the time-discrete Allen-Cahn variational inequality (2.18). The reason is that although one can show the existence of the Langrange multipliers and the regularity $\mu_{\pm} \in L^2(\Omega)$ this regularity does in general not hold in each iteration of the PDAS- algorithm. Then the multipliers may still exist but only as measures. This effect is also known for obstacle problems [76]. Therefore, the pointwise definition of the active sets $\mathcal{A}^{\pm}$ according to (2.28) is not possible. However, we show in the next section that the application of the PDAS-method to the fully discrete problem is possible and the algorithm converges locally.

2.4 Finite element discretisation

For space discretisation we employ a finite element approximation which we present in this section. Furthermore we present the PDAS-algorithm for the fully discrete system and discuss the local convergence by employing the formulation as a semi-smooth Newton method. At the end of this section we discuss some properties of the proposed method.

2.4.1 Notation

For simplicity we assume that Ω is a polyhedral domain. We introduce now a finite element space. For more details on finite elements we refer the reader to [26].Let $\mathcal{T}_h$ be a regular triangulation of Ω into disjoint open simplices, i.e. $\Omega = \cup_{T\in\mathcal{T}_h}\overline{T}$. Furthermore, we define $h := \max_{T\in\mathcal{T}_h} \operatorname{diam} T$ the maximal element size of $\mathcal{T}_h$ and we set $\mathcal{J}$ to be the set of vertices of $\mathcal{T}_h$ and $\{p_j\}_{j\in\mathcal{J}}$ to be the coordinates of these vertices. Associated with $\mathcal{T}_h$ is the piecewise linear finite element space

$$S_h := \left\{\varphi \in H^1(\Omega) \middle| \varphi\big|_T \in P_1(T) \ \forall\ T \in \mathcal{T}_h\right\} \subset C^0(\overline{\Omega}),$$

where we denote by $P_1(T)$ the set of all affine linear functions on T. We are using P_1–finite elements because we want to make use of mass lumping, and in fact we need mass lumping in order to show convergence of the primal-dual active set method. We will refer to nodes and vertices as being the same since we restrict ourselves to P_1–elements. We denote the standard nodal basis functions of S_h by χ_j for all $j \in \mathcal{J}$. Then u_j for $j \in \mathcal{J}$ denote the coefficients of the basis representation of u_h in S_h which is given by $u_h = \sum_{j\in\mathcal{J}} u_j\chi_j$ and the vector of coefficients is denoted by $\underline{u}$. We use this notation for all vectors in $\mathbb{R}^J$, where J is the number of vertices in $\mathcal{J}$, in order to avoid confusions later on when we introduce the vector-valued Allen-Cahn equation.
In order to derive a discretisation of our models we set

$$\mathcal{K}_h := \{\eta \in S_h \,|\, |\eta(x)| \le 1 \text{ for all } x \in \Omega\}, \qquad \mathcal{K}_h^m := \{\eta \in \mathcal{K}_h | \fint_\Omega \eta dx = m\}.$$

We introduce also the lumped mass scalar product $(f,g)_h = \int_\Omega I_h(fg)$ instead of (f,g), where $I_h : C^0(\overline{\Omega}) \to S_h$ is the standard interpolation operator [26] such that $(I_h f)(p_j) = f(p_j)$ for all nodes $j \in \mathcal{J}$.
Defining $m_j := (1, \chi_j)$ we have $\fint_\Omega u_h = \sum_{j\in\mathcal{J}} m_j u_j / \sum_{j\in\mathcal{J}} m_j$. Moreover we define the stiffness matrix as $A := (a_{ij})$ with $a_{ij} = (\nabla\chi_j, \nabla\chi_i)$, the mass matrix $M := ((\chi_j,\chi_i)_h) = \operatorname{diag}(m_j)$ and the mass vector $\underline{m} := (m_j)$.

2.4.2 Finite element approximation and the PDAS-algorithm

We now introduce the following finite element approximations of (2.18) using $\psi_0'(u) = -u$. In the following we consider a fixed time-step $\tau = t_n - t_{n-1}$ and omit in some places the superscript n:
Given $u_h^{n-1} \in \mathcal{K}_h^m$ find $u_h = u_h^n \in \mathcal{K}_h^m$ such that

$$(\tfrac{\varepsilon}{\tau}(u_h - u_h^{n-1}) - \tfrac{\gamma}{\varepsilon}u_h, \chi - u_h)_h + \gamma\varepsilon(\nabla u_h, \nabla(\chi - u_h)) \geq 0 \ \ \forall \chi \in \mathcal{K}_h^m. \tag{2.32}$$

Due to the use of piecewise linear finite elements and nodal basis functions the reformulation (2.32) with Lagrange multipliers $\mu_h \in S_h$ and $\lambda \in \mathbb{R}$ can be stated as follows:
Find $u_h \in S_h$, $\mu_h \in S_h$ and $\lambda \in \mathbb{R}$ such that

$$(\tfrac{\varepsilon^2}{\tau} - \gamma)(u_h, \varphi)_h + \gamma\varepsilon^2(\nabla u_h, \nabla\varphi) + (\mu_h, \varphi)_h - \lambda(1, \varphi) = \tfrac{\varepsilon^2}{\tau}(u_h^{n-1}, \varphi)_h \ \ \forall \varphi \in S_h\,, \tag{2.33}$$

$$\sum_{j\in\mathcal{J}} m_j u_j = m \sum_{j\in\mathcal{J}} m_j\,, \tag{2.34}$$

$$(\mu_j)_- \geq 0,\ (\mu_j)_+ \geq 0,\ |u_j| \leq 1, \tag{2.35}$$

$$(u_j + 1)(\mu_j)_- = (u_j - 1)(\mu_j)_+ = 0 \quad \forall\ j \in \mathcal{J}. \tag{2.36}$$

As in (2.29) the complementarity conditions can be rewritten as

$$\mathcal{H}(u_j, \mu_j) = 0 \qquad \forall j \in \mathcal{J}\,. \tag{2.37}$$

Applying now the PDAS-method to the discrete problem (2.33)-(2.36) we obtain the following algorithm:

Primal-Dual Active Set Algorithm (PDAS-I):

0. *Set $k = 0$ and initialise $\mathcal{A}_0^{\pm}$ using u_h^{n-1} and μ_h^{n-1} from the previous time-step iteration. More precisely, set*
   $\mathcal{A}_0^+ := \{j \in \mathcal{J} : u_j^{n-1} + \frac{\mu_j^{n-1}}{c} > 1\}$, $\mathcal{A}_0^- := \{j \in \mathcal{J} : u_j^{n-1} + \frac{\mu_j^{n-1}}{c} < -1\}$.

1. *Define $\mathcal{I}_k = \mathcal{J} \setminus (\mathcal{A}_k^+ \cup \mathcal{A}_k^-)$.*
   Set $u_j^k = \pm 1$ for $j \in \mathcal{A}_k^{\pm}$ and $\mu_j^k = 0$ for $j \in \mathcal{I}_k$.

2. *Solve the discrete PDE (2.33) with the non-local constraint (2.34) to obtain u_j^k*

for $j \in \mathcal{I}_k$ and $\lambda^k \in \mathbb{R}$:

$$\begin{aligned}(\tfrac{\varepsilon}{\tau} - \tfrac{\gamma}{\varepsilon})m_j u_j^k + \gamma\varepsilon \sum_{i\in\mathcal{I}_k} a_{ij}u_i^k - \tfrac{1}{\varepsilon}m_j\lambda^k \qquad (2.38)\\ = \tfrac{\varepsilon}{\tau}m_j u_j^{n-1} + \gamma\varepsilon(\sum_{i\in\mathcal{A}_k^-} a_{ij} - \sum_{i\in\mathcal{A}_k^+} a_{ij}) \qquad \forall j \in \mathcal{I}_k\end{aligned}$$

$$\sum_{i\in\mathcal{I}_k} m_i u_i^k = m\sum_{i\in\mathcal{J}} m_i - \sum_{i\in\mathcal{A}_k^+} m_i + \sum_{i\in\mathcal{A}_k^-} m_i. \qquad (2.39)$$

3. *Determine μ_j^k for $j \in \mathcal{A}_k^\pm$ using (2.33):*

$$\mu_j^k = -(\tfrac{\varepsilon^2}{\tau} - \gamma)u_j^k - \gamma\varepsilon^2\tfrac{1}{m_j}\sum_{i\in\mathcal{J}} a_{ij}u_i^k + \lambda^k + \tfrac{\varepsilon^2}{\tau}u_j^{n-1}.$$

4. *Set $\mathcal{A}_{k+1}^+ := \{j \in \mathcal{J} : u_j^k + \frac{\mu_j^k}{c} > 1\}$, $\mathcal{A}_{k+1}^- := \{j \in \mathcal{J} : u_j^k + \frac{\mu_j^k}{c} < -1\}$.*

5. *If $\mathcal{A}_{k+1}^\pm = \mathcal{A}_k^\pm$ stop, otherwise set $k = k+1$ and goto 1.*

Remark 2.4.1. *We solve (2.38), (2.39) by multiplying (2.39) with $-\frac{1}{\varepsilon}$ and using the conjugate gradient method. In Chapter 4 we discuss the choice of linear algebra solvers in more detail.*

2.5 Convergence as a semi-smooth Newton method

In this section we consider the system (2.33), (2.34) and (2.37) as a problem of finding a root of $\boldsymbol{F}(\underline{u}, \underline{\mu}, \lambda) = \mathbf{0}$. Since the function $\mathcal{H}$ in (2.37) is not Fréchet differentiable we cannot use the classical Newton method. We need to introduce the concept of slant differentiability [40] in which case a semi-smooth Newton method can be used.

Definition 2.5.1. *Let X, Z be Banach spaces and let $F : D \subset X \longrightarrow Z$ be a mapping where D is an open subset of X. The mapping F is called **slantly differentiable** in the open subset $U \subset D$ if there exists a family of mappings $K : U \longrightarrow L(X, Z)$ such that*

$$\lim_{h\to 0}\frac{1}{\|h\|}\|F(x+h) - F(x) - K(x+h)h\| = 0$$

for every $x \in U$.

We refer to K as slanting function for F in U.
In [72] it is shown that the mapping $y \longmapsto \max(0, y)$ from $\mathbb{R}$ to $\mathbb{R}$ is slantly differentiable and one possible slanting function is $G(y) = 1$ for $y > 0$ and $G(y) = 0$ for

$y \leq 0$. Setting $\mathcal{A}_h^+ := \{j \in \mathcal{J} : u_j + \frac{\mu_j}{c} > 1\}$, $\mathcal{A}_h^- := \{j \in \mathcal{J} : u_j + \frac{\mu_j}{c} < -1\}$, $\mathcal{I}_h := \mathcal{J} \setminus (\mathcal{A}_h^+ \cup \mathcal{A}_h^-)$ and adapting the above for the min-max-function $\mathcal{H}(u_j, \mu_j)$ one derives the slanting function $\mathcal{G}(u_j, \mu_j) = (-c, 0)$ for $j \in \mathcal{A}_h^\pm$ and $\mathcal{G}(u_j, \mu_j) = (0, 1)$ for $j \in \mathcal{I}_h$. We now consider the system (2.33), (2.34) and (2.37) as a problem of finding a root of $\boldsymbol{F}(\underline{u}, \underline{\mu}, \lambda) = \mathbf{0}$, by using a semi-smooth Newton method (SSN) $(\underline{u}^{k+1}, \underline{\mu}^{k+1}, \lambda^{k+1}) = (\underline{u}^k, \underline{\mu}^k, \lambda^k) - \boldsymbol{G}(\underline{u}^k, \underline{\mu}^k, \lambda^k)^{-1} \boldsymbol{F}(\underline{u}^k, \underline{\mu}^k, \lambda^k)$. We set

$$\mathcal{G}_u(\underline{u}, \underline{\mu}) := (g_{ij}^u) \qquad \text{with} \qquad g_{ij}^u := \begin{cases} -c & \text{for } i = j \in \mathcal{A}_h^\pm \\ 0 & \text{elsewhere} \end{cases} \tag{2.40}$$

$$\mathcal{G}_\mu(\underline{u}, \underline{\mu}) := (g_{ij}^\mu) \qquad \text{with} \qquad g_{ij}^\mu := \begin{cases} 1 & \text{for } i = j \in \mathcal{I}_h \\ 0 & \text{elsewhere} \end{cases} \tag{2.41}$$

and derive for $\boldsymbol{F}$ the slanting function

$$\boldsymbol{G}(\underline{u}, \underline{\mu}, \lambda) = \begin{bmatrix} (\frac{\varepsilon^2}{\tau} - \gamma)M + \gamma\varepsilon^2 A & M & -\underline{m} \\ \mathcal{G}_u(\underline{u}, \underline{\mu}) & \mathcal{G}_\mu(\underline{u}, \underline{\mu}) & \underline{0} \\ -\underline{m}^t & \underline{0}^T & 0 \end{bmatrix}. \tag{2.42}$$

Moreover, it is easy to show the equivalence of the Newton algorithm to the PDAS-I method using as a starting set $\mathcal{A}_0^\pm$ the set given by an initial guess (u^{-1}, μ^{-1}).

Theorem 2.5.2. *The PDAS-I algorithm converges locally to the coefficient vector $\underline{u}^*$ of the solution u_h of the discrete Allen-Cahn variational inequality with mass constraints (2.32), if at least one node p_j of u_h exists such that $|u_h(p_j)| < 1$ and*

$$\tau(1 - \tfrac{\varepsilon^2}{c_h^p}) < \tfrac{\varepsilon^2}{\gamma}\,. \tag{2.43}$$

Proof: Let $\underline{\mu}^*$ and λ^* be the Lagrange multipliers corresponding to $\underline{u}^*$. Given at least one inactive node p_j of u_h there exists an open neighbourhood U of $(\underline{u}^*, \underline{\mu}^*, \lambda^*)$ where $j \in \mathcal{I}_h$ for all $(\underline{u}, \underline{\mu}, \lambda) \in U$. Since for a fixed discretisation there exists only a finite number of possible active sets, only finitely many different $\mathcal{G}_u(\underline{u}, \underline{\mu})$ and $\mathcal{G}_\mu(\underline{u}, \underline{\mu})$ can occur, as is the case for $\boldsymbol{G}$. In the following theorem we show that $\boldsymbol{G}$ is invertible for all possible active sets with $\mathcal{I}_h \neq \emptyset$. Hence the inverses of $\boldsymbol{G}$ are uniformly bounded on U. The convergence result for the semismooth Newton method in [40, 72] then provides the local convergence. □

In order to show the invertibility of $\boldsymbol{G}(\underline{u}, \underline{\mu}, \lambda)$ we need a discrete Poincaré inequality: There exists a Poincaré constant $c_h^p > 0$ such that

$$(v, v)_h \leq c_h^p (\nabla v, \nabla v) \quad \forall v \in K \tag{2.44}$$

with $K := \{v \in S_h \mid \int_\Omega v = 0, v(p_j) = 0 \text{ if } j \in \mathcal{A}_h^\pm\}$. We then obtain the following

theorem.

Theorem 2.5.3. *Assume $\mathcal{I}_h \neq \emptyset$ and let τ be such that (2.43) Then the matrix $\boldsymbol{G}(\underline{u}, \underline{\mu}, \lambda)$ is invertible which is equivalent to the unique solvability of (2.38), (2.39).*

Proof: We show that the kernel of $\boldsymbol{G}(\underline{u}, \underline{\mu}, \lambda)$ contains only $\mathbf{0}$ provided that $\mathcal{I}_h \neq \emptyset$. The equation

$$\boldsymbol{G}(\underline{u}, \underline{\mu}, \lambda)(\underline{v}, \underline{\kappa}, \alpha)^t = \mathbf{0} \tag{2.45}$$

implies $\underline{v} \equiv \underline{0}$ on the active sets $\mathcal{A}_h^{\pm}$, $\underline{\kappa} = \underline{0}$ on $\mathcal{I}_h$ and $\underline{m} \cdot \underline{v} = 0$. If one can show that $\underline{v} = \underline{0}$ has to hold, we can conclude by using a row $j \in \mathcal{I}_h$ that $\alpha = 0$. Then the first block of rows yield $\underline{\kappa} = \underline{0}$, and hence the assertion holds.
To show $\underline{v} = \underline{0}$ we prove that $v = \sum_{j \in \mathcal{J}} v_j \chi_j = 0$ is the unique solution of the quadratic optimisation problem in v on the inactive set

$$\min_{v \in K} \left[\tfrac{1}{2} (\tfrac{\varepsilon^2}{\tau} - \gamma)(v, v)_h + \tfrac{\gamma \varepsilon^2}{2} (\nabla v, \nabla v) \right] \tag{2.46}$$

where the first order necessary conditions are given by (2.45).
We show that (2.46) is a strictly convex minimisation problem. If $\tau \leq \frac{\varepsilon^2}{\gamma}$ this follows immediately. This is the time-step restriction that is usually taken for an implicit time discretisation. However, we now show how this restriction can be relaxed. To this end we need to control $(v, v)_h$ on K. Using the Poincaré inequality (2.44) we obtain

$$\tfrac{\gamma \varepsilon^2}{2} (\nabla v, \nabla v) + \tfrac{1}{2} (\tfrac{\varepsilon^2}{\tau} - \gamma)(v, v)_h \geq (\tfrac{\gamma \varepsilon^2}{2} + \tfrac{1}{2} c_h^p (\tfrac{\varepsilon^2}{\tau} - \gamma))(\nabla v, \nabla v)\,.$$

We hence obtain that (2.46) is uniquely solvable if (2.43) holds. □

In the Allen-Cahn model with double obstacle potential, interfaces have a thickness of $\pi\varepsilon$. Hence we expect that the typical Poincaré constant c_h^p in (2.44), which depends due to K only on $\mathcal{I}_h$, scales like ε^2. Then the time-step restriction is much less severe than $\tau < \frac{\varepsilon^2}{\gamma}$ which is usually taken, see [43], in fully implicit time discretisations of the Allen-Cahn equation. This shall be illustrated in the following remark.

Remark 2.5.4. *i) The Poincaré constant c_h^p and therefore the maximal possible time-step τ, see (2.43), can be estimated by a Poincaré constant $c_p(\mathcal{I}_h)$ for a continuous problem. We introduce $\Omega_{\mathcal{I}_h} := int\{x \in \Omega \mid x \in supp\, \chi_j,\ j \in \mathcal{I}_h\}$,where intA is the interior of a set A. Let $c_p(\mathcal{I}_h)$ be a Poincaré constant such that*

$$(v, v) \leq c_p(\mathcal{I}_h)\, (\nabla v, \nabla v) \quad \forall v \in H_0^1(\Omega_{\mathcal{I}_h}) \ \ with \fint_{\Omega} v dx = 0\,.$$

Since $(v,v)_h \leq (d+2)(v,v)$ *for all* $v \in S_h$ *where* d *is the space dimension, see [79] Lemma 11, we obtain* $(v,v)_h \leq c_p(\mathcal{I}_h)\,(d+2)(\nabla v, \nabla v)$ *for* $v \in K$ *and hence*

$$c_h^p \leq c_p(\mathcal{I}_h)\,(d+2)\,.$$

ii) In one dimension it is shown in [56] Lemma 6.2 that for an interface $\mathcal{I}$ *of width* $\pi\varepsilon$ *a Poincaré constant* $c_p(\mathcal{I}) = \frac{1}{4}\varepsilon^2$ *is obtained.*
Then, given a good numerical approximation $\mathcal{I}_h$ *of* $\mathcal{I}$ *no restriction at all has to be enforced for the time-step* τ *in order to show unique solvability.*

Remark 2.5.5. *We can also solve a semi-implicit discretisation, i.e. in case that we replace* $\psi_0(u_h)$ *by* $\psi_0(u_h^{n-1}) + \psi_0'(u_h^{n-1})(u_h - u_h^{n-1})$, *respectively* $\psi_0'(u_h)$ *by* $\psi_0'(u_h^{n-1})$ *and in (2.33)* $\gamma(u_h, \varphi)_h$ *by* $\gamma(u_h^{n-1}, \varphi)_h$, *with a primal-dual active set algorithm. In this case the resulting linear systems are always solvable, since in (2.46) the negative term disappears. However it will turn out that the fully implicit time discretisation is much more accurate, see Section 2.6.1.*

Further features of the PDAS-approach

Although local convergence is shown, we can face slow convergence or oscillatory behaviour of the method if the starting sets or the choice of c is not appropriate.

i) *Slow convergence*

One has to keep in mind that the convergence radius is unknown. In the worst case the radius is so small that the active set of the initial guess is identical to the active set of the solution. Then, however, the solution is obtained in one step, and hence Theorem 2.5.2 proves local exactness, which follows directly with Theorem 2.5.3. In practice we always observed convergence for a larger convergence radius. However, there exist examples for elliptic non-local obstacle problems where the active set only moves one mesh point per primal-dual active set iteration leading to a very slow convergence [21]. To overcome this one can use regularisation techniques as for example discussed in [76], or a nested approach can be used, i.e. the problem is first solved on a coarse mesh and then this solution is used as initial data for the next finer mesh. This process is repeated until the finest mesh is reached.
For Allen-Cahn variational inequalities we study discrete time evolutions and hence we always have good starting values from the previous time-step leading to fast convergence.

ii) *Oscillations in the bilateral case.*

For bilateral constraints there are situations in which iterates can oscillate between the two constraints. In [21] an example for oscillatory behaviour is discussed for an elliptic obstacle problem. This can be overcome by choosing c large enough. With a scaling of the Lagrange multiplier μ by $\frac{1}{\varepsilon}$ the parameter c should be chosen to be

larger than 1. For values $c < 1$ oscillations can occur for Allen-Cahn problems and also for Cahn-Hilliard variational inequalities, see [19]. This indicates that the local convergence radius of the PDAS-method depends on the choice of c.

iii) *Mesh-independence.*
In general, as noticed for example in [16], one will face mesh dependent convergence behaviour. To overcome this problem regularisation or penalisation techniques can be applied to analytically obtain mesh independent convergence (e.g. [76, 87, 92]). Alternatively for time independent problems, in practice one can use a nested iteration approach. This approach, which can be interpreted as regularisation due to discretisation, provides an efficient method that does not suffer (to a great extent) from mesh dependence, see [21]. For time-dependent problems, like the Allen-Cahn problems, even nested iteration is in practice not necessary, since good initial data are provided by the solution of the previous time-step. Numerical evidence of this can be seen in Section 2.6.1.

iv) *Globalisation approaches.*
In [65] a new globalisation approach of the primal-dual active set strategy for optimal control problems is discussed. The primal-dual active set method is shown to be equivalent to a non-smooth Newton method which is based on the formulation of the optimal control problem as an unconstrained minimisation problem. The gradient of the objective functional is the nonlinear Schur complement of the optimality system and it can be used as descent direction. Using a damping strategy, such as the Armijo rule, Gräser showed that the method converges for arbitrary initial data. The same strategy is used by Gräser and Kornhuber in [67] for more general set-valued saddle point problems. One of the applications discussed there is the Cahn-Hilliard equation.

2.6 Numerical tests and discussion

In this section we discuss some computational results.
In Subsection 2.6.1 we consider examples where the exact solution is known. First, we consider the Allen-Cahn variational inequality without integral constraint. We compare our PDAS-method to the widely used projected SOR method and show its efficiency. Furthermore, we see that the PDAS-method allows larger time-steps resulting in a speed up without loss of accuracy. We show numerically that the primal-dual active set method is mesh independent. Second, we present some results for the non-local Allen-Cahn equation. The computation times obtained are similar to the local Allen-Cahn variational inequalities and again large time-steps are possible. Furthermore, we consider one example where the explicit solution

is known and show that implicit discretisation provides higher accuracy than the semi-implicit one. Finally, in Subsection 2.6.2 we present two simulations for the non-local Allen-Cahn equation.

Unless it is otherwise stated, we take $\varepsilon = \frac{1}{16\pi}$ and $\gamma = 1$. Furthermore, we present numerical results in two and three space dimensions, where we take $\Omega = (-1,1)^2$ and, respectively, $\Omega = (-1,1)^3$.

We note that since the interfacial thickness is proportional to ε in order to resolve the interfacial layer we need to choose $h \ll \varepsilon$ (see [45, 50] for details). Away from the interface h can be chosen larger and hence adaptivity in space can heavily speed up computations. In fact we use the finite element toolbox ALBERTA 2.0 (see Schmidt and Siebert [108]) for adaptivity and we implemented the same mesh refinement strategy as in Barrett, Nürnberg and Styles [9]. We use u_h^{n-1} as an indicator and mark an element for refinement if $|u_h^{n-1}| < 1$ on one of the vertices of the element. An element is marked for coarsening if $u_h^{n-1} = \pm 1$ is fulfilled for all vertices of the element. For refinement and coarsening we specify a maximal element size h_{max} and a minimal element size h_{min}. For the computations in this section we take the minimal diameter of all elements $h_{min} = \frac{1}{256}$ and the maximal diameter $h_{max} = h = \frac{1}{16}$, unless otherwise stated.

For the standard Allen-Cahn variational inequality, i.e. without mass constraint, there is no Lagrange multiplier λ and (2.39) does not need to be considered. In each PDAS iteration one has to solve the linear system (2.38) without the variable λ present. For both the local and the non-local Allen-Cahn variational inequality we use the conjugate gradient method to solve the linear system (2.38)-(2.39), see also Remark 2.4.1.

2.6.1 Comparison with analytically known solutions

In order to show the accuracy and efficiency of our method we need problems where the exact solution is known. First, we consider the Allen-Cahn equation without volume constraint and we compare the primal-dual active set strategy to the widely used projected SOR method. We look at the number of primal-dual active set iterations needed for various time-step and mesh sizes and establish that the method is numerically mesh independent. Then we discuss the efficiency and accuracy of the method for the non-local Allen-Cahn variational inequality.

Comparison PDAS versus projected SOR

We begin by considering the Allen-Cahn equation without volume constraint. For this problem a projected SOR (pSOR) algorithm is often used, see [43]. We compare the PDAS method to the pSOR for the simple problems of a shrinking circle in $\mathbb{R}^2$

and a shrinking sphere in $\mathbb{R}^3$ with radius 0.45 and centre 0 and we compare the CPU times as well as the relative error at $T = 0.01$ of the two algorithms. In the tables CPU total gives the computation time needed for the program to reach the time T, whereas CPU solver gives the computation time needed for the solver only. For the projected SOR method this is the computation time needed to solve the system of equations using a projected SOR algorithm; for the PDAS method it is the time needed to solve for u_j^k the linear system of equations (2.38) without λ (there is no mass constraint present) using the conjugate gradient method. We calculate the relative error by taking the zero level set of u_h as an approximation of the sharp interface and compare it to the solution of the sharp interface formulation for which the radius $R(t)$ at time t is given by the ODE $\frac{d}{dt}R(t) = -\frac{1}{R(t)}, R(0) = 0.45$ [25]. To be precise we measure the error between the intersection points of the positive x_1-axis with the circle and with the zero level set of u_h. There may be minor variances of u_h in the other directions, but they have been negligible in our experiments. At $T = 0.01$ we have $R(T) = 0.4272$ and the circle disappears at $t = 0.10125$. For the sphere the exact solution is given by the ODE $\frac{d}{dt}R(t) = -\frac{1}{2R(t)}, R(0) = 0.45$, since the mean curvature is defined to be the sum of the principle curvatures. Hence, the sphere shrinks twice as fast as the circle. We expect essentially the relative errors for the projected SOR and the PDAS to be of the same size, since we are solving the same equation on the interface. However, for the SOR method we use $|u_j^{k,l} - u_j^{k,l-1}| < \text{tol}$ as stopping criterion while for the cg-method we use the residual. We chose and fixed the tolerances in such a way that the relative errors are almost the same for the smallest time-step. For the larger time-step the PDAS method resulted in slightly higher accuracy. Furthermore, the given averages of the degrees of freedom (DOFs) and the PDAS-iterations are averages over time. We use ø to indicate that we mean the average.

time step	CPU total [s]		CPU solver [s]		DOFs circa	rel. error		PDAS-iter. ø
	pSOR	PDAS	pSOR	PDAS		pSOR	PDAS	
$6.25{\cdot}10^{-5}$	23.57	20.59	7.47	2.77	15500	$9.64{\cdot}10^{-3}$	$7.61{\cdot}10^{-3}$	2.1
$5.00{\cdot}10^{-4}$	13.90	7.43	10.12	3.27	16500	$1.63{\cdot}10^{-2}$	$5.23{\cdot}10^{-3}$	3.2
$1.00{\cdot}10^{-3}$	-	6.59	-	3.44	17700	-	$6.11{\cdot}10^{-3}$	4.2

Table 2.1: Projected SOR method vs. PDAS-method - CPU and error for various time-steps in 2D at $T = 0.01$.

In the two dimensional case the results are listed in Table 2.1 and Figure 2.1. For both time-steps $\tau = 6.25 \cdot 10^{-5}$ and $\tau = 5 \cdot 10^{-4}$ our PDAS-method is faster. In case of $\tau = 5 \cdot 10^{-4}$ it is even about 46% faster than the pSOR method. Furthermore, it is more stable since for the pSOR method the time-step has to be less than $6 \cdot 10^{-4}$ to converge. In Theorem 2.5.3 and the following remark we have shown that the time-step can be much larger for the PDAS-method, which is also observed in the

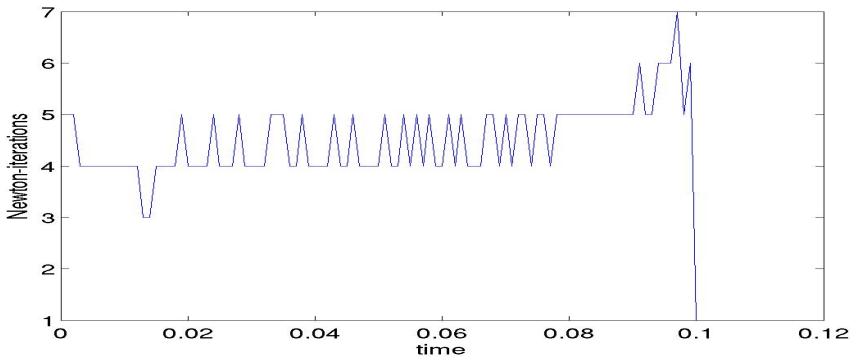

Figure 2.1: Number of Newton iterations for a shrinking circle

above calculations. In particular, in the numerical experiments the PDAS-method worked for larger time-steps as long as the mean curvature does not become too high. If the solution is only of interest at time T, large time-steps are favoured and with the PDAS-method the computation time can be reduced significantly.
In addition, larger time-steps can be taken for the PDAS-method without loosing accuracy. This is in contrast to the projected SOR method which gives a higher error for $\tau = 5 \cdot 10^{-4}$.
We note that the CPU time for the SOR solver in the projected SOR method increases for larger time-steps although there are less equations to be solved. This is due to the initial guess, which is the solution of the previous time-step, being further away from the solution of the linear system in the current time-step. The conjugate gradient solver does not depend that strongly on a good initial guess due to a higher convergence rate and converges faster than the SOR method for larger time-steps.
Moreover, the CPU time for the solver in the PDAS-method is significantly lower than for the pSOR method, since the system of equations are considerably smaller. However, the total CPU time does not decrease quite that much because extra time is needed to determine the Lagrange multiplier μ_j^k and to set the active and inactive sets.
Note that in contrast to the PDAS-method for the pSOR method the system we solve is nonlinear and hence the choice of solver is more limited. For the computations in this section we are using the conjugated gradient algorithm in the PDAS-method. In Chapter 4 we discuss different linear algebra solvers for the PDAS method.
The average number of Newton iterations increases for larger time-steps, since the interface, and hence the active set moves more in a single time-step. The dependence of the number of Newton iterations on the speed of the interface movement can also be observed in time (see Figure 2.1). When the radius becomes smaller the number of Newton iterations increases. Note that the circle disappears at $t = 0.10125$.

time step	CPU total [s]		CPU solver [s]		DOFs ø mill.	rel. error		PDAS-iter. ø
	pSOR	PDAS	pSOR	PDAS		pSOR	PDAS	
$6.25{\cdot}10^{-5}$	12447	11350	3609	1697	1.9	$8.48{\cdot}10^{-3}$	$8.95{\cdot}10^{-3}$	4.2
$5.00{\cdot}10^{-4}$	6072	2500	4713	1029	2.1	$4.22{\cdot}10^{-3}$	$2.63{\cdot}10^{-3}$	4.7
$1.00{\cdot}10^{-3}$	-	2216	-	1290	2.3	-	$3.18{\cdot}10^{-3}$	6.1

Table 2.2: Projected SOR method vs. PDAS-method - CPU and error for various time-steps in 3D at $T = 0.01$.

For the three dimensional test problem the same behaviour is observed as in the two dimensional case, see Table 2.2. We note in particular that for $\tau = 5 \cdot 10^{-4}$ our method is 2.4 times faster than the pSOR method. This is mostly due to the decreased computation time needed to solve the linear systems. Since the mean curvature is defined as the sum of all principle curvatures the curvature of the sphere is twice as high as the curvature of a circle with the same radius. This has the effect that the interface changes more rapidly and hence, the number of Newton iterations is significantly higher for the three dimensional case. Moreover, we see that in higher dimensions it is essential to be able to use large time-steps for the study of the interface at a specific time T, which is possible with the PDAS-method. In comparison to the pSOR method we obtain u_h with a speed up of 64%.
The computations in Table 2.1 and 2.2 use a fixed mesh size as defined in the beginning of this section. By fixed mesh size we mean that h_{min} and h_{max} are fixed and an adaptive mesh is used. We also investigated other mesh sizes and compared the computation times for PDAS and pSOR. In all cases the PDAS-method was quicker than pSOR and the results presented here are representative.
Finally, we would like to mention that most existing literature concentrates up to now on the explicit discretisation where with the use of mass lumping a non-linear system of equations has to be solved [25, 57, 94]. The explicit discretisation has the usual stability restriction for parabolic problems, $\tau \leq Ch^2$. Since we need $h \ll \varepsilon$ this time-step restriction is very strong. In contrast, for the implicit discretisation in time in combination with the suggested PDAS-method, which we study in this paper, we only have the restriction (2.43). In our computations we were able to increase the time-step up to $\tau = 1 \cdot 10^{-3}$.

Mesh independence

Since we are applying the PDAS algorithm to the fully discrete problem the number of PDAS iterations might depend on the element size h. Analytical results on this are still lacking. However, we can investigate this numerically.
First, we fix $\varepsilon = \frac{1}{16\pi}$ and $\tau = 5 \cdot 10^{-4}$. We use a uniform mesh in a two dimensional domain where the elements have a maximal size of h. We consider again the test problem of the shrinking circle. The third column in Table 2.3 shows the average

number of PDAS iterations for 60 time-step iterations, i.e. up to $t = 0.03$. Although the number of PDAS iterations increases for smaller mesh size, this increase is only by a factor of approximately 1.3 and not 2 or 4 as one might expect since the element size is halved. This is due to the time evolution, since good initial data on the current time-step are given from the solution of the previous time-step.

h	DOFs	PDAS iter. ø for $\tau = 5 \cdot 10^{-4}$	τ	PDAS iter. ø for varying τ
1/128	66049	2.57	$1 \cdot 10^{-3}$	3.20
1/256	263169	3.10	$5 \cdot 10^{-4}$	3.10
1/512	1050625	4.02	$2.5 \cdot 10^{-4}$	3.30
1/1024	4198401	5.18	$1.25 \cdot 10^{-4}$	3.37

Table 2.3: Average number of PDAS iterations up to $t = 0.03$ for varying mesh and time-step sizes.

However, in our applications the time-step τ and the space discretisation are in general coupled. Hence it is more appropriate to look at the number of Newton iterations when both τ and h are driven to zero. The average number of iterations up to $t = 0.03$ is listed in the last column and is almost constant. Hence, although we are not able to show mesh independence analytically, our numerical investigations clearly indicate that the proposed method is mesh independent.

Non-local Allen-Cahn variational inequality

Example 1: To clarify the difference between problems without and with integral constraints we consider the same model problem as before, i.e. a circle of radius 0.45 as initial interface, but now with volume conservation. Now the circle should keep its shape and stay stationary. Therefore we expect only minor changes in the active set due to discretisation errors. This behaviour can be seen in Table 2.4 by looking at the numbers of Newton iterations averaged over time, which are between 1 and 2. Only for the first iteration we need 3 or 4 Newton iterations after which the number of Newton iterations goes down to 2 and soon stabilises at only one Newton iteration per time-step iteration. The CPU time does not increase compared to the computations for the shrinking circle. As before we use the conjugate gradient method and essentially we only add one more row and column to the linear system of equations. Again large time-steps can be used and speed up the calculation without loss of accuracy.

Example 2: Next, we take two spheres with radii r_1 and r_2 which do not intersect, more precisely we set $r_1(0) = 0.3$ and $r_2(0) = 0.2$ with centres $(-0.5, 0)$ and $(0.5, 0)$. This results for the sharp interface problem in $r_1' = -\frac{1}{r_1} + \lambda$, $r_2' = -\frac{1}{r_2} + \lambda$ together with the condition of volume conservation $0 = \frac{1}{2}(r_1^2 + r_2^2)'$ which gives that $\lambda = \frac{2}{r_1 + r_2}$.

time-step	CPU [s] total	CPU [s] solver	DOFs circa	rel. error	Newton iter. ø
$6.25 \cdot 10^{-5}$	19.75	4.42	16000	$4.08 \cdot 10^{-4}$	1.07
$5.00 \cdot 10^{-4}$	7.06	3.46	17000	$4.04 \cdot 10^{-4}$	1.50
$1.00 \cdot 10^{-3}$	6.74	3.95	17500	$4.00 \cdot 10^{-4}$	2.00

Table 2.4: PDAS-method for the volume conserved Allen-Cahn equation at $T = 0.01$.

This ODE can be solved analytically [103]. The larger circle grows while the smaller one disappears roughly at time $T = 0.053$. Again we compared the radii of the sharp interface solution with the approximations we obtained using the PDAS-method. We employed a semi-implicit as well as an implicit discretisation in time. In Figure 2.2 the radii of the larger circle over time are displayed for all three solutions for three different time-step sizes. The behaviour for the smaller circle is essentially the same and therefore omitted. The semi-implicit approximation leads to very poor accuracy for larger time-steps, in particular at growing time t. Although accuracy improves for smaller time-steps it remains worse than the approximation obtained for implicit discretisation in time. Hence, even though there is no time-step restriction for the semi-implicit time discretisation the time-step still needs to be very small to achieve accurate approximations. The implicit discretisation leads to better results.

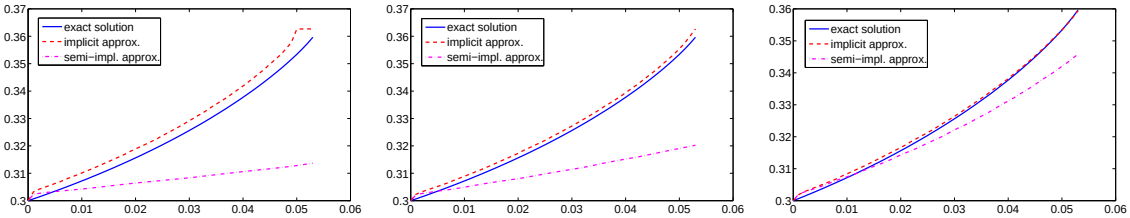

$\tau = 1.0 \cdot 10^{-3}$ $\tau = 5.0 \cdot 10^{-4}$ $\tau = 6.25 \cdot 10^{-5}$

Figure 2.2: Comparison: sharp interface solution vs. semi-implicit and implicit PDAS-approximation.

For the implicit discretisation the absolute error in time is given in Figure 2.3. The errors are of order 10^{-3} but increase significantly when the circle with initial radius $r_2(0) = 0.2$ becomes very small. Close to this singularity a smaller time-step achieves higher accuracy, whereas if the radii of the circles are big enough larger time-steps can be chosen. This clearly indicates that an adaptive choice of the time-step would be favourable. This however, is a subject for further research.

2.6.2 Numerical Simulations

For the first simulation (Figure 2.4) of interface evolution with volume constraint in two space dimensions we set the initial values for the order parameter u randomly between -0.1 and 0.1, i.e. there are no pure phases present. We used the time-step

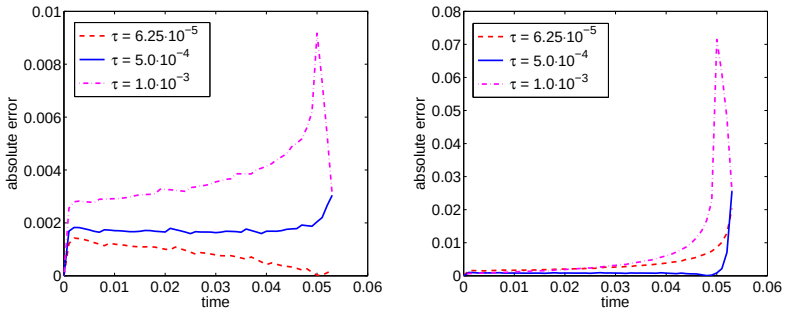

Figure 2.3: Absolute error between sharp interface solution and approximations (using implicit discretisation in time) of r_1 (left) and r_2 (right) for various time-steps.

$\tau = 6.25 \cdot 10^{-5}$. Already at time $t = 0.002$ grains start to form and grow and at $t = 0.003$ we have two phases (red and blue) separated by a diffuse interface. Now the interface moves according to motion by mean curvature but preserving the volume of both phases. That means that closed curves turn into circles and shapes with less volume shrink and disappear while at the same time shapes with the highest volume will grow. At the end (i.e. when the problem becomes stationary) there are four different shapes we can obtain: a circle, a half circle, a quarter of a circle in one of the corners (see Figure 2.4) and a straight vertical or horizontal line dividing the two phases.

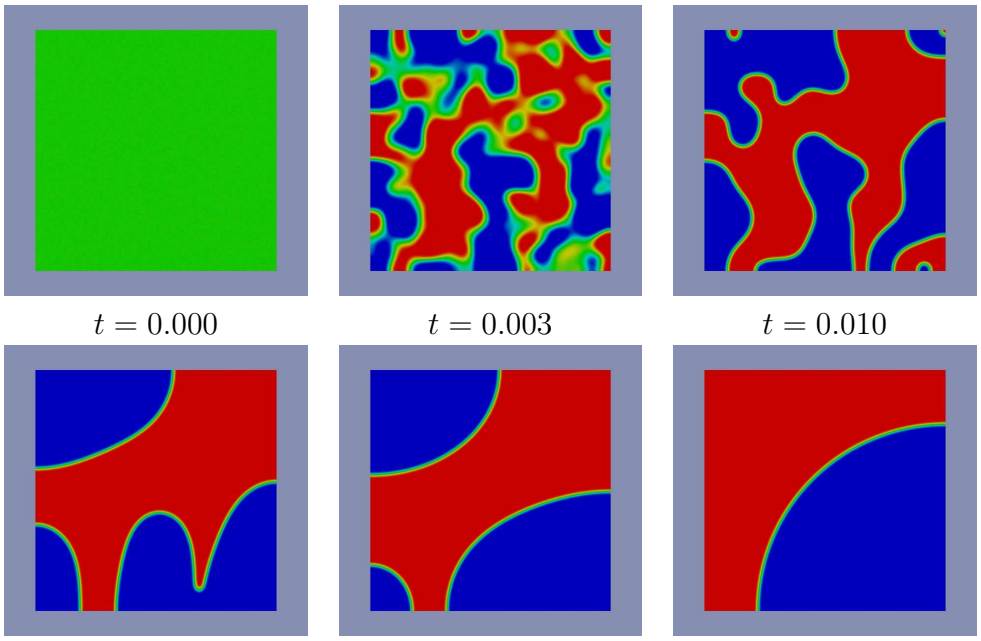

Figure 2.4: Volume controlled Allen-Cahn equation (2d) with random initial data (varying between -0.1 and 0.1).

For the computation in Figure 2.5 we use a three dimensional domain with one of the phases being a dumbbell. For this computation we had to take a coarser mesh due to memory restrictions. We used $h_{min} = \frac{1}{128}$ and $h_{max} = \frac{1}{16}$ and we set

$\tau = 6.25 \cdot 10^{-5}$. Without the volume conservation the dumbbell would dissect and the two spheres would shrink and disappear. The volume conservation forces the dumbbell to turn into an ellipsoid before turning into a sphere and finally becoming stationary.

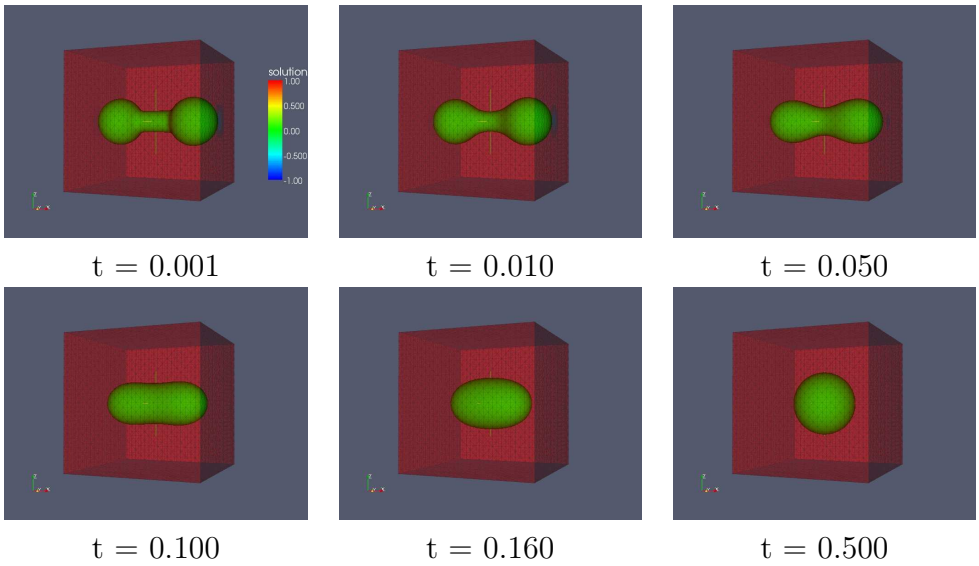

Figure 2.5: Volume controlled Allen-Cahn equation with a dumbbell as initial data.

Chapter 3

Vector-valued Allen-Cahn variational inequality with non-local constraints

The scalar Allen-Cahn equation describes the motion of an interface separating two phases. In practical applications often more than two phases occur [61, 77] and the phase field concept has been extended to deal with multiphase systems [28, 59]. The phase field takes now the form of a vector-valued function $\boldsymbol{u} : \Omega \times (0,T) \to \mathbb{R}^N$ which describes the fractions of the phases, i.e., each component u_i of $\boldsymbol{u}$ describes one phase.
The underlying non-convex energy is based on the Ginzburg-Landau energy for a vector-valued phase field $\boldsymbol{u} \in \mathbb{R}^N$

$$E(\boldsymbol{u}) := \int_\Omega \left(\tfrac{\gamma\varepsilon}{2} |\nabla \boldsymbol{u}|^2 + \tfrac{\gamma}{\varepsilon} \psi(\boldsymbol{u}) \right) dx \tag{3.1}$$

where $\Omega \subset \mathbb{R}^d$ is a bounded domain, $\gamma > 0$ is a parameter related to the interfacial energy and ψ is a bulk potential. Since each component of $\boldsymbol{u}$ stands for the fraction of one phase, the phase space for the order parameter $\boldsymbol{u}$ is the Gibbs simplex

$$\boldsymbol{G} := \{\boldsymbol{\xi} \in \mathbb{R}^N : \boldsymbol{\xi} \geq \mathbf{0}, \boldsymbol{\xi} \cdot \mathbf{1} = 1\}.$$

Here $\boldsymbol{\xi} \geq \mathbf{0}$ means $\xi_i \geq 0$ for all $i \in \{1, ..., N\}$, $\mathbf{1} = (1, ..., 1)^T$ and $\boldsymbol{\xi} \cdot \mathbf{1} = \sum_{i=1}^{N} \xi_i$. For the bulk potential $\psi : \mathbb{R}^N \to \mathbb{R}_0^+ \cup \{\infty\}$ we consider the multi-obstacle potential

$$\psi(\boldsymbol{\xi}) = \begin{cases} \psi_0(\boldsymbol{\xi}) := -\frac{1}{2} \boldsymbol{\xi} \cdot W \boldsymbol{\xi} & \text{for } \boldsymbol{\xi} \geq \mathbf{0}, \boldsymbol{\xi} \cdot \mathbf{1} = 1, \\ \infty & \text{otherwise,} \end{cases} \tag{3.2}$$

with W being a symmetric constant $N \times N$ matrix [25, 47]. Let $\sigma_{max}(W)$ be the

largest eigenvalue of W. If all eigenvalues of W were negative ψ would be a convex potential. However, different phases which correspond to minima of ψ only occur if W has at least one positive eigenvalue. We hence assume that W has at least one positive eigenvalue; the analysis in this paper would simplify if this were not the case.

Given an initial phase distribution $\boldsymbol{u}(.,0) = \boldsymbol{u}_0 : \Omega \to \boldsymbol{G}$ at time $t = 0$ the interface motion can be modelled by the steepest descent dynamics of $E(\boldsymbol{u})$ with respect to the L^2-norm which results, after suitable rescaling of time, in the following vector-valued Allen-Cahn equation

$$\varepsilon \tfrac{\partial \boldsymbol{u}}{\partial t} = -\mathrm{grad}_{L^2} E(\boldsymbol{u}) = \gamma\varepsilon\Delta\boldsymbol{u} + \tfrac{\gamma}{\varepsilon} W\boldsymbol{u} - \boldsymbol{\mu^*}$$

where $\boldsymbol{\mu^*} \in \partial I_G$ and ∂I_G denotes the subdifferential of the indicator function I_G of the Gibbs simplex. As for the scalar case this equation leads to the following variational inequality

$$\varepsilon(\tfrac{\partial \boldsymbol{u}}{\partial t}, \boldsymbol{\chi} - \boldsymbol{u}) + \gamma\varepsilon(\nabla\boldsymbol{u}, \nabla(\boldsymbol{\chi} - \boldsymbol{u})) - \tfrac{\gamma}{\varepsilon}(W\boldsymbol{u}, \boldsymbol{\chi} - \boldsymbol{u}) \geq 0 \tag{3.3}$$

which has to hold for almost all t and all $\boldsymbol{\chi} \in \mathcal{G} := \{\boldsymbol{v} \in \boldsymbol{H}^1(\Omega) : \sum_{i=1}^{N} v_i = 1,\ \boldsymbol{v} \geq \boldsymbol{0}\}$. We denote by $\boldsymbol{L}^2(\Omega)$ and $\boldsymbol{H}^1(\Omega)$ the spaces of vector-valued functions $(L^2(\Omega))^N$ and $(H^1(\Omega))^N$ respectively.

As in the scalar case one often considers systems in which the total spatial amount of the phases are conserved. In this case one studies the steepest descent of (3.1) under the constraint $\fint_\Omega \boldsymbol{u}\, dx = \boldsymbol{m}$ where $\boldsymbol{m} = (m^1, m^2, ..., m^N)^T$ with $m^i \in (0,1)$ for $i \in \{1, ..., N\}$ being a fixed number. Here we use the notation $\boldsymbol{m}$ and m^i in order to avoid confusion with the mass vector $\underline{m}$ and its components m_i introduced in Section 2.4.1.

To ensure that all phases are present we require $0 < m^i < 1$ and $\sum_{i=1}^{N} m^i = 1$, where the last condition makes sure that $\sum_{i=1}^{N} u_i = 1$ can be true. We define

$$\mathcal{G}^{\boldsymbol{m}} := \{\boldsymbol{v} \in \mathcal{G} : \fint_\Omega \boldsymbol{v} - \boldsymbol{m} = \boldsymbol{0}\}$$

and note that for $\boldsymbol{u} \in \mathcal{G}^{\boldsymbol{m}}$ it follows $\fint_\Omega \boldsymbol{u} - \boldsymbol{m} \in S := \{\boldsymbol{v} \in \mathbb{R}^N : \sum_{i=1}^{N} v_i = 0\}$.

Then the interface evolution with volume conservation can be formulated as:

($\boldsymbol{P_m}$) *For given* $\boldsymbol{u}(.,0) = \boldsymbol{u}_0 \in \mathcal{G}^{\boldsymbol{m}}$ *find* $\boldsymbol{u} \in L^2(0,T;\mathcal{G}^{\boldsymbol{m}}) \cap H^1(0,T;\boldsymbol{L}^2(\Omega))$ *such that*

$$\varepsilon(\tfrac{\partial \boldsymbol{u}}{\partial t}, \boldsymbol{\chi} - \boldsymbol{u}) + \gamma\varepsilon(\nabla\boldsymbol{u}, \nabla(\boldsymbol{\chi} - \boldsymbol{u})) - \tfrac{\gamma}{\varepsilon}(W\boldsymbol{u}, \boldsymbol{\chi} - \boldsymbol{u}) \geq 0 \tag{3.4}$$

which has to hold for almost all $t \in (0,T)$ *and all* $\boldsymbol{\chi} \in \mathcal{G}^{\boldsymbol{m}}$.

This chapter is organised in the same way as the previous chapter. First, we reformulate (3.4) with the help of Lagrange multipliers $\boldsymbol{\mu}, \boldsymbol{\lambda}$ and Λ corresponding to the constraints $\boldsymbol{u} \geq \boldsymbol{0}$, $\fint_\Omega \boldsymbol{u} - \boldsymbol{m} = \boldsymbol{0}$ and $\sum_{i=1}^N u_i = 1$ respectively. Using this formulation we show existence and uniqueness of a solution $\boldsymbol{u}$ of (3.4) and of the Lagrange multipliers. We derive a discretisation of (3.4) and apply the primal-dual active set method to it. Using the equivalence of the PDAS method and a semi-smooth Newton method we show local convergence of our algorithm. Finally, we demonstrate the efficiency and accuracy of our method using two model problems for which the explicit solution is known. We also show numerically that the proposed method is mesh independent as well as independent of the number of phases. Finally, we present some interesting numerical simulations in two and three space dimensions including soap bubble configurations and grain growth.

3.1 Formulation as a complementarity problem

Similar to the scalar case we first reformulate the problem $(\boldsymbol{P_m})$ with the help of (scaled) Lagrange multipliers $\boldsymbol{\mu}$ corresponding to the inequality constraint $\boldsymbol{u} \geq \boldsymbol{0}$, Λ corresponding to the constraint $\sum_{i=1}^N u_i = 1$ and $\boldsymbol{\lambda}$ corresponding to the constraint $\boldsymbol{P}_S(\fint_\Omega \boldsymbol{u} - \boldsymbol{m}) = \boldsymbol{0}$, where $\boldsymbol{P}_S : \mathbb{R}^N \longrightarrow S$ is a projection onto S. This could be for example an orthogonal projection but other projections can also be used. Note that due to the constraint $\sum_{i=1}^N u_i = 1$ we have that $\fint_\Omega \boldsymbol{u} - \boldsymbol{m} \in S$ already and hence $\fint_\Omega \boldsymbol{u} - \boldsymbol{m} = \boldsymbol{0}$. The reason we are introducing a projection at this point is to obtain $N-1$ constraints for the volume constraints instead of N constraints. Thus all the constraints are linearly independent and we can show uniqueness of a solution.

Lemma 3.1.1. *Let* T *be a positive time and let* $\Omega \subset \mathbb{R}^d$ *be a bounded domain which is either convex or fulfils* $\partial\Omega \in C^{1,1}$. *A function* $\boldsymbol{u} \in L^2(0,T;\boldsymbol{H}^2(\Omega)) \cap H^1(0,T;\boldsymbol{L}^2(\Omega)) \cap L^2(0,T;\mathcal{G}^{\boldsymbol{m}})$ *solves* $(\boldsymbol{P_m})$ *if there exist* $\boldsymbol{\mu} \in L^2(0,T;\boldsymbol{L}^2(\Omega))$, $\boldsymbol{\lambda} \in \boldsymbol{L}^2(0,T;S)$ *and* $\Lambda \in L^2(0,T;L^2(\Omega))$ *such that*

$$\varepsilon \tfrac{\partial \boldsymbol{u}}{\partial t} - \gamma\varepsilon\Delta\boldsymbol{u} - \tfrac{\gamma}{\varepsilon} W\boldsymbol{u} - \tfrac{1}{\varepsilon}\boldsymbol{\mu} - \tfrac{1}{\varepsilon}\Lambda\boldsymbol{1} - \tfrac{1}{\varepsilon}\boldsymbol{\lambda} = \boldsymbol{0} \qquad \text{a.e. in } \Omega_T := \Omega \times (0,T), \tag{3.5}$$

$$\boldsymbol{u}(0) = \boldsymbol{u}_0, \quad \tfrac{\partial \boldsymbol{u}}{\partial \nu} = \boldsymbol{0} \qquad \text{a.e. on } \partial\Omega \times (0,T), \tag{3.6}$$

$$\sum_{i=1}^N u_i = 1, \quad \boldsymbol{u} \geq \boldsymbol{0}, \quad \boldsymbol{\mu} \geq \boldsymbol{0} \qquad \text{a.e. in } \Omega_T, \tag{3.7}$$

$$\boldsymbol{P}_S(\fint_\Omega \boldsymbol{u} - \boldsymbol{m}) = \boldsymbol{0}, \quad (\boldsymbol{\mu}, \boldsymbol{u}) = 0 \qquad \text{for almost all } t \in (0,T). \tag{3.8}$$

Proof: Let $\boldsymbol{\chi} \in \mathcal{G}^{\boldsymbol{m}}$, then multiplying (3.5) by $(\boldsymbol{\chi} - \boldsymbol{u})$ and integrating by parts

gives

$$\int_\Omega (\varepsilon \tfrac{\partial \boldsymbol{u}}{\partial t} - \tfrac{\gamma}{\varepsilon} W\boldsymbol{u} - \tfrac{1}{\varepsilon}\boldsymbol{\mu} - \tfrac{1}{\varepsilon}\Lambda\mathbf{1} - \tfrac{1}{\varepsilon}\boldsymbol{\lambda}) \cdot (\boldsymbol{\chi} - \boldsymbol{u}) + \int_\Omega \gamma\varepsilon \nabla \boldsymbol{u} \cdot \nabla(\boldsymbol{\chi} - \boldsymbol{u}) = 0$$

for a.e. $t \in (0, T)$. Using the property $\boldsymbol{\chi} \geq \mathbf{0}$ and (3.7) - (3.8) gives

$$\int_\Omega \boldsymbol{\mu} \cdot (\boldsymbol{\chi} - \boldsymbol{u}) \geq 0.$$

Using (3.8), $\fint_\Omega \boldsymbol{\chi} = \boldsymbol{m}$ and the fact that $\boldsymbol{\lambda}$ is independent of $x \in \Omega$ we obtain

$$\int_\Omega \boldsymbol{\lambda} \cdot (\boldsymbol{\chi} - \boldsymbol{u}) = \boldsymbol{\lambda} \cdot \int_\Omega (\boldsymbol{\chi} - \boldsymbol{u}) = |\Omega| \boldsymbol{\lambda} \cdot [(\fint_\Omega \boldsymbol{\chi} - \boldsymbol{m}) - (\fint_\Omega \boldsymbol{u} - \boldsymbol{m})] = 0.$$

Since $\int_\Omega \mathbf{1} \cdot (\boldsymbol{\chi} - \boldsymbol{u}) = 0$ we obtain for all $\boldsymbol{\chi} \in \mathcal{G}^{\boldsymbol{m}}$ and almost all $t \in (0, T)$

$$\int_\Omega (\varepsilon \tfrac{\partial \boldsymbol{u}}{\partial t} - \tfrac{\gamma}{\varepsilon} W\boldsymbol{u}) \cdot (\boldsymbol{\chi} - \boldsymbol{u}) + \int_\Omega \gamma\varepsilon \nabla \boldsymbol{u} \cdot \nabla(\boldsymbol{\chi} - \boldsymbol{u}) \geq 0$$

and hence $\boldsymbol{u}$ solves $(\mathbf{P}_{\boldsymbol{m}})$.

□

3.2 Existence and uniqueness

To show the existence of $(\boldsymbol{u}, \boldsymbol{\mu}, \boldsymbol{\lambda}, \Lambda)$ we now introduce the following regularisation of ψ:

$$\psi_\delta(\boldsymbol{\xi}) = \psi_0(\boldsymbol{\xi}) + \tfrac{1}{\delta}\hat{\psi}(\boldsymbol{\xi}) \tag{3.9}$$

where

$$\hat{\psi}(\boldsymbol{\xi}) = \sum_{i=1}^{N} (\min(\xi_i, 0))^2. \tag{3.10}$$

Similar regularisations were used in [47, 7, 8]. We define the function $\hat{\phi}(r) = 2\min(r, 0)$ for all $r \in \mathbb{R}$ and note that $D\hat{\psi}(\boldsymbol{\xi}) = \hat{\boldsymbol{\phi}}(\boldsymbol{\xi}) := (\hat{\phi}(\xi_i))_{i=1}^N$. The functions $\hat{\phi}$ and ψ_δ have the following properties:

- For all $r, s \in \mathbb{R}$

$$0 \leq (\hat{\phi}(r) - \hat{\phi}(s))(r - s). \tag{3.11}$$

- For all $\boldsymbol{\xi}, \boldsymbol{\eta} \in \mathbb{R}^N$

$$\begin{aligned}(\boldsymbol{\xi}-\boldsymbol{\eta})\cdot D\psi_\delta(\boldsymbol{\eta}) &\leq \tfrac{1}{\delta}\hat{\psi}(\boldsymbol{\xi}) - \tfrac{1}{\delta}\hat{\psi}(\boldsymbol{\eta}) - (\boldsymbol{\xi}-\boldsymbol{\eta})\cdot W\boldsymbol{\eta} \\ &\leq \psi_\delta(\boldsymbol{\xi}) - \psi_\delta(\boldsymbol{\eta}) + \tfrac{1}{2}\sigma_{max}(W)\|\boldsymbol{\xi}-\boldsymbol{\eta}\|^2,\end{aligned} \tag{3.12}$$

  where we have used that $\hat{\psi}$ is convex and the identity

$$-2(\boldsymbol{\xi}-\boldsymbol{\eta})\cdot W\boldsymbol{\eta} = \boldsymbol{\eta}\cdot W\boldsymbol{\eta} - \boldsymbol{\xi}\cdot W\boldsymbol{\xi} + (\boldsymbol{\xi}-\boldsymbol{\eta})\cdot W(\boldsymbol{\xi}-\boldsymbol{\eta}).$$

- For all $\boldsymbol{\xi} \in \mathcal{M} := \{\boldsymbol{\xi} \in \mathbb{R}^N : \sum_{i=1}^N \xi_i = 1\}$ and $\delta \leq \delta_0 := \frac{1}{4N(N-1)^2\sigma_{max}(W)}$ we have that

$$\psi_\delta(\boldsymbol{\xi}) \geq \tfrac{1}{2\delta}\sum_{i=1}^N [\xi_i]_-^2 - C(N, \sigma_{max}(W)) \tag{3.13}$$

  where $[\cdot]_- := \min(\cdot, 0)$. This follows from

$$\begin{aligned}\psi_\delta(\boldsymbol{\xi}) &\geq \tfrac{1}{\delta}\sum_{i=1}^N [\xi_i]_-^2 - \sum_{i=1}^N \sigma_{max}(W)\xi_i^2 \\ &\geq \tfrac{1}{2\delta}\sum_{i=1}^N [\xi_i]_-^2 + \tfrac{1}{2\delta}[\xi_m]_-^2 - N\sigma_{max}(W)\xi_M^2\end{aligned} \tag{3.14}$$

  where $\xi_m := \min_{i=1,\dots,N} \xi_i$ and $|\xi_M| := \max_{i=1,\dots,N} |\xi_i|$.
  Since $\boldsymbol{\xi} \in \mathcal{M}$ it follows that

$$[\xi_m]_- \leq \xi_M \leq 1 - (N-1)[\xi_m]_-$$

  and hence

$$\xi_M^2 \leq 2(1 + (N-1)^2[\xi_m]_-^2)$$

  and hence (3.13) follows from (3.14) for all $\delta \leq \delta_0$.

In order to deal with the constraints $\sum_{i=1}^N u_i = 1$ and $\fint_\Omega \boldsymbol{u} - \boldsymbol{m} = \boldsymbol{0}$ we project $D\psi_\delta$ orthogonally first onto the space S and then onto $\mathcal{G}^{\boldsymbol{m}}$. This results in the following regularised version of the Allen-Cahn equation

$$\varepsilon\tfrac{\partial \boldsymbol{u}_\delta}{\partial t} - \gamma\varepsilon\Delta\boldsymbol{u}_\delta + \tfrac{\gamma}{\varepsilon}(I - \fint_\Omega)(I - \mathbf{1}\sum)D\psi_\delta(\boldsymbol{u}_\delta) = \boldsymbol{0} \tag{3.15}$$

where $(I - \fint_\Omega)\boldsymbol{\eta} := \boldsymbol{\eta} - \fint_\Omega \boldsymbol{\eta}$ for all $\boldsymbol{\eta} \in \boldsymbol{L}^2(\Omega)$ and $(I - \mathbf{1}\sum)\boldsymbol{v} := \boldsymbol{v} - \mathbf{1}\sum\boldsymbol{v}$ with

$$\sum\boldsymbol{v} := \tfrac{1}{N}\sum_{i=1}^N v_i$$

for all $\boldsymbol{v} \in \mathbb{R}^N$.
Equivalently we have to solve the following problem:

$(\boldsymbol{P}^{\boldsymbol{\delta}}_{\boldsymbol{m}})$ *Given $\boldsymbol{u}_\delta(.,0) = \boldsymbol{u}_0 \in \mathcal{G}^{\boldsymbol{m}}$ find $\boldsymbol{u}_\delta \in H^1(0,T;\boldsymbol{L}^2(\Omega)) \cap L^2(0,T;\boldsymbol{H}^1(\Omega))$ such that*

$$\varepsilon(\tfrac{\partial \boldsymbol{u}_\delta}{\partial t}, \boldsymbol{\chi}) + \gamma\varepsilon(\nabla \boldsymbol{u}_\delta, \nabla \boldsymbol{\chi}) + \tfrac{\gamma}{\varepsilon}((I - \mathbf{1}\sum)(D\psi_\delta(\boldsymbol{u}_\delta)), (I - \fint_\Omega)\boldsymbol{\chi}) = 0 \tag{3.16}$$

for all $\boldsymbol{\chi} \in \boldsymbol{H}^1(\Omega)$ and almost all $t \in (0,T)$.

Note that a solution of $(\boldsymbol{P}^{\boldsymbol{\delta}}_{\boldsymbol{m}})$ is such that for almost every $(x,t) \in \Omega_T$

$$\sum_{i=1}^{N} (u_\delta(x,t))_i = 1. \tag{3.17}$$

This follows from choosing $\boldsymbol{\chi} = (N\sum \boldsymbol{u}_\delta - 1)\mathbf{1}$ in (3.16) and using the fact that $\boldsymbol{u}_0 \in \mathcal{G}^{\boldsymbol{m}}$.
Furthermore, (3.17) gives that

$$\sum \tfrac{\partial \boldsymbol{u}_\delta}{\partial t} = 0. \tag{3.18}$$

Choosing a constant test function in (3.16) we obtain

$$\tfrac{d}{dt} \fint_\Omega \boldsymbol{u}_\delta = \mathbf{0} \tag{3.19}$$

and hence the total masses of the components of $\boldsymbol{u}_\delta$ are preserved.

Theorem 3.2.1. *Let $\Omega \subset \mathbb{R}^d$ be a bounded domain and assume that either Ω is convex or $\partial\Omega \in C^{1,1}$. Let $\boldsymbol{u}_\delta(x,0) = \boldsymbol{u}_0(x) \in \boldsymbol{H}^1(\Omega)$ with $\boldsymbol{u}_0 \geq \mathbf{0}, \fint_\Omega \boldsymbol{u}_0 = \boldsymbol{m}$ and $\sum_{i=1}^{N} (u_0)_i = 1$ a.e. in Ω and let $\beta \in (0,1)$ be such that $\beta\mathbf{1} < \fint_\Omega \boldsymbol{u}_0 < (1-\beta)\mathbf{1}$. Then there exists a unique solution $\boldsymbol{u}_\delta$ to $(\boldsymbol{P}^{\boldsymbol{\delta}}_{\boldsymbol{m}})$ for all $\delta \in (0,1]$ and a constant $C > 0$ which does not depend on δ such that*

$$\|\boldsymbol{u}_\delta\|_{L^\infty(0,T;\boldsymbol{H}^1(\Omega))} + \|\boldsymbol{u}_\delta\|_{H^1(0,T;\boldsymbol{L}^2(\Omega))} \leq C, \tag{3.20}$$

$$\tfrac{1}{\delta}\|\hat{\boldsymbol{\phi}}(\boldsymbol{u}_\delta)\|_{L^2(0,T;\boldsymbol{L}^2(\Omega))} \leq C, \tag{3.21}$$

$$\|[\boldsymbol{u}_\delta]_-\|_{L^\infty(0,T;\boldsymbol{L}^2(\Omega))} \leq C\delta^{1/2} \tag{3.22}$$

and

$$\|\boldsymbol{u}_\delta\|_{L^2(0,T;\boldsymbol{H}^2(\Omega))} \leq C. \tag{3.23}$$

Proof: First we show that the solution is unique. Therefore assume that $(\boldsymbol{P_m^\delta})$ has two solutions $\boldsymbol{u}_\delta^1, \boldsymbol{u}_\delta^2$, subtracting them and choosing $\boldsymbol{\chi} \equiv \boldsymbol{d} := \boldsymbol{u}_\delta^1 - \boldsymbol{u}_\delta^2$ gives

$$\varepsilon(\tfrac{\partial \boldsymbol{d}}{\partial t}, \boldsymbol{d}) + \gamma\varepsilon\|\nabla \boldsymbol{d}\|_{\boldsymbol{L}^2}^2 + \tfrac{\gamma}{\varepsilon}((I - \mathbf{1}\textstyle\sum)(\tfrac{1}{\delta}\hat{\boldsymbol{\phi}}(\boldsymbol{u}_\delta^1) - \tfrac{1}{\delta}\hat{\boldsymbol{\phi}}(\boldsymbol{u}_\delta^2) - W\boldsymbol{d}), (I - \fint_\Omega)\boldsymbol{d}) = 0.$$

Since $\sum \boldsymbol{d} = 0$ and $\fint_\Omega \boldsymbol{d} = \fint_\Omega (\boldsymbol{u}_\delta^1 - \boldsymbol{m}) - \fint_\Omega (\boldsymbol{u}_\delta^2 - \boldsymbol{m}) = \mathbf{0}$ it follows that

$$\tfrac{\varepsilon}{2}\tfrac{d}{dt}\|\boldsymbol{d}\|_{\boldsymbol{L}^2}^2 + \gamma\varepsilon\|\nabla \boldsymbol{d}\|_{\boldsymbol{L}^2}^2 + \tfrac{\gamma}{\varepsilon\delta}(\hat{\boldsymbol{\phi}}(\boldsymbol{u}_\delta^1) - \hat{\boldsymbol{\phi}}(\boldsymbol{u}_\delta^2), \boldsymbol{d}) = \tfrac{\gamma}{\varepsilon}(W\boldsymbol{d}, \boldsymbol{d}) \le \tfrac{\gamma}{\varepsilon}\sigma_{max}(W)\|\boldsymbol{d}\|_{\boldsymbol{L}^2}^2.$$

With (3.11) we obtain almost every $t \in (0, T)$

$$\tfrac{\varepsilon}{2}\tfrac{d}{dt}\|\boldsymbol{d}\|_{\boldsymbol{L}^2}^2 \le \tfrac{\gamma}{\varepsilon}\sigma_{max}(W)\|\boldsymbol{d}\|_{\boldsymbol{L}^2}^2.$$

Now Grönwall's inequality gives that $\|\boldsymbol{d}\|_{\boldsymbol{L}^2}^2 = 0$ and thus $\boldsymbol{u}_\delta^1 \equiv \boldsymbol{u}_\delta^2$.
The existence of a solution to $(\boldsymbol{P_m^\delta})$ follows similarly to the scalar case by using a Galerkin approximation, a priori estimates and a standard limit process. Using the assumptions on Ω and the growth property of $D\psi_\delta$, regularity theory gives $\boldsymbol{u}_\delta \in L^2(0, T; \boldsymbol{H}^2(\Omega))$.
Setting now $\boldsymbol{\chi} \equiv \partial \boldsymbol{u}_\delta / \partial t$ in (3.16) gives

$$\varepsilon\|\tfrac{\partial \boldsymbol{u}_\delta}{\partial t}\|_{\boldsymbol{L}^2}^2 + \tfrac{\gamma\varepsilon}{2}\tfrac{d}{dt}\|\nabla \boldsymbol{u}_\delta\|_{\boldsymbol{L}^2}^2 + \tfrac{\gamma}{\varepsilon}((I - \mathbf{1}\textstyle\sum)D\psi_\delta(\boldsymbol{u}_\delta), (I - \fint_\Omega)\tfrac{\partial \boldsymbol{u}_\delta}{\partial t}) = 0$$

and using (3.18) and (3.19) we obtain

$$\varepsilon\|\tfrac{\partial \boldsymbol{u}_\delta}{\partial t}\|_{\boldsymbol{L}^2}^2 + \tfrac{\gamma\varepsilon}{2}\tfrac{d}{dt}\|\nabla \boldsymbol{u}_\delta\|_{\boldsymbol{L}^2}^2 + \tfrac{\gamma}{\varepsilon}(D\psi_\delta(\boldsymbol{u}_\delta), \tfrac{\partial \boldsymbol{u}_\delta}{\partial t}) = 0.$$

Integrating this equation over $(0, t)$ and rearranging gives

$$\int_0^t \varepsilon\|\tfrac{\partial \boldsymbol{u}_\delta}{\partial t}\|_{\boldsymbol{L}^2}^2 ds + \tfrac{\gamma\varepsilon}{2}\|\nabla \boldsymbol{u}_\delta(t)\|_{\boldsymbol{L}^2}^2 + \tfrac{\gamma}{\varepsilon}(\psi_\delta(\boldsymbol{u}_\delta), 1) = \tfrac{\gamma\varepsilon}{2}\|\nabla \boldsymbol{u}_0\|_{\boldsymbol{L}^2}^2 + \tfrac{\gamma}{\varepsilon}(\psi_\delta(\boldsymbol{u}_0), 1) \le C \tag{3.24}$$

since $\boldsymbol{u}_0 \in \mathcal{G}^{\boldsymbol{m}}$.
In particular, it follows that

$$(\psi_\delta(\boldsymbol{u}_\delta), 1) \le C.$$

Using (3.13) gives

$$\tfrac{1}{\delta}(\sum_{n=1}^N [(\boldsymbol{u}_\delta)_n]_-^2, 1) \le C(N, \sigma_{max}(W))$$

and hence

$$\sum_{n=1}^N \|[(\boldsymbol{u}_\delta)_n]_-\|_{\boldsymbol{L}^2}^2 \le C(N, \sigma_{max}(W))\delta.$$

So, we have that $\|[\boldsymbol{u}_\delta(t)]_-\|_{\boldsymbol{L}^2} \leq C(N, \sigma_{max}(W))\delta^{1/2}$ for *a.e.* $t \in (0,T)$ and thus (3.22) follows.
Furthermore, from (3.24) it follows that $\|\nabla \boldsymbol{u}_\delta\|_{\boldsymbol{L}^2} \leq C$ and using the Poincaré inequality

$$\|\eta\|_{L^2} \leq C_P(\|\nabla\eta\|_{L^2} + |(\eta,1)|) \qquad \forall \eta \in H^1(\Omega) \tag{3.25}$$

gives that $\|\boldsymbol{u}_\delta(t)\|^2_{\boldsymbol{H}^1(\Omega)} \leq C$ for *a.e.* $t \in (0,T)$ and thus $\boldsymbol{u}_\delta \in L^\infty(0,T;\boldsymbol{H}^1(\Omega))$.
From (3.24) and (3.13) it also follows that $\left(\frac{\partial \boldsymbol{u}_\delta}{\partial t}\right)_{\delta>0}$ is uniformly bounded in $L^2(0,T;\boldsymbol{L}^2(\Omega))$.
Setting $\boldsymbol{\chi} \equiv \frac{1}{\delta}(I - \mathbf{1}\sum)\hat{\boldsymbol{\phi}}(\boldsymbol{u}_\delta)$ in (3.16) gives

$$\begin{aligned}\tfrac{\varepsilon}{\delta}(\tfrac{\partial \boldsymbol{u}_\delta}{\partial t}, (I - \mathbf{1}\sum)\hat{\boldsymbol{\phi}}(\boldsymbol{u}_\delta)) + \tfrac{\gamma\varepsilon}{\delta}(\nabla \boldsymbol{u}_\delta, \nabla(I - \mathbf{1}\sum)\hat{\boldsymbol{\phi}}(\boldsymbol{u}_\delta)) \\ + \tfrac{\gamma}{\varepsilon\delta}((I - \mathbf{1}\sum)(D\psi_\delta(\boldsymbol{u}_\delta)), (I - \fint_\Omega)(I - \mathbf{1}\sum)\hat{\boldsymbol{\phi}}(\boldsymbol{u}_\delta)) = 0.\end{aligned}$$

Using (3.17) and $(I - \mathbf{1}\sum)(D\psi_\delta(\boldsymbol{u}_\delta)) \equiv (I - \mathbf{1}\sum)[\frac{1}{\delta}\hat{\boldsymbol{\phi}}(\boldsymbol{u}_\delta) - W\boldsymbol{u}_\delta]$ gives

$$\begin{aligned}\tfrac{\varepsilon}{\delta}(\tfrac{\partial \boldsymbol{u}_\delta}{\partial t}, (I - \mathbf{1}\sum)\hat{\boldsymbol{\phi}}(\boldsymbol{u}_\delta)) + \tfrac{\gamma\varepsilon}{\delta}(\nabla \boldsymbol{u}_\delta, \nabla\hat{\boldsymbol{\phi}}(\boldsymbol{u}_\delta)) + \tfrac{\gamma}{\delta^2\varepsilon}((I - \mathbf{1}\sum)\hat{\boldsymbol{\phi}}(\boldsymbol{u}_\delta), (I - \fint_\Omega)(I - \mathbf{1}\sum)\hat{\boldsymbol{\phi}}(\boldsymbol{u}_\delta)) \\ = \tfrac{\gamma}{\varepsilon\delta}((I - \mathbf{1}\sum)W\boldsymbol{u}_\delta, (I - \fint_\Omega)(I - \mathbf{1}\sum)\hat{\boldsymbol{\phi}}(\boldsymbol{u}_\delta)).\end{aligned}$$

Noting that $((I - \fint_\Omega)v, \fint_\Omega v) = 0$ for any $v \in L^2(\Omega)$ and using (3.19) we obtain

$$\begin{aligned}\tfrac{\gamma\varepsilon}{\delta}(\nabla \boldsymbol{u}_\delta, \nabla\hat{\boldsymbol{\phi}}(\boldsymbol{u}_\delta)) + \tfrac{\gamma}{\delta^2\varepsilon}\|(I - \fint_\Omega)(I - \mathbf{1}\sum)\hat{\boldsymbol{\phi}}(\boldsymbol{u}_\delta)\|^2_{\boldsymbol{L}^2} \leq \tfrac{\varepsilon}{\delta}|(\tfrac{\partial \boldsymbol{u}_\delta}{\partial t}, (I - \fint_\Omega)(I - \mathbf{1}\sum)\hat{\boldsymbol{\phi}}(\boldsymbol{u}_\delta))| \\ + \tfrac{\gamma}{\varepsilon\delta}|((I - \mathbf{1}\sum)W\boldsymbol{u}_\delta, (I - \fint_\Omega)(I - \mathbf{1}\sum)\hat{\boldsymbol{\phi}}(\boldsymbol{u}_\delta))|.\end{aligned}$$

Since $\hat{\phi}$ is non-decreasing we have that $\int_0^T(\nabla \boldsymbol{u}_\delta, \nabla\hat{\boldsymbol{\phi}}(\boldsymbol{u}_\delta))dt \geq 0$ and hence Young's inequality and the uniform estimates on $\boldsymbol{u}_\delta \in L^\infty(0,T;\boldsymbol{H}^1(\Omega))$ and $\partial_t \boldsymbol{u}_\delta \in L^2(0,T;\boldsymbol{L}^2(\Omega))$ yield

$$\tfrac{1}{\delta^2}\|(I - \fint_\Omega)(I - \mathbf{1}\sum)\hat{\boldsymbol{\phi}}(\boldsymbol{u}_\delta)\|^2_{L^2(0,T;\boldsymbol{L}^2(\Omega))} \leq C. \tag{3.26}$$

Choosing $\boldsymbol{\chi} = \boldsymbol{u}_\delta$ in (3.16) and using (3.17) we obtain

$$\begin{aligned}0 &= \varepsilon(\tfrac{\partial \boldsymbol{u}_\delta}{\partial t}, \boldsymbol{u}_\delta) + \gamma\varepsilon(\nabla \boldsymbol{u}_\delta, \nabla \boldsymbol{u}_\delta) + \tfrac{\gamma}{\varepsilon}((I - \mathbf{1}\sum)D\psi_\delta(\boldsymbol{u}_\delta), (I - \fint_\Omega)\boldsymbol{u}_\delta) \\ &= \varepsilon(\tfrac{\partial \boldsymbol{u}_\delta}{\partial t}, \boldsymbol{u}_\delta) + \gamma\varepsilon(\nabla \boldsymbol{u}_\delta, \nabla \boldsymbol{u}_\delta) + \tfrac{\gamma}{\varepsilon}(D\psi_\delta(\boldsymbol{u}_\delta), (I - \fint_\Omega)\boldsymbol{u}_\delta).\end{aligned} \tag{3.27}$$

From (3.27) and (3.12) it follows for any constant $\boldsymbol{\xi} \in \mathbb{R}^N$ and for a.e. $t \in (0,T)$ that

$$\begin{aligned}\tfrac{\gamma}{\varepsilon}(D\psi_\delta(\boldsymbol{u}_\delta), \boldsymbol{\xi} - \fint_\Omega \boldsymbol{u}_\delta) &= \tfrac{\gamma}{\varepsilon}(D\psi_\delta(\boldsymbol{u}_\delta), \boldsymbol{\xi} - \boldsymbol{u}_\delta) - \gamma\varepsilon\|\nabla \boldsymbol{u}_\delta\|^2_{\boldsymbol{L}^2} - \varepsilon(\tfrac{\partial \boldsymbol{u}_\delta}{\partial t}, \boldsymbol{u}_\delta) \\ &\leq \tfrac{\gamma}{\varepsilon}(\psi_\delta(\boldsymbol{\xi}) - \psi_\delta(\boldsymbol{u}_\delta), 1) + \tfrac{\gamma\sigma_{max}(W)}{2\varepsilon}\|\boldsymbol{\xi} - \boldsymbol{u}_\delta\|^2_{\boldsymbol{L}^2} + \varepsilon\|\tfrac{\partial \boldsymbol{u}_\delta}{\partial t}\|_{\boldsymbol{L}^2}\|\boldsymbol{u}_\delta\|_{\boldsymbol{L}^2}.\end{aligned}$$

Setting now $\boldsymbol{\xi} \equiv (\fint_\Omega \boldsymbol{u}_\delta) \pm \beta \mathbf{e}^n$, where $\mathbf{e}^n$ is the n-th unit vector, $n = 1, ..., N$, and $\beta \in (0,1)$ such that $\beta\mathbf{1} < \fint_\Omega \boldsymbol{u}_0 < (1-\beta)\mathbf{1}$ we obtain

$$\begin{aligned}\tfrac{\gamma}{\delta\varepsilon}(\hat{\boldsymbol{\phi}}(\boldsymbol{u}_\delta), \pm\beta\mathbf{e}^n) &\leq \tfrac{\gamma}{\varepsilon}(W\boldsymbol{u}_\delta, \pm\beta\mathbf{e}^n) - \tfrac{\gamma}{2\varepsilon}(W(\fint_\Omega \boldsymbol{u}_\delta \pm \beta\mathbf{e}^n), \fint_\Omega \boldsymbol{u}_\delta \pm \beta\mathbf{e}^n) + \tfrac{\gamma}{2\varepsilon}(W\boldsymbol{u}_\delta, \boldsymbol{u}_\delta) \\ &\quad - \tfrac{\gamma}{\delta\varepsilon}(\hat{\psi}(\boldsymbol{u}_\delta), 1) + \tfrac{\gamma\sigma_{max}(W)}{2\varepsilon}\|\fint_\Omega \boldsymbol{u}_\delta \pm \beta\mathbf{e}^n - \boldsymbol{u}_\delta\|^2_{\boldsymbol{L}^2} + \varepsilon\|\tfrac{\partial \boldsymbol{u}_\delta}{\partial t}\|_{\boldsymbol{L}^2}\|\boldsymbol{u}_\delta\|_{\boldsymbol{L}^2} \\ &\leq \tfrac{\gamma\sigma_{max}(W)}{\varepsilon}\|\boldsymbol{u}_\delta\|_{\boldsymbol{L}^2} - \tfrac{\gamma\sigma_{min}(W)}{2\varepsilon}\|\fint_\Omega \boldsymbol{u}_\delta \pm \beta\mathbf{e}^n\|^2_{\boldsymbol{L}^2} + \tfrac{\gamma\sigma_{max}(W)}{\varepsilon}\|\boldsymbol{u}_\delta\|^2_{\boldsymbol{L}^2} \\ &\quad + \tfrac{\gamma\sigma_{max}(W)}{2\varepsilon}\|\fint_\Omega \boldsymbol{u}_\delta \pm \beta\mathbf{e}^n\|^2_{\boldsymbol{L}^2} + \varepsilon\|\tfrac{\partial \boldsymbol{u}_\delta}{\partial t}\|_{\boldsymbol{L}^2}\|\boldsymbol{u}_\delta\|_{\boldsymbol{L}^2}\end{aligned}$$

where we used that $\hat{\psi}(\boldsymbol{\xi}) = 0$ and $\hat{\psi}(\boldsymbol{u}_\delta) \geq 0$. By $\sigma_{min}(W)$ we denote the minimal eigenvalue of W. Using that $-\sigma_{min}(W) \leq |||W|||$ and $\sigma_{max}(W) \leq |||W|||$ where $|||W|||$ is the spectral norm of W, and $\mathbf{0} < \fint_\Omega \boldsymbol{u}_\delta \pm \beta\mathbf{e}^n < \mathbf{1}$ the above estimate gives that

$$\tfrac{|\Omega|}{\delta}|\fint_\Omega \{(\hat{\boldsymbol{\phi}}(\boldsymbol{u}_\delta)\}_n| \leq C(1 + \|\boldsymbol{u}_\delta\|^2_{\boldsymbol{L}^2} + \|\tfrac{\partial \boldsymbol{u}_\delta}{\partial t}\|_{\boldsymbol{L}^2}\|\boldsymbol{u}_\delta\|_{\boldsymbol{L}^2})$$

for all $n = 1, ..., N$ and hence

$$\tfrac{|\Omega|}{\delta}\|\fint_\Omega \hat{\boldsymbol{\phi}}(\boldsymbol{u}_\delta)\| \leq C(1 + \|\boldsymbol{u}_\delta\|^2_{\boldsymbol{L}^2} + \|\tfrac{\partial \boldsymbol{u}_\delta}{\partial t}\|_{\boldsymbol{L}^2}\|\boldsymbol{u}_\delta\|_{\boldsymbol{L}^2}) \tag{3.28}$$

where C depends on $\varepsilon, \gamma, N, |||W|||$ and $\sigma_{max}(W)$ but not on δ. Integrating (3.28) over $t \in (0,T)$ and using the same arguments as in Step 3 in the proof of Theorem 2.2.1, i.e. in particular that $\boldsymbol{u}_\delta \in L^\infty(0,T;\boldsymbol{H}^1(\Omega)) \cap H^1(0,T;\boldsymbol{L}^2(\Omega))$ yields that

$$\tfrac{1}{\delta}\|\fint_\Omega \hat{\boldsymbol{\phi}}(\boldsymbol{u}_\delta)\|_{L^2(0,T;\boldsymbol{L}^2(\Omega))} \leq C. \tag{3.29}$$

It follows that

$$\begin{aligned}\tfrac{1}{\delta}\|\fint_\Omega (I - \mathbf{1}\sum)\hat{\boldsymbol{\phi}}(\boldsymbol{u}_\delta)\|_{L^2(0,T;\boldsymbol{L}^2(\Omega))} &\leq \tfrac{1}{\delta}\|\fint_\Omega \hat{\boldsymbol{\phi}}(\boldsymbol{u}_\delta)\|_{L^2(0,T;\boldsymbol{L}^2(\Omega))} + \tfrac{1}{\delta}\|\mathbf{1}\sum\fint_\Omega \hat{\boldsymbol{\phi}}(\boldsymbol{u}_\delta)\|_{L^2(0,T;\boldsymbol{L}^2(\Omega))} \\ &\leq C\end{aligned}$$

and together with (3.26) we obtain

$$\tfrac{1}{\delta}\|(I-\mathbf{1}\textstyle\sum)\hat{\boldsymbol{\phi}}(\boldsymbol{u}_\delta)\|_{L^2(0,T;\boldsymbol{L}^2(\Omega))}\le C. \tag{3.30}$$

From (3.17) it follows that $\min\{\boldsymbol{u}_\delta(x,t)\}_n \le \frac{1}{N} \le \max\{\boldsymbol{u}_\delta(x,t)\}_n$ for almost every $(x,t)\in\Omega_T$ and since $\hat{\phi}$ is monotonically increasing we obtain

$$\min_{n=1,\dots,N}\hat{\phi}(\{\boldsymbol{u}_\delta(x,t)\}_n)\le\hat{\phi}(\tfrac{1}{N})=0=\max_{n=1,\dots,N}\hat{\phi}(\{\boldsymbol{u}_\delta(x,t)\}_n).$$

Noting this and (3.30) yields that

$$\begin{aligned}\tfrac{1}{\delta}\|\textstyle\sum\hat{\boldsymbol{\phi}}(\boldsymbol{u}_\delta)\|_{L^2(0,T;L^2(\Omega))} &= \tfrac{1}{\delta}\|\hat{\phi}(\tfrac{1}{N})-\mathbf{1}\textstyle\sum\hat{\boldsymbol{\phi}}(\boldsymbol{u}_\delta)\|_{L^2(0,T;L^2(\Omega))}\\ &\le \tfrac{1}{\delta}\|(I-\mathbf{1}\textstyle\sum)\hat{\boldsymbol{\phi}}(\boldsymbol{u}_\delta)\|_{L^2(0,T;\boldsymbol{L}^2(\Omega))}\le C.\end{aligned}$$

Together with (3.30) we obtain

$$\tfrac{1}{\delta}\|\hat{\boldsymbol{\phi}}(\boldsymbol{u}_\delta)\|_{L^2(0,T;\boldsymbol{L}^2(\Omega))}\le\tfrac{1}{\delta}\|(I-\mathbf{1}\textstyle\sum)\hat{\boldsymbol{\phi}}(\boldsymbol{u}_\delta)\|_{L^2(0,T;\boldsymbol{L}^2(\Omega))}+\tfrac{1}{\delta}\|\mathbf{1}\textstyle\sum\hat{\boldsymbol{\phi}}(\boldsymbol{u}_\delta)\|_{L^2(0,T;\boldsymbol{L}^2(\Omega))}\le C.$$

We refer to [7] where similar arguments have been used in the context of a Cahn-Hilliard system with a logarithmic free energy. Finally, (3.23) follows from (3.16), (3.20), (3.21) and standard parabolic regularity theory.

□

For the uniqueness proof in the next theorem we are using some graph theory and therefore we state the definitions of a graph, a path and connectivity of a graph. An introduction to graph theory can be found for example in [118].

Definition 3.2.2. *(i) A graph consists of a non-empty finite set of elements called vertices and a finite family of unordered pairs of elements called edges.*
(ii) A path in a graph is a sequence of vertices such that from each of its vertices there is an edge to the next vertex in the sequence.
(iii) A graph is connected if there is a path between each pair of vertices.

Theorem 3.2.3. *Let $\Omega\subset\mathbb{R}^d$ be a bounded domain and assume that either Ω is convex or fulfils $\partial\Omega\in C^{1,1}$. Let $\boldsymbol{u}_\delta(x,0)=\boldsymbol{u}_0(x)\in\boldsymbol{H}^1(\Omega)$ with $\boldsymbol{u}_0\ge\mathbf{0}, \fint_\Omega \boldsymbol{u}_0=\boldsymbol{m}$ and $\sum_{i=1}^N(u_0)_i=1$ a.e. in Ω and such that a $\beta\in(0,1)$ exists with $\beta\mathbf{1}<\fint_\Omega\boldsymbol{u}_0<(1-\beta)\mathbf{1}$. Then there exists a unique solution $(\boldsymbol{u},\boldsymbol{\mu},\boldsymbol{\lambda},\Lambda)$ to (3.5) - (3.8) with the following*

properties:

$$\boldsymbol{u} \in L^\infty(0,T;\boldsymbol{H}^1(\Omega)) \cap H^1(0,T;\boldsymbol{L}^2(\Omega)) \cap L^2(0,T;\boldsymbol{H}^2(\Omega)), \tag{3.31}$$

$$\boldsymbol{\mu} \in L^2(0,T;\boldsymbol{L}^2(\Omega)), \tag{3.32}$$

$$\boldsymbol{\lambda} \in \boldsymbol{L}^2(0,T) \text{ and } \sum_{i=1}^{N} \lambda_i = 0 \text{ for almost all } t \in (0,T), \tag{3.33}$$

$$\Lambda \in L^2(0,T;L^2(\Omega)). \tag{3.34}$$

Proof: As the bounds (3.20), (3.21) and (3.23) are independent of δ, it follows that there exists $\boldsymbol{u} \in L^\infty(0,T;\boldsymbol{H}^1(\Omega)) \cap H^1(0,T;\boldsymbol{L}^2(\Omega)) \cap L^2(0,T;\boldsymbol{H}^2(\Omega))$, $\xi \in L^2(0,T;L^2(\Omega))$ and $\boldsymbol{\zeta} \in \boldsymbol{L}^2(0,T)$ and a subsequence $\{\boldsymbol{u}_{\delta'}\}$ such that as $\delta' \to 0$

$$\begin{aligned} \boldsymbol{u}_{\delta'} \to \boldsymbol{u} \quad \text{in} \quad & L^\infty(0,T;\boldsymbol{H}^1(\Omega)) \text{ weak-star,} \\ & H^1(0,T;\boldsymbol{L}^2(\Omega)) \cap L^2(0,T;\boldsymbol{H}^2(\Omega)) \text{ weakly, and} \\ & L^2(0,T;\boldsymbol{L}^2(\Omega)) \text{ strongly,} \end{aligned} \tag{3.35}$$

$$\tfrac{1}{\delta'}\textstyle\sum \hat{\boldsymbol{\phi}}(\boldsymbol{u}_{\delta'}) \to \xi \quad \text{in} \quad L^2(0,T;L^2(\Omega)) \text{ weakly,} \tag{3.36}$$

$$\tfrac{1}{\delta'} \fint_\Omega \hat{\boldsymbol{\phi}}(\boldsymbol{u}_{\delta'}) \to \boldsymbol{\zeta} \quad \text{in} \quad \boldsymbol{L}^2(0,T) \text{ weakly,} \tag{3.37}$$

where the third convergence in (3.35) follows from the first two weak convergences in (3.35) [85].
Taking the limit $\delta' \to 0$ in (3.22) gives that $[\boldsymbol{u}]_- = \boldsymbol{0}$ and thus $\boldsymbol{u}(x,t) \geq \boldsymbol{0}$ for almost every $(x,t) \in \Omega_T$.

Since $\boldsymbol{u}_\delta \in L^2(0,T;\boldsymbol{H}^2(\Omega))$ we can use the strong formulation of (3.16) and obtain

$$\varepsilon \tfrac{\partial \boldsymbol{u}_\delta}{\partial t} - \gamma\varepsilon\Delta\boldsymbol{u}_\delta + \tfrac{\gamma}{\varepsilon} D\psi_\delta(\boldsymbol{u}_\delta) - \tfrac{\gamma}{\varepsilon}\textstyle\sum D\psi_\delta(\boldsymbol{u}_\delta)\mathbf{1} - \tfrac{\gamma}{\varepsilon} \fint_\Omega (I - \mathbf{1}\textstyle\sum) D\psi_\delta(\boldsymbol{u}_\delta) = \boldsymbol{0}.$$

Using $D\psi_\delta(\boldsymbol{u}_\delta) = \frac{1}{\delta}\hat{\boldsymbol{\phi}}(\boldsymbol{u}_\delta) - W\boldsymbol{u}_\delta$ and defining $\Lambda_\delta := \frac{\gamma}{\delta}\sum\hat{\boldsymbol{\phi}}(\boldsymbol{u}_\delta) - \gamma\sum W\boldsymbol{u}_\delta$, $\boldsymbol{\lambda}_\delta := \frac{\gamma}{\delta}\fint_\Omega \hat{\boldsymbol{\phi}}(\boldsymbol{u}_\delta) - \gamma\fint_\Omega W\boldsymbol{u}_\delta - \gamma\fint_\Omega \Lambda_\delta\mathbf{1}$ and $\boldsymbol{\mu}_\delta := -\frac{\gamma}{\delta}\hat{\boldsymbol{\phi}}(\boldsymbol{u}_\delta)$ the above equation becomes

$$\varepsilon \tfrac{\partial \boldsymbol{u}_\delta}{\partial t} - \gamma\varepsilon\Delta\boldsymbol{u}_\delta - \tfrac{\gamma}{\varepsilon} W\boldsymbol{u}_\delta - \tfrac{1}{\varepsilon}\boldsymbol{\mu}_\delta - \tfrac{1}{\varepsilon}\Lambda_\delta\mathbf{1} - \tfrac{1}{\varepsilon}\boldsymbol{\lambda}_\delta = \boldsymbol{0}. \tag{3.38}$$

Noting that $\Lambda_\delta \in L^2(0,T;L^2(\Omega))$ and $\boldsymbol{\lambda}_\delta \in \boldsymbol{L}^2(0,T)$ gives together with the a priori estimates on $\boldsymbol{u}_\delta$ that $\boldsymbol{\mu}_\delta \in L^2(0,T;\boldsymbol{L}^2(\Omega))$.
Hence there exists $\boldsymbol{\mu} \in L^2(0,T;\boldsymbol{L}^2(\Omega))$ such that for a subsequence

$$\boldsymbol{\mu}_{\delta'} \rightharpoonup \boldsymbol{\mu} \quad \text{in } L^2(0,T;\boldsymbol{L}^2(\Omega)) \quad \text{as } \delta' \to 0.$$

Since $\boldsymbol{\mu}$ is the weak limit of functions which are componentwise non-negative we obtain $\boldsymbol{\mu} \geq \mathbf{0}$ a.e. in Ω_T. Furthermore, from (3.35c) it follows that $\sum_{i=1}^{N} u_i = 1$ and $\frac{d}{dt} \int_\Omega \boldsymbol{u} = \mathbf{0}$ and hence $\fint_\Omega \boldsymbol{u} = \boldsymbol{m}$. Note that $\sum_{i=1}^{N} (\lambda_\delta)_i = 0$ and hence $\sum_{i=1}^{N} \lambda_i = 0$.
In order to show that $(\boldsymbol{\mu}, \boldsymbol{u}) = 0$ we first note that

$$(\boldsymbol{\mu}_\delta, \boldsymbol{u}_\delta) = -\tfrac{\gamma}{\delta}(\hat{\boldsymbol{\phi}}(\boldsymbol{u}_\delta), \boldsymbol{u}_\delta) \leq 0,$$

and using that $\boldsymbol{u}_\delta \to \boldsymbol{u}$ and $\boldsymbol{\mu}_\delta \rightharpoonup \boldsymbol{\mu}$ in $L^2(0,T,\boldsymbol{L}^2(\Omega))$ it follows that $(\boldsymbol{u}, \boldsymbol{\mu}) \leq 0$. However, since $\boldsymbol{u} \geq \mathbf{0}$ and $\boldsymbol{\mu} \geq \mathbf{0}$ we have that $(\boldsymbol{u}, \boldsymbol{\mu}) = 0$ a.e. in $(0,T)$.
It remains to show uniqueness. Assume that there are two solutions $(\boldsymbol{u}^1, \boldsymbol{\mu}^1, \boldsymbol{\lambda}^1, \Lambda^1)$ and $(\boldsymbol{u}^2, \boldsymbol{\mu}^2, \boldsymbol{\lambda}^2, \Lambda^2)$. Then we define $\bar{\boldsymbol{u}} = \boldsymbol{u}^1 - \boldsymbol{u}^2, \bar{\boldsymbol{\mu}} = \boldsymbol{\mu}^1 - \boldsymbol{\mu}^2$. Multiplying the difference of the equation (3.5) for $\boldsymbol{u}^1$ and $\boldsymbol{u}^2$ with $\bar{\boldsymbol{u}}$ gives, after integration and using $\int_\Omega \mathbf{1} \cdot \bar{\boldsymbol{u}} = 0$, that

$$\varepsilon \tfrac{d}{dt} \int_\Omega |\bar{\boldsymbol{u}}|^2 + \gamma\varepsilon \int_\Omega |\nabla \bar{\boldsymbol{u}}|^2 - \tfrac{1}{\varepsilon} \int_\Omega (\boldsymbol{\mu}^1 - \boldsymbol{\mu}^2) \cdot (\boldsymbol{u}^1 - \boldsymbol{u}^2) \leq \tfrac{\gamma \sigma_{max}(W)}{\varepsilon} \int_\Omega |\bar{\boldsymbol{u}}|^2. \tag{3.39}$$

The complementarity conditions (3.7)-(3.8) imply that $(\boldsymbol{\mu}^1 - \boldsymbol{\mu}^2) \cdot (\boldsymbol{u}^1 - \boldsymbol{u}^2) \leq 0$ and hence we deduce that

$$\varepsilon \tfrac{d}{dt} \int_\Omega |\bar{\boldsymbol{u}}|^2 + \gamma\varepsilon \int_\Omega |\nabla \bar{\boldsymbol{u}}|^2 \leq \tfrac{\gamma \sigma_{max}(W)}{\varepsilon} \int_\Omega |\bar{\boldsymbol{u}}|^2.$$

Using a Grönwall argument now gives uniqueness of $\boldsymbol{u}$. Hence $\boldsymbol{\mu} + \boldsymbol{\lambda} + \Lambda \mathbf{1}$ is uniquely given through equation (3.5).
Now we show the uniqueness of the Lagrange multipliers $\boldsymbol{\lambda}, \Lambda$ and $\boldsymbol{\mu}$. For what follows we fix $t \in (0,T)$ and using that $\boldsymbol{u}_\delta \in L^2(0,T;\boldsymbol{H}^2(\Omega))$ and hence continuous for $d \leq 3$, we define

$$A_{ij} := \{x \in \Omega : u_i(x,t) > 0, u_j(x,t) > 0\}$$

and

$$A_{ij}^\rho := \{x \in \Omega : u_i(x,t) > \rho, u_j(x,t) > \rho\}.$$

Claim: $\lambda_i - \lambda_j$ is uniquely defined for all pairs (i,j) with $|A_{ij}| > 0$.
For (i,j) with $|A_{ij}| > 0$ we find a $\rho > 0$ such that $|A_{ij}^\rho| > 0$. Using (3.5) and recalling that $\mathbf{e}^k$ is the k-th unit vector we obtain that on A_{ij}^ρ

$$(\varepsilon \tfrac{\partial \boldsymbol{u}}{\partial t} - \gamma\varepsilon \Delta \boldsymbol{u} - \tfrac{\gamma}{\varepsilon} W \boldsymbol{u} - \tfrac{1}{\varepsilon} \boldsymbol{\lambda}) \cdot (\mathbf{e}^i - \mathbf{e}^j) = 0 \tag{3.40}$$

where we have used that $\mu_i = \mu_j = 0$ on A_{ij}^ρ. We hence conclude

$$\lambda_i - \lambda_j = \tfrac{1}{|A_{ij}^\rho|} \int\limits_{A_{ij}^\rho} \left[\varepsilon^2 \tfrac{\partial u_i}{\partial t} - \gamma\varepsilon^2 \Delta u_i - \gamma (Wu)_i - \varepsilon^2 \tfrac{\partial u_j}{\partial t} + \gamma\varepsilon^2 \Delta u_j + \gamma (Wu)_j \right].$$

This implies that the difference $\lambda_i - \lambda_j$ is uniquely defined if $|A_{ij}| > 0$.
We now introduce a graph $\mathcal{E}$ with vertices $\{1, ..., N\}$ and edges $\{\{i, j\} : |A_{ij}| > 0\}$.
Claim: $\mathcal{E}$ is a connected graph.
We define the following sets of indices

$$\mathcal{I} = \{i \in \{1, ..., N\} : \text{ there is a path from 1 to } i\} \quad \text{and} \quad \mathcal{J} = \{1, ..., N\} \setminus \mathcal{I}.$$

We need to show that $\mathcal{J} = \emptyset$ and therefore we assume this is not true. We set

$$v = \sum_{i \in \mathcal{I}} u_i \quad \text{and} \quad w = \sum_{j \in \mathcal{J}} u_j$$

and note that $v \geq 0, w \geq 0$ and $v + w = 1$. Now one observes that the set

$$A := \{x \in \Omega : v(x) > 0 \text{ and } w(x) > 0\}$$

has measure zero. This is true because otherwise there exist $i \in \mathcal{I}$ and $j \in \mathcal{J}$ such that $|A_{ij}| > 0$ which contradicts the definition of $\mathcal{I}$. We hence obtain that v only attains the values 0 and 1. However, since $\mathcal{J} \neq \emptyset$ we obtain that v is not constant. Since a H^1-function that attains finitely many values has to be constant we obtain a contradiction.
Hence $\mathcal{J} = \emptyset$ and the graph $\mathcal{E}$ is connected. This implies that the differences $\lambda_i - \lambda_j$ are for all $i, j \in \{1, ..., N\}$ uniquely defined. In particular we obtain that $\lambda_1 - \lambda_j = \alpha_j$ for all $j = 2, ..., N$. Summing these equations over j and using that $\sum\limits_{i=1}^{N} \lambda_i = 0$ we obtain the uniqueness of $\boldsymbol{\lambda}$.
Now we show the uniqueness of Λ. For any $x_0 \in \Omega$ we can find a $\rho > 0$ and an $i \in \{1, ..., N\}$ such that $x_0 \in A_i^\rho := \{x \in \Omega : u_i(x, t) > \rho\}$ and $|A_i^\rho| > 0$. On A_i^ρ we know that $\mu_i = 0$ and hence we can define

$$\Lambda = (\varepsilon^2 \tfrac{\partial \boldsymbol{u}}{\partial t} - \gamma\varepsilon^2 \Delta \boldsymbol{u} - \gamma W \boldsymbol{u} - \boldsymbol{\lambda})_i. \tag{3.41}$$

The Lagrange multiplier Λ is well defined and unique since

$$(\varepsilon \tfrac{\partial \boldsymbol{u}}{\partial t} - \gamma\varepsilon \Delta \boldsymbol{u} - \tfrac{\gamma}{\varepsilon} W \boldsymbol{u} - \tfrac{1}{\varepsilon} \boldsymbol{\lambda})_i(x, t) = (\varepsilon \tfrac{\partial \boldsymbol{u}}{\partial t} - \gamma\varepsilon \Delta \boldsymbol{u} - \tfrac{\gamma}{\varepsilon} W \boldsymbol{u} - \tfrac{1}{\varepsilon} \boldsymbol{\lambda})_j(x, t)$$

for almost every $x \in A_{ij}$.
As t is chosen arbitrarily the Lagrange multipliers $\boldsymbol{\lambda}$ and Λ and hence $\boldsymbol{\mu}$ are unique.
□

Remark 3.2.4. *(i) It can be shown that* $(\boldsymbol{P_m})$ *has a unique solution. Hence we can conclude that for all solutions to* $(\boldsymbol{P_m})$ *there exist Lagrange multipliers* $\boldsymbol{\mu}, \boldsymbol{\lambda}, \Lambda$ *such that (3.5) - (3.8) hold.*
(ii) Rodrigues and Santos [102] showed the existence of a solution for the vector-valued Allen-Cahn equation without volume constraints by using a representation of the Lagrange multipliers which cannot be used directly for a numerical approach. They substitute u_N *by* $1 - \sum_{i=1}^{N-1} u_i$ *and consider a system of parabolic variational inequalities in* $\mathbb{R}^{N-1}$.

3.3 Discretisation and primal-dual active set method

First, we discretise $(\boldsymbol{P_m})$ in time using an implicit Euler discretisation. We denote the time-step by τ, which can be a variable time-step, $t_0 = 0$, $t_n := t_{n-1} + \tau$ and $\boldsymbol{u}^n \approx \boldsymbol{u}(., t_n)$.
$(\boldsymbol{P_m^\tau})$ *Given* $\boldsymbol{u}^{n-1} \in \mathcal{G}^{\boldsymbol{m}}$ *find* $\boldsymbol{u} = \boldsymbol{u}^n \in \mathcal{G}^{\boldsymbol{m}}$ *such that*

$$\tfrac{\varepsilon}{\tau}(\boldsymbol{u} - \boldsymbol{u}^{n-1}, \boldsymbol{\eta} - \boldsymbol{u}) + \gamma\varepsilon(\nabla \boldsymbol{u}, \nabla \boldsymbol{\eta} - \nabla \boldsymbol{u}) \geq \tfrac{\gamma}{\varepsilon}(W\boldsymbol{u}, \boldsymbol{\eta} - \boldsymbol{u}) \quad \forall \boldsymbol{\eta} \in \mathcal{G}^{\boldsymbol{m}}. \tag{3.42}$$

For simplicity we denote by $\boldsymbol{u}$ the time discrete solution at time t_n. This discretisation can also be seen as the Euler-Lagrange equation of an implicit time discretisation of the L_2 gradient flow of the energy E, which is given as

$$\min \mathcal{E}(\boldsymbol{u}) := \int_\Omega \left\{ \tfrac{\gamma\varepsilon}{2}|\nabla \boldsymbol{u}|^2 + \tfrac{\gamma}{\varepsilon}\psi(\boldsymbol{u}) \right\} dx + \tfrac{\varepsilon}{2\tau}\|\boldsymbol{u} - \boldsymbol{u}^{n-1}\|^2_{\boldsymbol{L^2}}.$$

As in Lemma 3.1.1 one can reformulate $(\boldsymbol{P_m^\tau})$ by using scaled Lagrange-multipliers $\boldsymbol{\mu} \in \boldsymbol{L}^2(\Omega)$ for the inequality constraint $\boldsymbol{u} \geq \boldsymbol{0}$, $\boldsymbol{\lambda} \in S$ for the constraint $\boldsymbol{P}_S(\fint_\Omega \boldsymbol{u} - \boldsymbol{m}) = \boldsymbol{0}$ and $\Lambda \in L^2(\Omega)$ for the sum constraint $\sum_{i=1}^N u_i = 1$ to obtain:

$$\tfrac{\varepsilon^2}{\tau}(\boldsymbol{u} - \boldsymbol{u}^{n-1}) - \gamma\varepsilon^2\Delta\boldsymbol{u} - \gamma W\boldsymbol{u} - \boldsymbol{\mu} - \boldsymbol{\lambda} - \Lambda\boldsymbol{1} = \boldsymbol{0} \qquad \text{a.e. in } \Omega, \tag{3.43}$$

$$\tfrac{\partial \boldsymbol{u}}{\partial \nu} = \boldsymbol{0} \qquad \text{a.e. on } \partial\Omega, \tag{3.44}$$

$$\boldsymbol{P}_S(\fint_\Omega \boldsymbol{u} - \boldsymbol{m}) = \boldsymbol{0} \tag{3.45}$$

together with the complementary conditions

$$\boldsymbol{u} \geq \mathbf{0} \quad \text{a.e. in } \Omega, \tag{3.46}$$

$$\boldsymbol{\mu} \geq \mathbf{0} \quad \text{a.e. in } \Omega, \tag{3.47}$$

$$(\boldsymbol{\mu}, \boldsymbol{u}) = 0. \tag{3.48}$$

The complementary conditions (3.46) - (3.48) can be reformulated using active sets based on the primal variable $\boldsymbol{u}$ and the dual variable $\boldsymbol{\mu}$ such that for any $c > 0$ and for all $i \in \{1, ..., N\}$

$$u_i = 0 \text{ a.e. in } \mathcal{A}_i, \tag{3.49}$$

$$\mu_i = 0 \text{ a.e. in } \mathcal{I}_i := \Omega \setminus \mathcal{A}_i, \tag{3.50}$$

where

$$\mathcal{A}_i = \{x \in \Omega \,|\, c(u(x))_i - (\mu(x))_i < 0\}. \tag{3.51}$$

Before applying the primal-dual active set method to the vector-valued Allen-Cahn equation with volume constraints we first need to discretise.
For the discretisation in space we use again a finite element approximation. We use the notation introduced in Section 2.4.1 and we set $\boldsymbol{S}_h = (S_h)^N$. Then $\boldsymbol{u}_j \in \mathbb{R}^N$ for $j = 1, \ldots, J$ denote the coefficients of the basis representation of $\boldsymbol{u}_h$ in $\boldsymbol{S}_h$ which is given by $\boldsymbol{u}_h = \sum_{j \in \mathcal{J}} \boldsymbol{u}_j \chi_j$. Additionally we introduce the vector of coefficients $\underline{\boldsymbol{u}} = (\underline{u}_1, \underline{u}_2, ..., \underline{u}_N)$ where $\underline{u}_i \in \mathbb{R}^J$ is the vector of coefficients of $(u_i)_h$ for $i = 1, ..., N$. In general we use the notation $\underline{b}$ for a vector in $\mathbb{R}^J$, $\boldsymbol{b}$ for a vector in $\mathbb{R}^N$ and $\underline{\boldsymbol{b}}$ for a vector in $\mathbb{R}^{JN}$.
Furthermore, we introduce the sets

$$\mathcal{G}_h := \{\boldsymbol{\chi} \in \boldsymbol{S}_h |\ \boldsymbol{\chi} \geq \mathbf{0} \text{ and } \sum_{i=1}^{N} (\chi_i)_j = 1 \ \ \forall j \in \mathcal{J}\}$$

and

$$\mathcal{G}_h^{\boldsymbol{m}} := \{\boldsymbol{\eta} \in \mathcal{G}_h | \fint_{\Omega} \boldsymbol{\eta} - \boldsymbol{m} = \mathbf{0}\}.$$

Here $(\chi_i)_j$ denotes the j-th node of the i-th component χ_i of $\boldsymbol{\chi}$.
We now introduce the following finite element approximations of $(\boldsymbol{P}_{\boldsymbol{m}}^{\boldsymbol{\tau}})$ given by (3.42). In the following we consider a fixed time step $\tau = t_n - t_{n-1}$ and omit in some places the superscript n:
Given $\boldsymbol{u}_h^{n-1} \in \mathcal{G}_h^{\boldsymbol{m}}$ *find* $\boldsymbol{u}_h = \boldsymbol{u}_h^n \in \mathcal{G}_h^{\boldsymbol{m}}$ *such that*

$$(\tfrac{\varepsilon}{\tau}(\boldsymbol{u}_h - \boldsymbol{u}_h^{n-1}) - \tfrac{\gamma}{\varepsilon} W \boldsymbol{u}_h, \boldsymbol{\chi} - \boldsymbol{u}_h)_h + \gamma\varepsilon(\nabla \boldsymbol{u}_h, \nabla(\boldsymbol{\chi} - \boldsymbol{u}_h)) \geq 0 \ \ \forall \boldsymbol{\chi} \in \mathcal{G}_h^{\boldsymbol{m}}. \tag{3.52}$$

Due to the use of piecewise linear finite elements and nodal basis functions the reformulation of (3.52) with Lagrange multipliers $\boldsymbol{\mu}_h \in \boldsymbol{S}_h$ can be stated as follows: *Find* $\boldsymbol{u}_h \in \boldsymbol{S}_h$, $\boldsymbol{\mu}_h \in \boldsymbol{S}_h$, $\boldsymbol{\lambda} \in S$ *and* $\Lambda \in S_h$ *such that*

$$\begin{aligned}\tfrac{\varepsilon^2}{\tau}(\boldsymbol{u}_h, \boldsymbol{\varphi})_h - \gamma(W\boldsymbol{u}_h, \boldsymbol{\varphi})_h + \gamma\varepsilon^2(\nabla\boldsymbol{u}_h, \nabla\boldsymbol{\varphi}) - (\boldsymbol{\mu}_h, \boldsymbol{\varphi})_h - (\boldsymbol{\lambda}, \boldsymbol{\varphi}) - (\Lambda\mathbf{1}, \boldsymbol{\varphi})_h \\ = \tfrac{\varepsilon^2}{\tau}(\boldsymbol{u}_h^{n-1}, \boldsymbol{\varphi})_h \quad \forall \boldsymbol{\varphi} \in \boldsymbol{S}_h\,,\end{aligned} \tag{3.53}$$

$$\sum_{i=1}^{N}(u_i)_j = 1 \quad \forall\, j \in \mathcal{J}, \tag{3.54}$$

$$\boldsymbol{P}_S(\sum_{j\in\mathcal{J}} m_j\boldsymbol{u}_j - \sum_{j\in\mathcal{J}} m_j\boldsymbol{m}) = \mathbf{0}\,, \tag{3.55}$$

$$\boldsymbol{\mu}_j \geq \mathbf{0},\ \boldsymbol{u}_j \geq \mathbf{0} \quad \forall\, j \in \mathcal{J}, \tag{3.56}$$

$$(\boldsymbol{u}_j, \boldsymbol{\mu}_j) = 0 \quad \forall\, j \in \mathcal{J}. \tag{3.57}$$

In the following we will write $\boldsymbol{\lambda} \in S$ as $(\lambda_1, \lambda_2, ..., \lambda_{N-1}, -\lambda_1 - ... - \lambda_{N-1})^T$ thus eliminating λ_N. Using (3.54) we can restate (3.55) as

$$\sum_{j\in\mathcal{J}} m_j((u_i)_j - (u_N)_j) = \sum_{j\in\mathcal{J}} m_j(m^i - m^N)$$

for $i \in \{1, ..., N-1\}$.
Applying now the PDAS-method to (3.53)-(3.57) we obtain the following algorithm. Here we use the notation $\boldsymbol{u}_i^k$ and $\boldsymbol{u}_i^{n-1}$ where the k denotes the k-th iteration in the PDAS algorithm and $n-1$ is the $(n-1)$-st time-step. This is of course a slight misuse of notation for $k = n-1$.

Primal-Dual Active Set Algorithm (PDAS-I):

0. Set $k = 0$ and initialise $\mathcal{A}_i^0$, $i \in \{1, ..., N\}$.

1. Define $\mathcal{I}_i^k = \mathcal{J} \setminus \mathcal{A}_i^k$ for all $i \in \{1, ..., N\}$.
   Set $(u_i^k)_j = 0$ for $j \in \mathcal{A}_i^k$ and $(\mu_i^k)_j = 0$ for $j \in \mathcal{I}_i^k$ for all $i \in \{1, ..., N\}$.

2. Solve the discrete PDE (3.53) with the constraints (3.54) and (3.55) to obtain

$(u_i^k)_j, \Lambda_j^k$ and λ_i^k for all (i,j) such that $j \in \mathcal{I}_i^k$, $i \in \{1,...,N\}$:

$$\frac{\varepsilon^2}{\tau} m_j (u_i^k)_j - \gamma m_j \sum_{m=1}^{N} w_{im} (u_m^k)_j + \gamma \varepsilon^2 \sum_{l \in \mathcal{J}} a_{lj} (u_i^k)_l - m_j [\lambda_i^k + \Lambda_j^k] = \frac{\varepsilon^2}{\tau} m_j (u_i^{n-1})_j, \tag{3.58}$$

$$\sum_{j \in \mathcal{J}} m_j ((u_i^k)_j - (u_N^k)_j) = \sum_{j \in \mathcal{J}} m_j (m^i - m^N) \ \text{ for } i \in \{1,...,N-1\}, \ \sum_{i=1}^{N} (u_i^k)_j = 1, \tag{3.59}$$

where $\lambda_N^k = -\lambda_1^k - ... - \lambda_{N-1}^k$.

3. Determine $(\mu_i^k)_j$ for $j \in \mathcal{A}_i^k$ using (3.53) for all $i \in \{1,...,N\}$ as

$$(\mu_i^k)_j = \frac{\varepsilon^2}{\tau} (u_i^k)_j - \gamma \sum_{m=1}^{N} w_{im} (u_m^k)_j + \gamma \varepsilon^2 \frac{1}{m_j} \sum_{l \in \mathcal{J}} a_{lj} (u_i^k)_l - \lambda_i^k - \Lambda_j^k - \frac{\varepsilon^2}{\tau} (u_i^{n-1})_j.$$

4. Set $\mathcal{A}_i^{k+1} := \{j \in \mathcal{J} : (u_i^k)_j - \frac{(\mu_i^k)_j}{c} < 0\}$, $i \in \{1,...,N\}$.

5. If $\mathcal{A}_i^{k+1} = \mathcal{A}_i^k$ for all $i \in \{1,...,N\}$ stop, otherwise set $k = k+1$ and goto 1.

Remark 3.3.1. *(i) In each node p_j for $j \in \mathcal{J}$ some components of $\boldsymbol{u}_h$ are active and the others are inactive. The number of components which are active can vary from point to point. Only for each individual component u_i can we split the set of nodes into nodes which are active and inactive for this component. This results in a quite complex linear system, see Chapter 4.*
(ii) We solve (3.58), (3.59) in two space dimensions using the direct solver UMFPACK [41] and in three space dimensions we use MINRES, see Chapter 4 for more details on the solver.
(iii) Note that if $j \in \mathcal{A}_1^k \cap ... \cap \mathcal{A}_{i-1}^k \cap \mathcal{A}_{i+1}^k \cap ... \cap \mathcal{A}_N^k$ we can use the fact that $\sum_{i=1}^{N} (u_i^k)_j = 1$ and set $(u_i^k)_j = 1$ without solving (3.58).

3.4 Convergence as a semi-smooth Newton method

In order to show that the PDAS method converges, we reformulate the method as a semi-smooth Newton method. Instead of introducing active and inactive sets we can reformulate (2.26)-(2.28) using the following semi-smooth function

$$\mathcal{H}_i(u_i, \mu_i) := \mu_i - \max(0, cu_i - \mu_i) \tag{3.60}$$

for $i \in \{1,...,N\}$ and $c > 0$.

Hence the PDAS algorithm is equivalent to a semi-smooth Newton algorithm applied to (3.5) - (3.6) and (3.60), see e.g. [72].
Setting $\mathcal{A}_h^i := \{j \in \mathcal{J} : (u_i)_j - \frac{(\mu_i)_j}{c} > 0\}$, $\mathcal{I}_h^i := \mathcal{J} \setminus \mathcal{A}_h^i$ for $i \in \{1, ..., N\}$ and using the the same principles as in the scalar case, one derives for the function $\mathcal{H}_i((u_i)_j, (\mu_i)_j)$ the slanting function $\mathcal{G}_i((u_i)_j, (\mu_i)_j) = (-c, 0)$ for $j \in \mathcal{A}_h^i$ and $\mathcal{G}_i((u_i)_j, (\mu_i)_j) = (0, 1)$ for $j \in \mathcal{I}_h^i$. We now consider the system (3.53) - (3.55) and $\mathcal{H}_i((u_i)_j, (\mu_i)_j) = 0$ as a problem of finding a root of $\boldsymbol{F}(\underline{\boldsymbol{u}}, \underline{\boldsymbol{\mu}}, \boldsymbol{\lambda}, \underline{\Lambda}) = \boldsymbol{0}$, by using a semi-smooth Newton method (SSN) $(\underline{\boldsymbol{u}}^{k+1}, \underline{\boldsymbol{\mu}}^{k+1}, \boldsymbol{\lambda}^{k+1}, \underline{\Lambda}^{k+1}) = (\underline{\boldsymbol{u}}^k, \underline{\boldsymbol{\mu}}^k, \boldsymbol{\lambda}^k, \underline{\Lambda}^k) - \boldsymbol{G}(\underline{\boldsymbol{u}}^k, \underline{\boldsymbol{\mu}}^k, \boldsymbol{\lambda}^k, \underline{\Lambda}^k)^{-1} \boldsymbol{F}(\underline{\boldsymbol{u}}^k, \underline{\boldsymbol{\mu}}^k, \boldsymbol{\lambda}^k, \underline{\Lambda}^k)$, recalling that $\underline{\boldsymbol{u}} := (\underline{u}_1, ..., \underline{u}_N)$, $\underline{\boldsymbol{\mu}} := (\underline{\mu}_1, ..., \underline{\mu}_N)$ and $\underline{u}_i$, $\underline{\mu}_i$ are the coefficient vectors of $(u_i)_h$, $(\mu_i)_h$.
In order to show local convergence of the semi-smooth Newton method we need to show invertibility of $\boldsymbol{G}$ in some neighbourhood of a solution to $\boldsymbol{F}(\underline{\boldsymbol{u}}, \underline{\boldsymbol{\mu}}, \boldsymbol{\lambda}, \underline{\Lambda}) = \boldsymbol{0}$.
In order to show the invertibility of $\boldsymbol{G}(\underline{\boldsymbol{u}}, \underline{\boldsymbol{\mu}}, \boldsymbol{\lambda}, \underline{\Lambda})$ we need a discrete Poincaré inequality: There exists a Poincaré constant $c_h^p > 0$ such that

$$(\boldsymbol{v}, \boldsymbol{v})_h \leq c_h^p (\nabla \boldsymbol{v}, \nabla \boldsymbol{v}) \quad \forall\, \boldsymbol{v} \in \boldsymbol{K} \tag{3.61}$$

with $\boldsymbol{K} := \{\boldsymbol{v} \in \boldsymbol{S}_h \mid \int_\Omega \boldsymbol{v} = \boldsymbol{0}, \sum (v_i)_j = 0 \ \forall j \in \mathcal{J}, \, v_i(p_j) = 0 \text{ if } j \in \mathcal{A}_h^i \text{ and } i \in \{1, ..., N\}\}$. The Poincaré inequality holds in a more general space than $\boldsymbol{K}$; in fact only $\int_\Omega \boldsymbol{v} = \boldsymbol{0}$ is needed. However, as discussed in Remark 2.5.4 the Poincaré constant in (3.61) can be estimated by the width of the interface rather than the width of Ω.
To show invertibility we need in addition a discrete analogue of the graph theoretic argument used in the proof of Theorem 3.2.3. Assume that active and inactive sets are given. We then choose a graph $\mathcal{E}_h$ with vertices $\{1, ..., N\}$ and edges $\{(i, l) : \exists j \in \mathcal{J}$ s.t. i and l are inactive at $j\}$.

Theorem 3.4.1. *Assume that the graph $\mathcal{E}_h$ is connected and that*

$$\tau(\sigma_{max}(\mathbf{A}) - \tfrac{\varepsilon^2}{c_h^p}) < \tfrac{\varepsilon^2}{\gamma} \tag{3.62}$$

where c_h^p is a Poincaré constant. Then the linear mapping $\boldsymbol{G}(\underline{\boldsymbol{u}}, \underline{\boldsymbol{\mu}}, \boldsymbol{\lambda}, \underline{\Lambda})$ is invertible which is equivalent to the unique solvability of (3.58), (3.59).

Proof: We show that the kernel of $\boldsymbol{G}(\underline{\boldsymbol{u}}, \underline{\boldsymbol{\mu}}, \boldsymbol{\lambda}, \underline{\Lambda})$ contains only $\boldsymbol{0}$. The equation

$$\boldsymbol{G}(\underline{\boldsymbol{u}}, \underline{\boldsymbol{\mu}}, \boldsymbol{\lambda}, \underline{\Lambda})(\underline{\boldsymbol{v}}, \underline{\boldsymbol{\kappa}}, \boldsymbol{\alpha}, \underline{\beta})^t = \boldsymbol{0} \tag{3.63}$$

is equivalent to

$$\tfrac{\varepsilon^2}{\tau} m_j (v_i)_j - \gamma m_j \sum_{m=1}^{N} w_{im} (v_m)_j + \gamma \varepsilon^2 \sum_{l \in \mathcal{J}} a_{lj} (v_i)_l - m_j (\kappa_i)_j - m_j [\alpha_i + \beta_j] = 0, \tag{3.64}$$

$$\mathcal{G}_i((u_i)_j, (\mu_i)_j) \cdot ((v_i)_j, (\kappa_i)_j) = 0 \text{ with } \mathcal{G}_i((u_i)_j, (\mu_i)_j) := \begin{cases} (-c, 0) & \text{for } j \in \mathcal{A}_h^i, \\ (0, 1) & \text{for } j \in \mathcal{I}_h^i, \end{cases} \tag{3.65}$$

$$\sum_{j \in \mathcal{J}} m_j ((v_i)_j - (v_N)_j) = 0, \qquad \sum_{i=1}^{N} (v_i)_j = 0, \qquad \sum_{i=1}^{N} \alpha_i = 0 \tag{3.66}$$

for $i \in \{1, ..., N\}$ and $j \in \mathcal{J}$. Note that $\alpha_N = -\alpha_1 - ... - \alpha_{N-1}$.
Equation (3.65) implies $\underline{v}_i \equiv \underline{0}$ on the active set $\mathcal{A}_h^i$ and $\underline{\kappa}_i = \underline{0}$ on $\mathcal{I}_h^i$ for all $i \in \{1, ..., N\}$.
To show that $\underline{\boldsymbol{v}}$, the coefficient vector of $\boldsymbol{v} \in \boldsymbol{S}_h$, equals $\underline{\mathbf{0}}$ we prove that $\boldsymbol{v} = \mathbf{0}$ is the unique solution of the quadratic optimisation problem in $\boldsymbol{v}$ on the inactive set $\mathcal{I}_1 \times \mathcal{I}_2 \times ... \times \mathcal{I}_N$

$$\min_{\boldsymbol{v} \in \boldsymbol{K}} \left[\tfrac{\varepsilon^2}{2\tau} (\boldsymbol{v}, \boldsymbol{v})_h - \tfrac{\gamma}{2} (W\boldsymbol{v}, \boldsymbol{v})_h + \tfrac{\gamma\varepsilon^2}{2} (\nabla \boldsymbol{v}, \nabla \boldsymbol{v}) \right] \tag{3.67}$$

where the first order necessary conditions are given by (3.63).
We show that (3.67) is a strictly convex minimisation problem. If $\tau \leq \frac{\varepsilon^2}{\gamma \sigma_{max}(W)}$ this follows immediately. In the other case we need to control $(\boldsymbol{v}, \boldsymbol{v})_h$ on $\boldsymbol{K}$. Using the Poincaré inequality (3.61) we obtain

$$\tfrac{\gamma\varepsilon^2}{2} (\nabla \boldsymbol{v}, \nabla \boldsymbol{v}) + \tfrac{1}{2} (\tfrac{\varepsilon^2}{\tau} - \gamma \sigma_{max}(W)) (\boldsymbol{v}, \boldsymbol{v})_h \geq (\tfrac{\gamma\varepsilon^2}{2} + \tfrac{1}{2} c_h^p (\tfrac{\varepsilon^2}{\tau} - \gamma \sigma_{max}(W)) (\nabla \boldsymbol{v}, \nabla \boldsymbol{v}) \,.$$

Hence, it follows that (3.67) is uniquely solvable if (3.62) holds, and thus $\underline{\boldsymbol{v}} \equiv \underline{\mathbf{0}}$.
Now we show that $\boldsymbol{\alpha} = \mathbf{0}$. Assume $j \in \mathcal{I}_h^i \cap \mathcal{I}_h^l$. Using that $\underline{\boldsymbol{v}} \equiv \underline{\mathbf{0}}$ in (3.64) and $(\kappa_l)_j = (\kappa_i)_j = 0$ we obtain that

$$\begin{aligned} m_j \alpha_i + m_j \beta_j &= 0, \\ m_j \alpha_l + m_j \beta_j &= 0. \end{aligned}$$

and hence $\alpha_i = \alpha_l$ for $i, l \in \{1, ..., N-1\}$.
Using the assumption that the graph $\mathcal{E}_h$ is connected we obtain together with $\alpha_N = -\alpha_1 - ... - \alpha_{N-1}$ that $\alpha_i = \alpha_l$ for all $i, l \in \{1, ..., N\}$.
In order to show that $\underline{\beta} = \underline{0}$ note that for any $j \in \mathcal{J}$ there exists an $i \in \{1, ..., N\}$ such that $j \in \mathcal{I}_h^i$. Using (3.64) and $(\kappa_i)_j = 0$ it follows that $\beta_j = 0$ and since j was

chosen arbitrarily $\underline{\beta} = \underline{0}$ which also gives that $\underline{\boldsymbol{\kappa}} = \underline{\mathbf{0}}$.

□

Theorem 3.4.2. *Assume $(\boldsymbol{u}_h, \boldsymbol{\mu}_h, \boldsymbol{\lambda}_h, \Lambda_h)$ is a solution of the discrete Allen-Cahn problem (3.53) - (3.57). Assume that the inactive sets $\hat{\mathcal{I}}_h^i = \{j \in \mathcal{J} : (u_i)_h(p_j) > 0\}$ are connected and assume that $\tau < \frac{\varepsilon^2}{\gamma \sigma_{max}(W)}$. Then (PDAS-I) converges locally in a neighbourhood of $(\boldsymbol{u}_h, \boldsymbol{\mu}_h, \boldsymbol{\lambda}_h, \Lambda_h)$.*

Proof: We choose a neighbourhood of $(\boldsymbol{u}_h, \boldsymbol{\mu}_h, \boldsymbol{\lambda}_h, \Lambda_h)$ such that the corresponding inactive sets are all connected. This is possible if we guarantee that all $j \in \hat{\mathcal{I}}_h^i$ remain active in the neighbourhood. Now Theorem 3.4.1 guarantees invertibility of $\boldsymbol{G}$ in this neighbourhood. Since only finitely many constellations with active sets are possible we can deduce that $\boldsymbol{G}^{-1}$ is uniformly bounded in this neighbourhood. Hence Theorem 1.1 in [72] now gives the local convergence result. □

Remark 3.4.3. *i) Taking into account Theorem 3.2.3 we can fulfil the assumption of Theorem 3.4.1 if h is sufficiently small. In practice we only need to ensure that there are enough mesh points on the interface.*
ii) Of course the condition on the time-step in Theorem 3.4.2 can be relaxed taking Theorem 3.4.1 into account. As the Poincaré constants of all possible active sets in the neighbourhood would enter into a precise assumption, we did not state such a result in a precise way.

3.5 Numerical tests and discussion

In this section we discuss some computational results. In Subsection 3.5.1 we consider problems where the explicit solution is known. We compare our numerical solutions to the exact sharp interface solutions and we discuss some properties of our method. In particular we show that the number of Newton iterations is mesh independent and it does not depend on the number of phases N.
In Subsection 3.5.2 we present some numerical simulations in two and three space dimensions including grain growth and soap bubble configurations.
For the implementation we used again the finite element toolbox ALBERTA 2.0 (see Schmidt and Siebert [108]) for adaptivity and we use the same refinement strategy as for the scalar case. Elements are marked for refinement if $0 < (u_h^{n-1})_i < 1$ for $i = \{1, ..., N\}$.
For the computations in two space dimensions we take the minimal diameter of all elements $h_{min} = \frac{1}{256}$ and the maximal diameter $h_{max} = \frac{1}{16}$, unless otherwise stated. Furthermore, we set the interfacial parameters $\varepsilon = \frac{1}{16\pi}$, $\gamma = 1$ and we choose the domain $\Omega = (-1, 1)^2$ (with the exception of the corner bubbles computations where

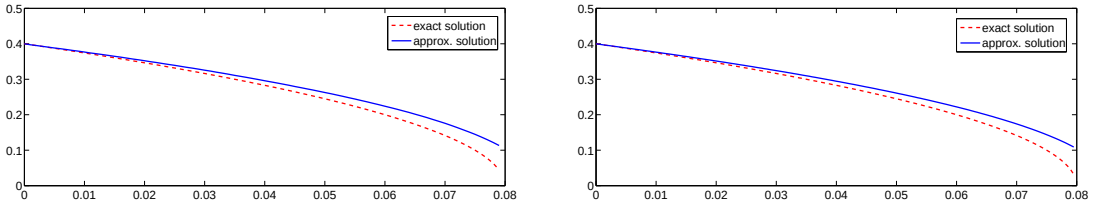

Figure 3.1: Exact and approximate radii for time-step $\tau = 2 \cdot 10^{-3}$ (left) and $\tau = 1 \cdot 10^{-4}$ (right).

Ω is triangular). For the time-step we take $\tau = 1 \cdot 10^{-4}$ unless otherwise stated. For computations in three space dimensions we take $\Omega = (-1, 1)^3$, $\varepsilon = \frac{1}{12\pi}$, $\gamma = 1$, $h_{min} = \frac{1}{128}$, and $h_{max} = \frac{1}{8}$. This is necessary due to memory restrictions. The matrix W in the multi-obstacle potential term is set to be the identity matrix.

3.5.1 Comparison with analytically known solutions

Local vector-valued Allen-Cahn

In this subsection we compare the numerical approximations obtained by using the PDAS-method to exact sharp interface solutions. We consider circles for which the radius $R(t)$ at time t is given by the ODE $\frac{d}{dt}R(t) = -\frac{1}{R(t)}, R(0) = 0.4$ [25].
We set $N = 3$, i.e. three phases are present, and take the simple problem of two shrinking circles with initial radii $R(0) = 0.4$ and centres $(-0.5, 0)$ and $(0.5, 0)$. Two order parameters $(u_h)_1$ and $(u_h)_2$ are each set to be 1 on one circle and 0 anywhere else. The third order parameter $(u_3)_h$ is 1 outside the circles and 0 inside. We take smooth transition layers of width $\varepsilon\pi$. Both circles shrink with the same velocity $-\frac{1}{R(t)}$. We calculate the radius of the approximate solution in each time-step by taking the intersection of the 0.5-level set of $(u_1)_h$ and $(u_2)_h$ and the x_1-axis. Figure 3.1 shows a plot of the exact and approximate radius for two timestep sizes $\tau = 2 \cdot 10^{-3}$ and $\tau = 1 \cdot 10^{-4}$. The two circles shrink with exactly the same velocity and hence we only present the radius of one of the circles. Between $t = 0$ and $t = 0.03$ the approximation is very accurate, it only deteriorates when the radius of the circle is less than 0.2 and a singularity (i.e. high curvature when the circle is about to disappear) is approached. There is hardly any difference between the two time-steps, so we can choose the larger time-step which is more efficient. Even larger time-steps can be chosen, but the approximations deteriorate especially when the curvature, and hence the velocity of the interface, is higher. For a noticeable improvement of the approximation we need to take a finer mesh size on the interface. If we half the minimal diameter the approximation remains accurate even when the circle becomes very small.
As before we cannot show analytically that the number of PDAS iterations is mesh

independent. However, in our application a good initial data on the current time-step is given from the solution of the previous time-step. Therefore, mesh independence is only of interest if both element size h and also time-step τ are driven to 0. We use a uniform mesh with element size h and the same initial data as previously stated. Table 3.1 shows that when h and τ both are decreased simultaneously, the number of PDAS iterations remains stable.

τ	h	DOFs	PDAS-iter.
$1 \cdot 10^{-3}$	1/128	66049	4.77
$2.5 \cdot 10^{-4}$	1/256	263169	4.86
$6.25 \cdot 10^{-5}$	1/512	1050625	4.70
$1.5625 \cdot 10^{-5}$	1/1024	319230 [1]	4.57

Table 3.1: Average number of PDAS iterations up to $t = 0.03$ for varying mesh and time-step sizes.

In the next computation we examine the number of PDAS-iterations for increasing phases N. We take circles of radii 0.3 and position them such that they do not intersect. For 3 order parameters we take two circles (one phase for each circle and one phase outside the circles); for $N = 4$ we take three circles, and so on up to $N = 7$ where six circles are needed. Moreover, we consider $N = 2$ (one circle) for the vector-valued Allen-Cahn equation with two order parameters and the scalar Allen-Cahn equation. In this case the scalar equation is obtained by taking $u_2 = 1 - u_1$. Figure 3.2 shows the average number of PDAS-iterations for t between 0 and 0.04 with fixed timestep size $\tau = 1 \cdot 10^{-4}$. For $N = 1$ and $N = 2$ the number of PDAS-iterations is considerably lower than for larger N. This could be because both order parameters are inactive on the interface. For larger N we have that two order parameters are inactive on each of the interfaces whilst the other order parameters are active (i.e. they are zero). For $N \geq 3$ the average number of PDAS-iterations remains almost stable. We conclude that the number of PDAS-iterations is driven by the change of the active and inactive sets only, while the number of phases does not seem to make much difference.

The computations thus far did not contain any triple points. In the next computation we consider a three phase system and we calculate the evolution of a triple junction. As initial configuration we choose a T-shaped triple junction. This configuration violates the 120° angle condition also known as Young's law [119]. In Figure 3.3 we show the evolution of the T-shape. Very quickly the 120° angle condition is attained and the shape of the interfaces starts to change, approaching a constantly transported profile. Finally the horizontal interface disappears and two of the phases shrink to the corners of the domain and will disappear.

[1] Due to memory restrictions an adaptive mesh was used with $h_{min} = h$

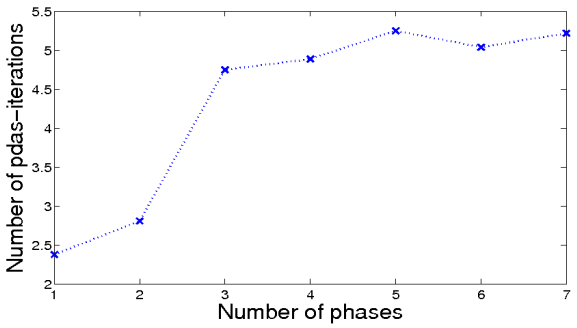

Figure 3.2: Average number of PDAS-iterations for increasing number of phases N

For the sharp interface problem, the constantly transported profile can be constructed explicitely, see [59]. Figure 3.4 shows the calculated transport velocities of the interface for different values on the y-axis and we see that they converge to the velocity of the explicit solution of the sharp interface problem. Note that we consider the domain $\Omega = (-1, 1)^2$ and hence the triple point is at $y = 0$. A comparison of the sharp interface profile and the numerical solution at $t = 0.5$ is shown in Figure 3.5.

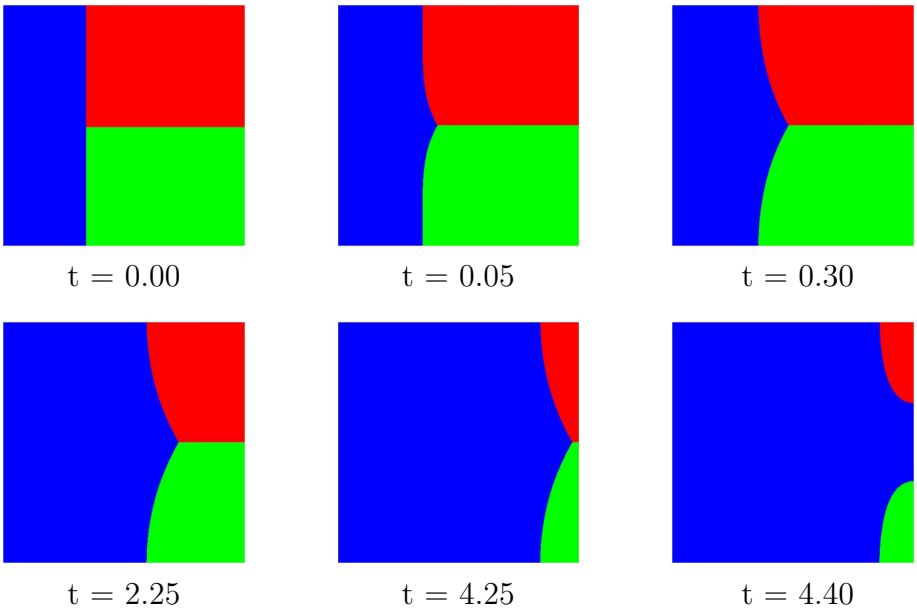

Figure 3.3: Evolution of a T-shaped structure using the vector-valued Allen-Cahn variational inequality.

Non-local vector-valued Allen-Cahn

Now we shall consider the vector-valued Allen-Cahn variational inequality with volume constraints. In the following we compare the approximation obtained using the PDAS-method to the exact solution. Therefore, we need a setting where the exact solution can be calculated analytically. For the scalar non-local Allen-Cahn

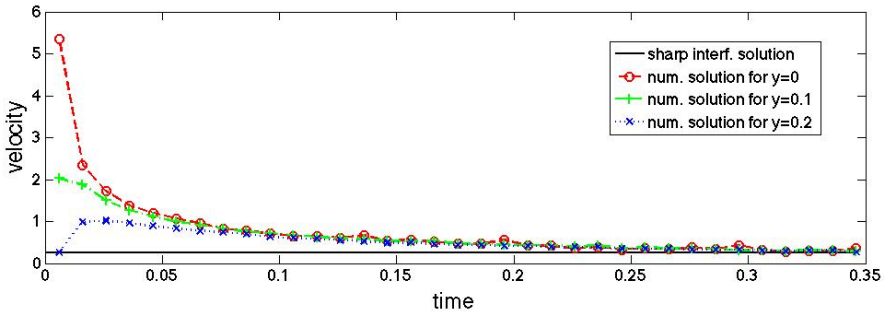

Figure 3.4: Transport velocities of the diffuse interface for different values on the y-axis compared to the velocity of the constantly transported solution of the sharp interface problem.

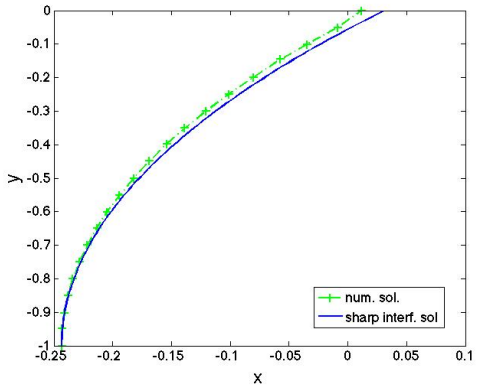

Figure 3.5: Comparison of the simulated interface profile (lower branch in Figure 3.3) with the constantly transported sharp interface solution.

variational inequality we found explicit solutions for the model problem where one phase occupies two circles of radii r_1 and r_2. We can use this problem in the case of $N = 3$ by considering two decoupled systems, that is four circles that do not intersect where phase 1 occupies two circles, phase 2 occupies the other two circles and phase 3 is present outside these four circles, see Figure 3.6. For the first order parameter (blue) we take the initial radii of the two circles to be $r_1(0) = 0.2$ and $r_2(0) = 0.3$ and for the second order parameter (red) we take $r_3(0) = 0.4$ and $r_2(0) = 0.25$. The exact sharp interface solution to this problem is given by the following system of ODEs: $r_i' = -\frac{1}{r_i} + \frac{2}{r_1+r_2}$ for $i = 1, 2$ and $r_i' = -\frac{1}{r_i} + \frac{2}{r_3+r_4}$ for $i = 3, 4$. Figure 3.7 shows the approximate solution and the exact solution for the two big circles for two different time-steps $\tau = 1 \cdot 10^{-3}$ and $\tau = 1 \cdot 10^{-4}$. The behaviour of the two small circles is essentially the same and therefore omitted. For both time-steps the approximations are very good, even better than the ones without volume conservation. This is to be expected since the volume constraints slow down the speed at which the interfaces move. Larger time-steps can also be taken as long as the curvature does not become too big.

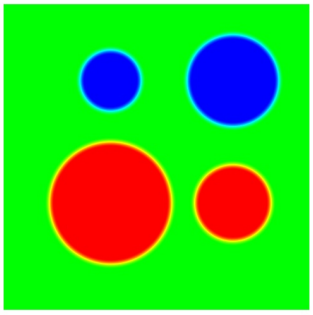

Figure 3.6: Initial configuration for vector-valued Allen-Cahn ($N = 3$) with volume constraints for comparison with explicitely known solutions.

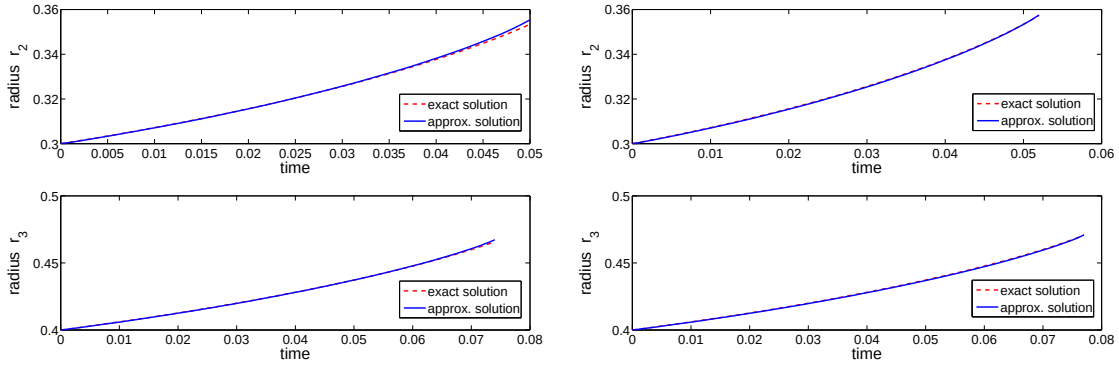

Figure 3.7: Exact and approximate radii for time-step $\tau = 2 \cdot 10^{-3}$ (left) and $\tau = 1 \cdot 10^{-4}$ (right).

3.5.2 Numerical simulations

Evolution of cellular structures

The vector-valued Allen-Cahn equation without volume constraints can be used to simulate the evolution of cellular structures in foams. Cellular structures occur naturally for example in biological tissue or polycrystalline metals, but also beer froth or washing up foam. In the early 1950's John von Neumann proved that in two dimensional foams, grains with more than six neighbours grow, those with less than six neighbours shrink and those with exactly six neighbours neither grow nor shrink, although they can change their shape. In particular, von Neumann proved the following law for the change of the area A of one bubble

$$\frac{dA}{dt} = -2\pi M\alpha \left(1 - \frac{n}{6}\right)$$

where M and α are constants describing mobility and surface tension of the bubble, and n is the number of its neighbours [115].

For the computation in Figure 3.8 we use a Voronoi partitioning algorithm [6] to randomly fill the two dimensional computational domain. We use 30 order parameters for this computation. At the beginning of the computation cell edges are not smooth and angle conditions are not fulfilled, but already at time $t = 0.004$ the partitioning can be viewed as a foam. For inner cells we observe that they behave according to von Neumann's law, see Figure 3.8. This computation could also describe grain growth evolution. Each of the 30 phases describes a different orientational variant in a crystalline material. Of course, when computing grain growth it is more appropriate to have less phases and more grains with the same orientation.

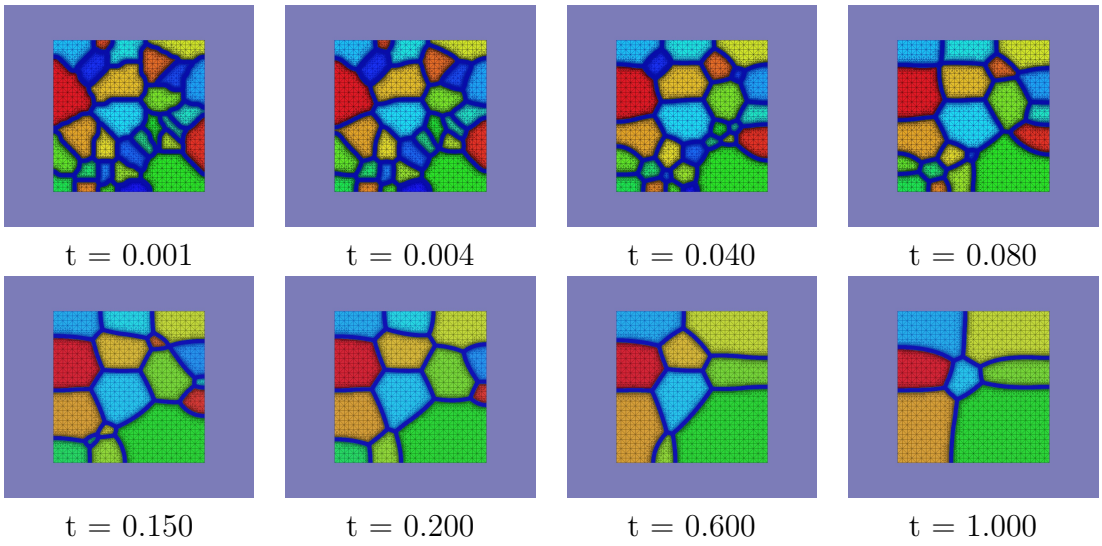

Figure 3.8: Vector-valued Allen-Cahn equation with Voronoi partitioning as initial data (30 order parameters).

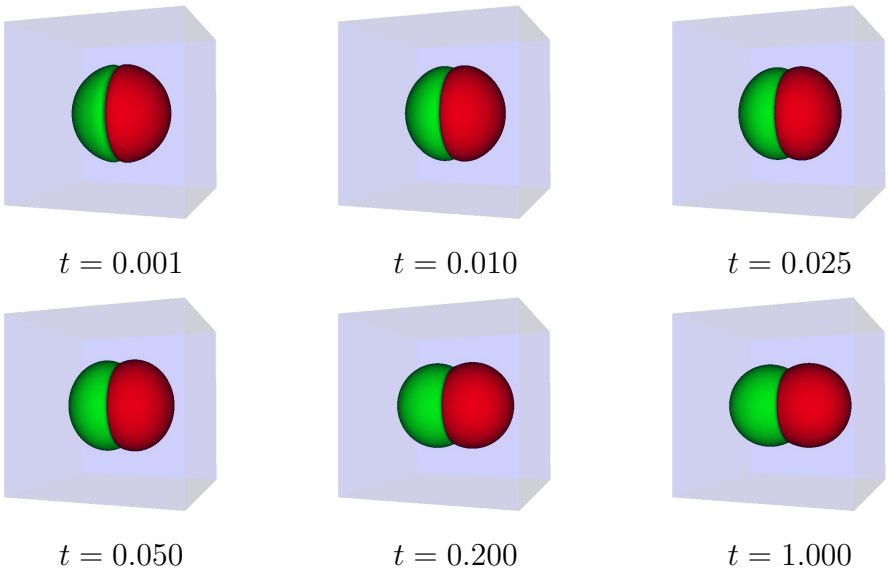

Figure 3.9: Double bubble; vector-valued Allen-Cahn with volume constraints, 3 order parameters.

Soap bubble configurations

In nature, soap bubble configurations enclose and separate several regions of space. They have fixed volumes and tend to minimise the total surface area. This observation leads to the following basic problem: How can one enclose and separate n regions of $\mathbb{R}^3$ having volumes $v_1, v_2, ..., v_n$ with the smallest possible surface area. For $n = 1$, i.e. a single region it is well known that a sphere is the optimal configuration. It has been shown that for two regions the optimal configuration is a double bubble [75].

We can use the vector-valued non-local Allen-Cahn equation to model soap bubble configurations. Due to the volume constraints the regions to be separated have fixed volume whilst the curvature driven motion tends to minimise the surface energy, and hence the surface area. In the first computation we use three order parameters and start with a sphere where the left half is occupied by phase 1 and the right half is occupied by phase 2. We note that first very rapidly the 120° angle condition is attained. Then the two halves gradually move outwards whilst staying attached in the middle, see Figure 3.9. The movement ends when the steady state, a double bubble, is reached.

Figure 3.10 shows a similar computation for $N = 4$. We begin the computations with a sphere that is divided into three equal spherical wedges. Each of these wedges is represented by a different phase, i.e. we have three phases in the sphere and one phase outside. As before, first the angle condition is attained and then the three parts move until a triple bubble is reached.

We conclude our soup bubble configurations by numerically investigating the results

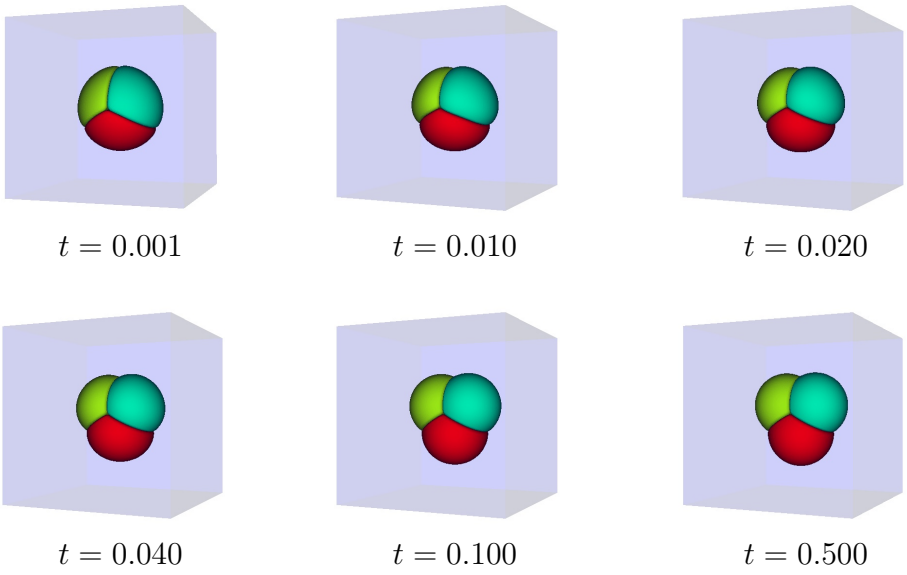

Figure 3.10: Triple bubble; vector-valued Allen-Cahn with volume constraints, 4 order parameters.

of Hruska et al. in [74]. This work examines enclosures of two connected regions in a sector of the Euclidean plane bounded by two rays emanating from a common point. The authors showed that for given $a_1, a_2 > 0$ and a corner of angle θ the shortest way to enclose and separate connected regions with areas a_1 and a_2 with a connected exterior region is either

1. two concentric circles inside the corner with the smaller area closer to the corner (see Fig. 3.11 left), or

2. a "truncated standard double bubble" inside the corner, consisting of three circular arcs meeting at a single vertex at angles of 120° and meeting the wall at right angle in three distinct points (see Fig. 3.11 right).

Furthermore, Hruska et al. show that if

$$\theta \geq \theta_0 = \frac{a_1 \pi}{(\sqrt{a_1} + \sqrt{a_1 + a_2} - \sqrt{a_2})^2},$$

then the truncated standard double bubble has shorter perimeter. Note that θ_0 has a minimum of $\pi/2$ when $a_1 = a_2$. There exists also an angle θ_1 for which the concentric circle configuration has the shorter perimeter for all $\theta < \theta_1$. However, θ_1 is not known. It is not known either what happens for $\theta_1 < \theta < \theta_0$ and whether there is a unique angle at which the two configurations have equal perimeter.
We use the vector-valued Allen-Cahn equation with volume-conservation to examine these theoretical results numerically. Note that both configurations, i.e. the concentric circles inside the corner (type 1) and the truncated standard double bubble

Figure 3.11: Minimising configurations for two bubbles in a corner: two concentric circles (left) and truncated standard double bubble (right).

Figure 3.12: Two computations for $\theta = 45°$ and equal areas in the corner leading to both minimising configurations.

(type 2) are local minima. Starting with either of these configurations as initial data will lead to a stationary system. Therefore, it is not suitable to start with one particular shape of the two regions in the corner, since the system will converge to the local minima which is 'closer' to this initial shape. Hence, we take random initial data in the corner. We fix a triangular domain Ω with one of the angles being θ. Away from the corner with angle θ the order parameter corresponding to the exterior phase is set to be 1.0. Close to the corner (in 20 % of the domain Ω) we set at each mesh point one of the two other order parameters to be 0.99 or 0.01. We cannot take values 1.0 and 0.0 since the primal-dual active set methods needs non-empty inactive sets. We vary the ratio of the areas a_1 and a_2 of the regions in the corner and the angle θ. Table 3.2 shows which of the two configurations we obtained. For each angle and area ratio we did three computations in order to make sure that we are getting the same result independent of the initial data. In two cases we obtained both configurations during the 3 trials. For these cases we computed 10 trials in total and also looked at the interfacial energy. The interfacial energy was lower for whatever configuration appeared more often during the 10 trials. Figure 3.12 shows an example where both configurations occurred.

For angles greater than 90° we obtained the truncated double bubble for all computations. For decreasing angles the concentric circle configuration starts to appear; at first only when the two areas are the same, but for very small angles (about 10°) this configuration appears throughout, see also Figure 3.13. In all computations one of the two configurations was obtained as a steady state.

angles	volume ratios		
	50:50	30:70	15:85
135°	type 2	type 2	type 2
90°	type 2	type 2	type 2
45°	type 2 [2]	type 2	type 2
30°	type 1 [3]	type 1	type 2
20°	type 1	type 1	type 2
10°	type 1	type 1	type 1

Table 3.2: Computations for various angles and volume ratios

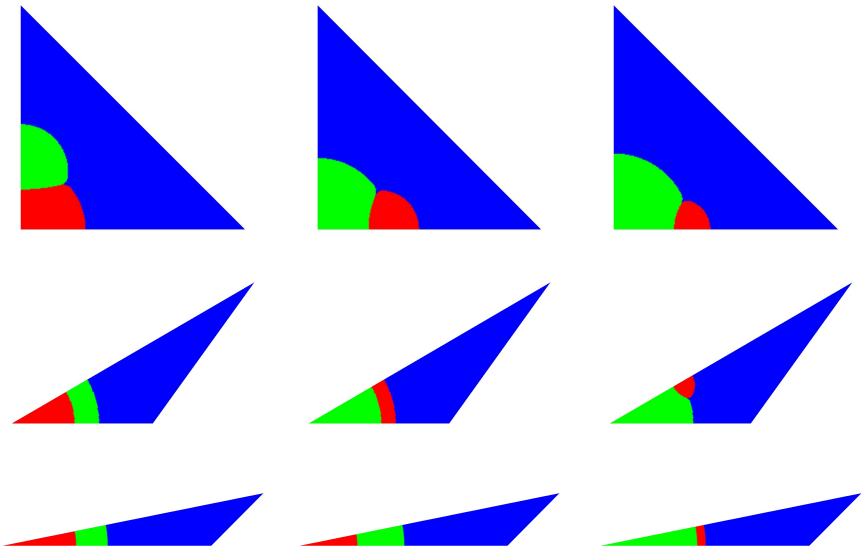

Figure 3.13: Minimising configurations obtained for $\theta = 90°, 30°, 10°$ and area ratios 50:50, 30:70, 15:85.

For the concentric circle configuration (type 1) the smaller area should be in the corner. However, in most of our computation (10 out of 12) we end up with the larger area in the corner. This is not due to numerical discretisation errors but is more a problem of mean curvature flow itself, see Figure 3.14. Both concentric circle configurations are local minima, yet the interfacial energy is lower when the smaller area is in the corner - which coincides with the theoretical results.
For the truncated double bubble configuration it is conjectured that the larger region is nestled in the corner [74], but it has not been proved yet. In all our computations

$t = 0.000$ $t = 0.001$ $t = 0.017$ $t = 0.033$

Figure 3.14: Formation of the concentric circle configuration

[2] In 7 out of 10 trials we obtained type 2
[3] In 8 out of 10 trials we obtained type 1

$t = 0.002$ $t = 0.010$ $t = 0.021$ $t = 0.056$

Figure 3.15: Three bubbles in the corner for $\theta = 10°$

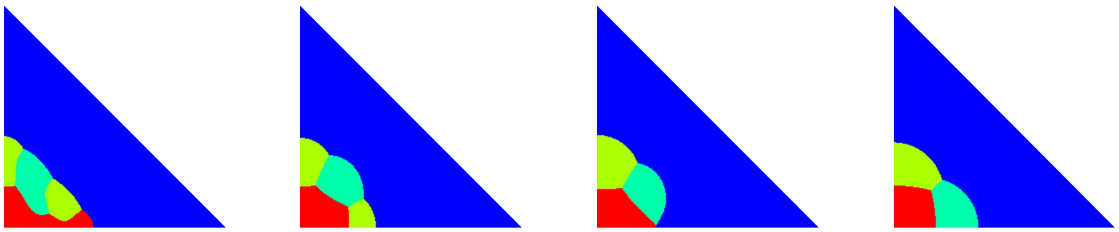

$t = 0.002$ $t = 0.025$ $t = 0.060$ $t = 0.400$

Figure 3.16: Three bubbles in the corner for $\theta = 90°$

we obtained that the larger region is nestled in the corner.

Thus far only the simple case of two bubbles in the corner has been formally analysed. Since our computations proved accurate for two bubbles in the corner (with the exception of the area distribution for the concentric circles) we also computed three bubbles in the corner. We would expect the configurations to be similar to the ones for the two bubbles, i.e. three concentric circles when the angle θ is small or some sort of triple bubble for θ large.

We considered two settings. In the first setting we took $\theta = 10°$ and the areas of the three bubbles were set to be equal. As expected we observe that the computed minimising configuration consists of three concentric circles, see Figure 3.15. In the second setting we changed θ to be $90°$ (the areas of the three bubbles are the same). The computations give now a triple bubble configuration consisting of five circular arcs meeting at two points at angles of $120°$, see Figure 3.16. For each of the two settings we ran 3 computations all of which lead to the same steady state.

Chapter 4

Strategies for solving the linear systems

With the primal-dual active set strategy, which we introduced in Section 2.4.2, we only need to solve a linear system on the inactive set. This makes the method very flexible in the sense that various linear algebra solvers can be used. In fact, solving the linear systems is generally one of the most expensive parts of the computation. Especially for large time-steps it can take up more than 50% of the computation time, see Tables 2.1 and 2.2. Hence, the choice of an appropriate solver speeds up the method and makes it even more competitive.
In this chapter we have a closer look at the linear systems. We consider various solvers, their advantages and disadvantages and we propose a preconditioning strategy. The scalar and the vector-valued cases are dealt with separately mainly to avoid confusions. The strategies, however, are very similar.

4.1 Non-local Allen-Cahn variational inequality

We consider the scalar non-local Allen-Cahn problem first, see Chapter 2. Recall that after introducing active and inactive sets we can rewrite the equations (2.33) and (2.34) as follows

$$\begin{bmatrix} L_{\mathcal{I},\mathcal{I}} & L_{\mathcal{I},\mathcal{A}^+} & L_{\mathcal{I},\mathcal{A}^-} & M_{\mathcal{I},\mathcal{I}} & 0 & 0 & -\underline{m}_{\mathcal{I}} \\ L_{\mathcal{A}^+,\mathcal{I}} & L_{\mathcal{A}^+,\mathcal{A}^+} & L_{\mathcal{A}^+,\mathcal{A}^-} & 0 & M_{\mathcal{A}^+,\mathcal{A}^+} & 0 & -\underline{m}_{\mathcal{A}^+} \\ L_{\mathcal{A}^-,\mathcal{I}} & L_{\mathcal{A}^-,\mathcal{A}^+} & L_{\mathcal{A}^-,\mathcal{A}^-} & 0 & 0 & M_{\mathcal{A}^-,\mathcal{A}^-} & -\underline{m}_{\mathcal{A}^-} \\ 0 & 0 & 0 & I & 0 & 0 & 0 \\ 0 & I & 0 & 0 & 0 & 0 & 0 \\ 0 & 0 & I & 0 & 0 & 0 & 0 \\ \underline{m}_{\mathcal{I}}^T & \underline{m}_{\mathcal{A}^+}^T & \underline{m}_{\mathcal{A}^+}^T & 0 & 0 & 0 & 0 \end{bmatrix} \begin{bmatrix} \underline{u}_{\mathcal{I}} \\ \underline{u}_{\mathcal{A}^+} \\ \underline{u}_{\mathcal{A}^-} \\ \underline{\mu}_{\mathcal{I}} \\ \underline{\mu}_{\mathcal{A}^+} \\ \underline{\mu}_{\mathcal{A}^-} \\ \lambda \end{bmatrix} = \begin{bmatrix} \underline{b}_{\mathcal{I}} \\ \underline{b}_{\mathcal{A}^+} \\ \underline{b}_{\mathcal{A}^-} \\ \underline{0}_{\mathcal{I}} \\ \underline{1}_{\mathcal{A}^+} \\ -\underline{1}_{\mathcal{A}^-} \\ m\,|\Omega| \end{bmatrix}.$$

where $L := (\frac{\varepsilon^2}{\tau} - \gamma)M + \varepsilon^2\gamma A$ and $\underline{b} = \frac{\varepsilon^2}{\tau} M\underline{u}^{(n-1)}$. Given that $\underline{u}_{\mathcal{A}^+} = 1, \underline{u}_{\mathcal{A}^-} = -1$ and $\underline{\mu}_{\mathcal{I}} = 0$, this linear system can be reduced to the following form

$$\begin{bmatrix} L_{\mathcal{I},\mathcal{I}} & -\underline{m}_{\mathcal{I}} \\ -\underline{m}_{\mathcal{I}}^T & 0 \end{bmatrix} \begin{bmatrix} \underline{u}_{\mathcal{I}} \\ \lambda \end{bmatrix} = \begin{bmatrix} \underline{b}_{\mathcal{I}} - L_{\mathcal{I},\mathcal{A}^+}\underline{u}_{\mathcal{A}^+} - L_{\mathcal{I},\mathcal{A}^-}\underline{u}_{\mathcal{A}^-} \\ -m\,|\Omega| + \underline{m}_{\mathcal{A}^+}^T\underline{u}_{\mathcal{A}^+} + \underline{m}_{\mathcal{A}^-}^T\underline{u}_{\mathcal{A}^-} \end{bmatrix}. \tag{4.1}$$

The Lagrange multipliers $\underline{\mu}$ on $\mathcal{A}_\pm$ are then given by

$$\begin{aligned} M_{\mathcal{A}^+,\mathcal{A}^+}\underline{\mu}_{\mathcal{A}^+} &= \underline{b}_{\mathcal{A}^+} - L_{\mathcal{A}^+,\mathcal{I}}\underline{u}_{\mathcal{I}} - L_{\mathcal{A}^+,\mathcal{A}^+}\underline{u}_{\mathcal{A}^+} - L_{\mathcal{A}^+,\mathcal{A}^-}\underline{u}_{\mathcal{A}^-} + \lambda\underline{m}_{\mathcal{A}^+} \\ M_{\mathcal{A}^-,\mathcal{A}^-}\underline{\mu}_{\mathcal{A}^-} &= \underline{b}_{\mathcal{A}^-} - L_{\mathcal{A}^-,\mathcal{I}}\underline{u}_{\mathcal{I}} - L_{\mathcal{A}^-,\mathcal{A}^+}\underline{u}_{\mathcal{A}^+} - L_{\mathcal{A}^-,\mathcal{A}^-}\underline{u}_{\mathcal{A}^-} + \lambda\underline{m}_{\mathcal{A}^-}. \end{aligned} \tag{4.2}$$

For practical purposes we look at the system matrix

$$\mathcal{K} := \begin{bmatrix} L & -\underline{m} \\ -\underline{m}^T & 0 \end{bmatrix} \tag{4.3}$$

as we do not form the matrix $L_{\mathcal{I},\mathcal{I}}$ but rather use L and implicitly work only on the free variables $\underline{u}_{\mathcal{I}}$. There are mainly two strategies to achieve this. One possibility is to introduce a bijective mapping from the set of inactive nodes $\mathcal{I}$ to the set $\{1, ..., n_{\mathcal{I}}\}$ where $n_{\mathcal{I}}$ is the number of points in $\mathcal{I}$. Using this one can work with vectors of length $n_{\mathcal{I}} + 1$, and whenever information from the matrix is needed one can use this mapping. Another possibility is to work with the full matrix and ensure that all the vector entries corresponding to nodes in $\mathcal{A}^+$ and $\mathcal{A}^-$ are zero at any time. Let $\mathbf{p}$ be a vector with zeroes on the active and inactive nodes and multiply the matrix $\mathcal{K}$ by this vector, i.e.

$$\mathcal{K}\mathbf{p} = \begin{bmatrix} L_{\mathcal{I},\mathcal{I}} & L_{\mathcal{I},\mathcal{A}^+} & L_{\mathcal{I},\mathcal{A}^-} & -\underline{m}_{\mathcal{I}} \\ L_{\mathcal{A}^+,\mathcal{I}} & L_{\mathcal{A}^+,\mathcal{A}^+} & L_{\mathcal{A}^+,\mathcal{A}^-} & -\underline{m}_{\mathcal{A}^+} \\ L_{\mathcal{A}^-,\mathcal{I}} & L_{\mathcal{A}^-,\mathcal{A}^+} & L_{\mathcal{A}^-,\mathcal{A}^-} & -\underline{m}_{\mathcal{A}^-} \\ \underline{m}_{\mathcal{I}}^T & \underline{m}_{\mathcal{A}^+}^T & \underline{m}_{\mathcal{A}^+}^T & 0 \end{bmatrix} \begin{bmatrix} \underline{p}_{\mathcal{I}}^{(1)} \\ \underline{p}_{\mathcal{A}^+}^{(1)} = 0 \\ \underline{p}_{\mathcal{A}^-}^{(1)} = 0 \\ p^{(2)} \end{bmatrix}. \tag{4.4}$$

Then it can easily be seen that if we eliminate the entries of $\mathcal{K}\mathbf{p}$ corresponding to the sets $\mathcal{A}^+$ and $\mathcal{A}^-$ working with system (4.3) is a feasible approach. Which of these strategies one is using depends strongly on the software package. In general, we have been working with the first approach.

Let us now focus on solving the linear system (4.1). The matrix in this system is sparse and symmetric. We have shown in Theorem 2.5.3 that this matrix is invertible if $\tau(1-\frac{\varepsilon^2}{c_h^P}) < \frac{\varepsilon^2}{\gamma}$ holds. Under the same time-step restriction and using that the mass matrix M is positive definite and the stiffness matrix A is positive semi-definite it is also obvious that $L_{\mathcal{I},\mathcal{I}}$ and also L are positive definite. Hence, the matrix $\mathcal{K}$ is in so-called saddle point form. There are two classes of solvers for these kinds of

problems: direct solvers and iterative solvers. Direct solvers are known to perform extremely well when the dimension of the problem is not too big. Typically, direct solvers can deal with linear systems with up to 800,000 unknowns. For larger systems iterative methods have to be employed. The most common iterative solvers are the so-called Krylov subspace methods. These methods minimise a given quantity over the Krylov subspace span $\{\mathbf{r}_0, \mathcal{K}\mathbf{r}_0, ..., \mathcal{K}^{k-1}\mathbf{r}_0\}$ at the current (k-th) iteration where $\mathbf{r}_0 = \mathbf{b} - \mathcal{K}\mathbf{x}_0$. For symmetric positive definite matrices the conjugate gradient (CG) method minimises the energy norm of the errors. Other Krylov subspace methods for more general matrices include the minimal residual (MINRES) method, the general minimal residual (GMRes) method and the (stabilised) BiCG method.

For the standard Allen-Cahn equation without volume conservation we have to solve the first line of (4.1) with $\lambda = 0$. In [107] three solvers for this problem are considered. The first solver is the SOR which is used mainly to demonstrate that even when using the same solver the PDAS method is quicker than the projected SOR method. The second solver is the conjugate gradient method and the last solver tested is the direct solver UMFPACK [41]. UMFPACK is a set of routines for solving unsymmetric sparse linear systems. It was originally developed by Davis and Duff [42] in Fortran; the current version is written in C and it is easy to call the routines from Alberta. However, UMFPACK requires the whole matrix $L_{\mathcal{I},\mathcal{I}}$ which has to be set in every Newton iteration. The numerical tests in [107] showed that it depends very strongly on the problem and the parameters which of the three solvers performs best. In general, for small time-steps, iterative solvers like SOR and CG perform better, since they can take advantage of a good initial guess which is provided by the previous Newton iteration. For larger time-steps quite often UMFPACK was found to be the quickest solver. The research into sparse direct solvers is much more advanced than for iterative solvers and hence good solvers are available. One drawback of direct solvers is that they cannot deal with large problems. For computations in three space dimensions UMFPACK cannot be used. In [107] the CG method was used rather inefficiently. In order to use the ALBERTA built-in CG solver the system matrix was changed to be the "identity" matrix (i.e. the diagonal entry was set to equal 1 and all the other entries were set to 0) for active rows. For inactive rows the system matrix remained unchanged. Active nodes in the right hand side vector were treated like a Dirichlet boundary and were set to 1 and -1. The problem with this approach is that the system matrix needs to be assembled for each Newton iteration which is of course expensive.

We have found another way to use the built-in ALBERTA solvers. It turns out that one only has to modify the matrix-vector multiplication such that only $L_{\mathcal{I},\mathcal{I}}\underline{u}_{\mathcal{I}}$ is considered. The right hand side vector and the vector for the initial guess also need to be modified such that they are vectors of length $n_{\mathcal{I}}$ and then a bijective mapping

can be used to obtain the 'correct' vector $\underline{u}$. With this strategy the following solvers from the OEM library can be used: conjugate gradient (for symmetric positive definite systems), stabilised BiCG (for non-symmetric system matrices), GMRes (for regular system matrices), method of orthogonal directions (for symmetric positive system matrices), and method of orthogonal residuals (for symmetric systems). For the standard Allen-Cahn variational inequality without volume constraints we found that the conjugate gradient method performed best. For the shrinking circle problem with $\varepsilon = \frac{1}{16\pi}, \tau = 1 \cdot 10^{-3}, h_{min} = \frac{1}{16}, h_{max} = \frac{1}{256}$ and $T = 0.1$ the following computation times in seconds were obtained: 39.75 for CG, 51.38 for BiCG, 70.33 for GMRes with 0 restarts. The method of orthogonal directions cannot be used since the system matrix has negative elements and the method of orthogonal residuals does not seem to give good results for this time-step. Even if the tolerance for the norm of the residual is taken to be extremely small (10^{-20}) the system is still solved very inaccurately and leads to very poor approximations. One reason might be that the norm used is inappropriate for our sort of problem. It is to be expected that for symmetric positive matrices CG performs better than the other two Krylov subspace methods. For comparison, the UMFPACK solver needed 38.66 seconds for this computation. However, for smaller time-steps CG performs better than the direct solver UMFPACK and it also works for large problems.

Based on these experiences we suggest to use Krylov subspace solvers, especially for large problems. The conjugate gradient method should only be used for symmetric positive matrices. For indefinite matrices, such as in (4.1), we found that CG still worked extremely well, but there is a small chance that it might not work. For indefinite symmetric matrices the minimal residual method (MINRES) is the Krylov subspace solver of choice. It minimises the Euclidean norm of the residual $\underline{r}_k = \underline{b} - \mathcal{K}\underline{u}_k$. Compared to the conjugate gradient method MINRES only requires two extra vector operations in an iteration. We shall briefly investigate computation times for the various solvers. We use an ellipse with major diameter 1.4 and minor diameter 0.8 and we use the following set of parameters: $\varepsilon = \frac{1}{16\pi}, \tau = 1 \cdot 10^{-3}, h_{min} = \frac{1}{16}, h_{max} = \frac{1}{256}$ and $T = 0.02$. The following computation times in seconds were obtained for the ALBERTA solvers: 27.99 for CG, 35.67 for BiCGStab and 69.22 for GMRes without restart. Using the direct solver UMFPACK the computation time was 28.21, hence almost the same as CG. However, even though the conjugate gradients seems to work very well for this problem, one should bear in mind that it might fail. The solver MINRES needed 29.66 seconds for this computation. This solver is easy to implement and we programmed it in such a way that it only uses vectors of length $n_{\mathcal{I}} + 1$. The computation time for MINRES is pretty much the same as for CG and UMFPACK, thus MINRES should be a good choice for a robust solver which can also deal with large problems.

The convergence behaviour of iterative schemes usually depends on the conditioning of the problem and the clustering of the eigenvalues. Hence one may attempt to transform the linear system into one that is equivalent, in the sense that it gives the same solution, but has more favourable spectral properties, i.e. a smaller condition number. Such a transformation is achieved by using a preconditioner. For instance, if a matrix $\mathcal{P}$ approximates the coefficient matrix $\mathcal{K}$ in some way, the transformed system $\mathcal{P}^{-1}\mathcal{K}\mathbf{x} = \mathcal{P}^{-1}\mathbf{b}$ has the same solution as the original system $\mathcal{K}\mathbf{x} = \mathbf{b}$. For a good choice of $\mathcal{P}$ the condition number of $\mathcal{P}^{-1}\mathcal{K}$ is smaller than the one of $\mathcal{K}$ and hence the preconditioned system may be solved more efficiently.
Therefore, we will analyse the linear system (4.3) with respect to preconditioning. For the ALBERTA built-in solvers there are three preconditioning strategies available: diagonal preconditioning, hierarchical basis preconditioning and BPX (multilevel preconditioner developed by Bramble, Pasciak and Xu). However, none of these preconditioners seemed to speed up computations.
The linear equation (4.3) is in saddle point form which is known to arise in a variety of applications [14] and has been studied in detail for example in [14, 51]. A common ansatz for preconditioning a saddle point matrix of this form is given in [91]. Here the preconditioning matrix is given by

$$\mathcal{P} = \begin{bmatrix} L & \underline{0} \\ \underline{0}^T & S \end{bmatrix}$$

where S is the Schur complement $-\underline{m}^T L^{-1}\underline{m}$. The authors showed that for this choice of 'exact' preconditioner the preconditioned system $\mathcal{P}^{-1}\mathcal{K}$ has at most three distinct eigenvalues if $\mathcal{P}^{-1}\mathcal{K}$ is nonsingular.
However, we would like to avoid the approximation of S. Therefore, let us for the moment assume that the preconditioner for (4.3) is given by

$$\mathcal{P}_{BD} = \begin{bmatrix} L & \underline{0} \\ \underline{0}^T & 1 \end{bmatrix}. \tag{4.5}$$

Assuming that $\left(\lambda, \begin{bmatrix} \underline{v}_1 \\ v_2 \end{bmatrix}\right)$ represents an eigenpair of the preconditioned saddle point matrix $\mathcal{K}$, that means $\mathcal{P}_{BD}^{-1}\mathcal{K}$, we get

$$L\underline{v}_1 - \underline{m}v_2 = \lambda L\underline{v}_1 \tag{4.6}$$

$$-\underline{m}^T\underline{v}_1 = \lambda v_2. \tag{4.7}$$

If $\lambda = 1$ then from (4.6) we get that $-\underline{m}v_2 = \underline{0}$ which means that $v_2 = 0$ and hence (4.7) becomes $-\underline{m}^T\underline{v}_1 = 0$, i.e. the hyperplane given by $\underline{m}^\perp$ is the eigenspace of

$\lambda = 1$. As $\underline{m} \in \mathbb{R}^J$ has a $J-1$ dimensional kernel we obtain that the multiplicity of 1 is $J-1$. Now, for $\lambda \neq 1$ equation (4.6) gives that

$$\underline{v_1} = \frac{1}{1-\lambda} L^{-1} \underline{m} v_2$$

and by putting this into (4.7) we obtain

$$-\frac{1}{1-\lambda} \underline{m}^T L^{-1} \underline{m} v_2 = \lambda v_2.$$

Assuming now that σ is the eigenvalue of the Schur complement $\underline{m}^T L^{-1} \underline{m}$ of $\mathcal{K}$ we get

$$\lambda_1 = \frac{1}{2} + \sqrt{\frac{1}{4} + \sigma} \quad \text{and} \quad \lambda_2 = \frac{1}{2} - \sqrt{\frac{1}{4} + \sigma}$$

for the remaining two eigenvalues. This analysis indicates that for the Allen-Cahn variational inequality with volume constraint the preconditioning of the $(1,1)$ block of $\mathcal{K}$ is crucial as it can result in a clustering of the eigenvalues that guarantees fast convergence. Thus, we will only focus on efficient preconditioning strategies for the Allen-Cahn equation and then consider a preconditioner

$$\mathcal{P}_{BD} = \begin{bmatrix} A_0 & \underline{0} \\ \underline{0}^T & 1 \end{bmatrix} \tag{4.8}$$

where A_0 approximates the Allen-Cahn block. If one is willing to approximate the Schur complement $-\underline{m}^T L^{-1} \underline{m}$ of $\mathcal{K}$ techniques presented by Golub and Meurant in [64] can be used.

For the preconditioning of the Allen-Cahn block L we propose using algebraic multigrid (AMG). Multigrid methods use two complementary processes: smoothing and coarse-grid correction. Smoothing involves the application of a smoother which is in general a simple iterative method like Gauss-Seidel. Coarse-grid correction involves transferring information to a coarser grid and solving the coarse-grid system of equations. The solution is transferred back onto the fine grid through interpolation. This is a two-grid scheme. Multigrid methods are based on the recursive use of this two-grid scheme. A V-cycle multigrid method is obtained when the coarse problem is solved approximately with one iteration of the two-grid scheme on that level, and so on, until the coarsest level is reached on which the system is solved up to a given tolerance. The algebraic multigrid method [27, 106] was introduced for solving linear systems based on geometric multigrid principles, but in a way that only uses algebraic information. Typically, AMG methods exhibit geometric multigrid-like properties. When dealing with complicated geometries and meshes the algebraic multigrid tends to perform better than the geometric multigrid. An introduction to

AMG and the various AMG methods can be found in [55]. In our problems we solve the linear system (4.3) only on the interface and for some problems this domain can be quite complicated.

We have found now a promising preconditioner for the system matrix (4.3). Together with the Krylov subspace solver MINRES this should be a good choice of solver. We shall now demonstrate efficiency of this solver and preconditioner.

For the algebraic multigrid solver we used the ML package [63] which is available as part of Trilinos [71]. It can be used independently of Trilinos and the user only needs to provide two functions, one function for matrix-vector multiplication and another function that reads out the positions and the values of non-zero entries for given rows. This makes the package quite easy to use. Unfortunately, it also means that the ML routines need to get all the information from ALBERTA and there are many calls of the second function necessary, about two to three times as many as degrees of freedom. This makes the AMG less efficient and therefore we also considered an implementation where other packages of Trilinos are used as well. The system matrix L needs to be stored in CRS (compressed row storage) form and then the AMG routine can be used. The disadvantage is of course that we need memory for an additional matrix but on the other hand once we have the matrix all the work is done within Trilinos and we saved computation time by not communicating between software packages. We found that this approach was quicker than the first one, but one drawback is the additional memory required. This is especially the case for large problems. At this point one might be better off using a different software to ALBERTA. One big disadvantage of ALBERTA is that it uses its own `DOF_MATRIX` structure, which is very similar to the commonly used CRS structure, but cannot be used directly. Other finite element software packages work with more general matrix structures and hence it is easier to include additional software packages.

We apply AMG to the whole matrix L and then we only use the entries of the solution vector corresponding to $\mathcal{I}$. Thus the preconditioner only needs to be initialised once per time-step. For one application of the preconditioner we use in general five Gauss-Seidel smoothing steps [1] and one V-cycle.

We consider the following two dimensional test problem where the order parameter is initialised with random values between -0.1 and 0.1, see also Figure 2.4. We set $\varepsilon = \frac{1}{16\pi}$ and $\gamma = 1$ and we take the following discretisation parameters: $\tau = 1 \cdot 10^{-4}$, $h_{min} = \frac{1}{512}$, and $h_{max} = \frac{1}{16}$. Furthermore, we set the tolerance for MINRES to 10^{-9}. Figure 4.1 shows the average number of MINRES iterations per Newton iteration for the first 30 time-steps. Note that for the first 25 time-steps all nodes are inactive and hence only one Newton iteration is needed for each time-step. During this period the preconditioning works very well, reducing MINRES iterations up to a factor of 10. When bulk regions are present the average number of MINRES iterations

drops considerably when no preconditioning is used. Since more Newton iterations are needed (here we had around 10 Newton iterations per time-step) a good initial guess is provided for the second and all the following Newton iterations from the previous Newton iteration. Hence the average number of MINRES iterations is much lower. When preconditioning is used the average number of Newton iterations goes up slightly when the bulk regions have formed. This is due to the presence of active nodes. Recall that we approximate $L_{\mathcal{I},\mathcal{I}}^{-1}$ by using AMG for the whole matrix L and then only consider inactive nodes of the solution vector. It is to be expected that this type of preconditioning will work better when $L_{\mathcal{I},\mathcal{I}} = L$. Nevertheless, the reduction in iterations is still substantial. Less than a third MINRES iterations are needed on average when a preconditioner is used.

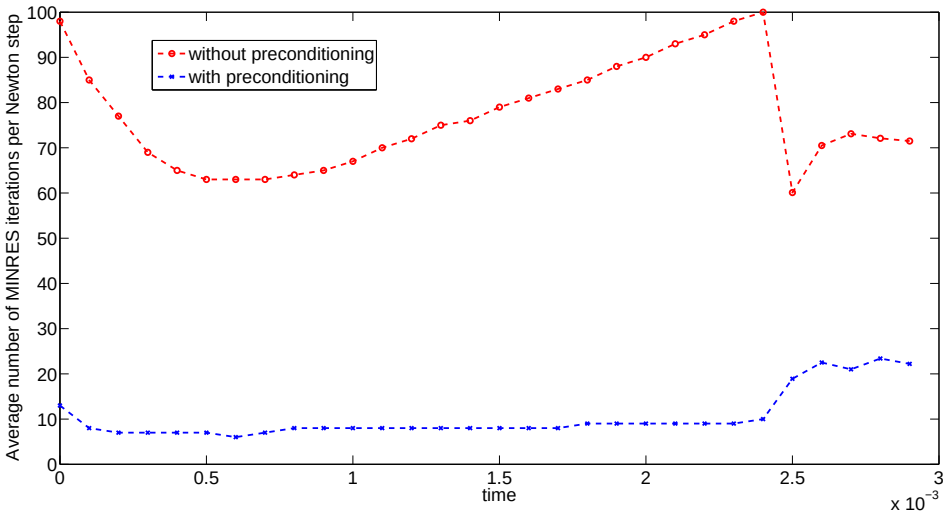

Figure 4.1: Average number of MINRES iterations for random data computation

Figure 4.2 shows the computation times for this problem. There is not much difference in computation times when preconditioning is used. For the first 20 iterations preconditioning reduces processing times, however, after bulk regions have been formed preconditioning fails to speed up computations. This indicates that the computational costs for initialising and applying AMG are too high compared to the costs for additional MINRES iterations.

There are situations where preconditioning will help. For example when using a uniform mesh AMG only needs to be initialised once at the beginning of the computation. Preconditioning should then speed up computations. Also, one might choose to use preconditioning only in the first few Newton iterations in each time-step. For subsequent Newton iterations good initial guesses should reduce the number of MINRES iterations already.

Moreover, using a different software package where AMG is already built-in or can be used more efficiently will also speed up computations with preconditioning.

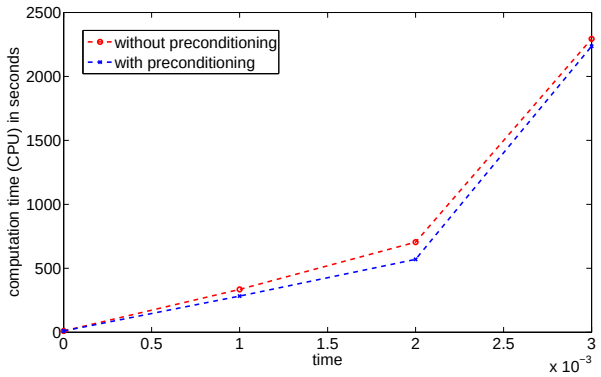

Figure 4.2: Computation times for random data computation with and without preconditioning.

4.2 Non-local vector-valued Allen-Cahn variational inequality

Now we consider the vector-valued non-local Allen-Cahn problem from Chapter 3. For simplicity we will only consider the case where W is the identity matrix. Without loss of generality we consider only 3 phases, i.e. $N = 3$. The generalisation is straight forward and all the ideas can be applied to arbitrarily many phases. After introducing active and inactive sets the equations (3.58) and (3.59) can be written as

$$\begin{bmatrix} L_{\mathcal{I}_1,\mathcal{I}_1} & 0 & 0 & -M_{\mathcal{I}_1,:} & -\underline{m}_{\mathcal{I}_1} & \underline{0} \\ 0 & L_{\mathcal{I}_2,\mathcal{I}_2} & 0 & -M_{\mathcal{I}_2,:} & \underline{0} & -\underline{m}_{\mathcal{I}_2} \\ 0 & 0 & L_{\mathcal{I}_3,\mathcal{I}_3} & -M_{\mathcal{I}_3,:} & \underline{m}_{\mathcal{I}_3} & \underline{m}_{\mathcal{I}_3} \\ -M_{:,\mathcal{I}_1} & -M_{:,\mathcal{I}_2} & -M_{:,\mathcal{I}_3} & 0 & 0 & 0 \\ -\underline{m}_{\mathcal{I}_1}^T & \underline{0}^T & \underline{m}_{\mathcal{I}_3}^T & 0^T & 0 & 0 \\ \underline{0}^T & -\underline{m}_{\mathcal{I}_2}^T & \underline{m}_{\mathcal{I}_3}^T & 0^T & 0 & 0 \end{bmatrix} \begin{bmatrix} (\underline{u}_1)_{\mathcal{I}_1} \\ (\underline{u}_2)_{\mathcal{I}_2} \\ (\underline{u}_3)_{\mathcal{I}_3} \\ \underline{\Lambda} \\ \lambda_1 \\ \lambda_2 \end{bmatrix} = \begin{bmatrix} \left(\frac{\varepsilon^2}{\tau} M \underline{u}_1^{(n-1)}\right)_{\mathcal{I}_1} \\ \left(\frac{\varepsilon^2}{\tau} M \underline{u}_2^{(n-1)}\right)_{\mathcal{I}_2} \\ \left(\frac{\varepsilon^2}{\tau} M \underline{u}_3^{(n-1)}\right)_{\mathcal{I}_3} \\ -\underline{m} \\ (m^3 - m^1)\,|\Omega| \\ (m^3 - m^2)\,|\Omega| \end{bmatrix}. \tag{4.9}$$

For a different choice of W the first 3 by 3 block changes and might loose the diagonal structure but it remains symmetric.

The system matrix in (4.9) is symmetric and indefinite and it is invertible under the stated time-step restriction. Finding a suitable solver is harder in this case. The conjugate gradient method does not work in most cases and/or is very inefficient. The direct solver UMFPACK can deal with smaller problems, i.e. two dimensional problems with N not too big. For larger problems we choose again MINRES as our preferred solver. For the vector-valued case the system matrix is much more complicated and a suitable preconditioning will help to speed up convergence.
We focus now on preconditioning. Since we do not want to compute a new preconditioner in every Newton iteration we work again with the 'full' matrix. Using that

$(\underline{u}_i)_{\mathcal{A}_i} = 0$ and $(\underline{\mu}_i)_{\mathcal{I}_i} = 0$ for $i \in \{1, ..., N\}$ the system (4.9) becomes

$$\begin{bmatrix} L & 0 & 0 & -M & -\underline{m} & \underline{0} \\ 0 & L & 0 & -M & \underline{0} & -\underline{m} \\ 0 & 0 & L & -M & \underline{m} & \underline{m} \\ -M^T & -M^T & -M^T & 0 & \underline{0} & \underline{0} \\ -\underline{m}^T & \underline{0}^T & \underline{m}^T & \underline{0}^T & 0 & 0 \\ \underline{0}^T & -\underline{m}^T & \underline{m}^T & \underline{0}^T & 0 & 0 \end{bmatrix} \begin{bmatrix} \underline{u}_1 \\ \underline{u}_2 \\ \underline{u}_3 \\ \underline{\Lambda} \\ \lambda_1 \\ \lambda_2 \end{bmatrix} = \begin{bmatrix} M\underline{\mu}_1 + \frac{\varepsilon^2}{\tau} M\underline{u}_1^{(k-1)} \\ M\underline{\mu}_2 + \frac{\varepsilon^2}{\tau} M\underline{u}_2^{(k-1)} \\ M\underline{\mu}_3 + \frac{\varepsilon^2}{\tau} M\underline{u}_3^{(k-1)} \\ -\underline{m} \\ (m^3 - m^1)\,|\Omega| \\ (m^3 - m^2)\,|\Omega| \end{bmatrix} \tag{4.10}$$

As in the scalar case we work implicitly only on the free variables given in (4.9). The variables $(\underline{\mu}_i)_{\mathcal{A}_i}$ are then determined by the first three lines. The system matrix in (4.10) is denoted by $\mathcal{K}_{vv}$ for the remainder of this section.

First, we note that $\mathcal{K}_{vv}$ is a saddle-point problem. In order to obtain a classical 2×2 saddle-point problem we have to decide how to split $\mathcal{K}_{vv}$. We propose the following splitting

$$B = \begin{bmatrix} L & 0 & 0 & -M \\ 0 & L & 0 & -M \\ 0 & 0 & L & -M \\ -M^T & -M^T & -M^T & 0 \end{bmatrix} \text{ and } C = \begin{bmatrix} -\underline{m}^T & \underline{0}^T & \underline{m}^T \\ \underline{0}^T & -\underline{m}^T & \underline{m}^T \end{bmatrix} \tag{4.11}$$

which we motivate by the following eigenvalue analysis. Assume that $(\lambda, \mathbf{v})$ is an eigenpair of the preconditioned problem $\mathcal{P}_{vv}^{-1}\mathcal{K}_{vv}$

$$\begin{bmatrix} B & C^T \\ C & 0 \end{bmatrix} \mathbf{v} = \lambda \begin{bmatrix} B & 0 \\ 0 & I \end{bmatrix} \mathbf{v} \tag{4.12}$$

where the matrix on the right hand side of the equation is the preconditioner $\mathcal{P}_{vv}$. Similar to the scalar case one can show [78, 91, 110] that there are $n_N - r$ eigenvalues at 1, where r is the rank of the matrix C and n_N is the size of the matrix B, or more precisely $n_N = (N+1)J$. For $N = 3$, C obviously has rank 2 and hence $n_N - 2$ eigenvalues can be found at 1. The remaining 4 eigenvalues can be found based on the eigenvalues of the Schur complement $CB^{-1}C^T$. Since in our case $n_N \gg 2$, we will not focus on a Schur complement approximation but rather on a good preconditioner for the block B. A good preconditioner for $\mathcal{K}_{vv}$ is hence

$$\mathcal{P}_{vv} = \begin{bmatrix} B & 0 \\ 0 & I \end{bmatrix}$$

and depends strongly on a good preconditioner for B. As B itself is of saddle point structure we need to devise an appropriate preconditioner. Again it is important to choose the splitting of

$$B = \begin{bmatrix} L & 0 & 0 & -M \\ 0 & L & 0 & -M \\ 0 & 0 & L & -M \\ -M^T & -M^T & -M^T & 0 \end{bmatrix}$$

carefully and we suggest to take the block-diagonal matrix $\mathrm{diag}(L, L, L)$ as the $\tilde{B}$ block and the "skinny" matrix $\tilde{C}$ is given by $\begin{bmatrix} -M^T - M^T & -M^T \end{bmatrix}$ to reveal the following 2×2 saddle point matrix

$$B = \begin{bmatrix} \tilde{B} & \tilde{C}^T \\ \tilde{C} & 0 \end{bmatrix}.$$

As mentioned before a preconditioner of B can be built from a good approximation of $\tilde{B}$ and of the Schur complement S of B, see page 68. $\tilde{B}$ is a block diagonal matrix containing Allen-Cahn equations and hence we can use an algebraic multigrid preconditioner for each of these blocks. Note that since we apply the preconditioner onto the whole matrix L and then modify the entries corresponding to active nodes, we only need to initialise the preconditioner once in each time-step.
Next we need to approximate the Schur complement of B, which for N phases is given by

$$S = N(M^T L^{-1} M)$$

However, when used with the active set method the individual matrices M and L might be of different size. Nevertheless, the goal for the Schur complement is to approximate the term $M^T L^{-1} M$ as accurately as possible. For now, we will look at

$$(M^T L^{-1} M)^{-1} = (\frac{\varepsilon^2}{\tau} - \gamma) M^{-T} + \varepsilon^2 \gamma M^{-1} A M^{-T}$$

which represents the application of the inverse of the exact Schur complement. Note that in a Krylov subspace solver only the action of matrices is required. For the above example this means that all we need to do is approximate the inverse of the mass matrix which in our case is a diagonal matrix.
We will use the MINRES method together with this preconditioning strategy and show some numerical results. For the AMG preconditioner we use again 5 Gauss-Seidel smoothing steps and 1 V-cycle.
First, we consider a two dimensional test problem where the order parameters are initialised with random values between 0 and 1 such that the sum constraint is

fulfilled and the volume constraints are roughly $m^1 = 0.4, m^2 = 0.2, m^3 = 0.4$. We take the following set of parameters $\varepsilon = \frac{1}{16\pi}$, $\gamma = 1$, $\tau = 1 \cdot 10^{-4}$, $h_{min} = \frac{1}{256}$, and $h_{max} = \frac{1}{16}$. Furthermore, we set the tolerance for MINRES to 10^{-10}. Figure 4.3 shows the average number of MINRES iterations per Newton iteration for the first 300 time-steps. As in the scalar case, at the beginning of the computation all nodes are inactive and only one Newton iteration is performed in each time-step. However, after only 6 time-steps we obtain non-empty active sets and the number of Newton iterations increases gradually. The difference in the averages of MINRES iterations with and without preconditioning is substantial at all times; however, it is again larger at the beginning of the computation when the initial value for MINRES is not too close to the solution.

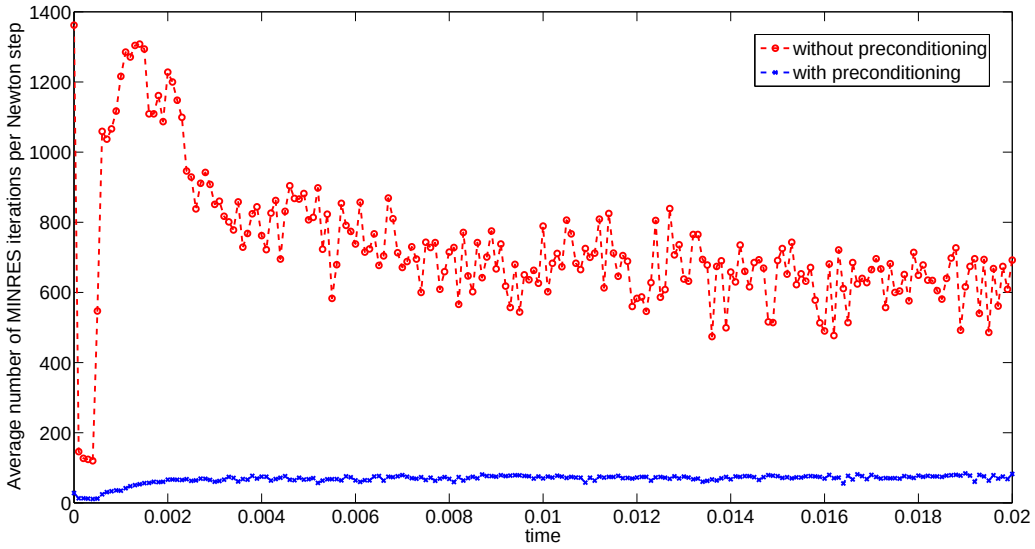

Figure 4.3: Average number of MINRES iterations for vector-valued random data computation

Figure 4.4 shows the computation times for this problem. With preconditioning the computation times are reduced by a factor of 3 or 4. The reduction is larger at the beginning of the computation when the iteration numbers are reduced more efficiently, but even later in the computation the preconditioning still speeds up computations.

For the second computation we use a three phase system consisting of two ellipses. The first two order parameters are each set to be 1 on one ellipse and 0 elsewhere. The interface is modelled to have a thickness of $\pi\varepsilon$ and the third order parameter is set such that the sum equates to 1 in each mesh point. The two ellipses are centred at $(-0.4, 0)$ and $(0.4, 0)$ and have major axes of 0.4 and 0.3 and minor axes of 0.15 and 0.2 respectively. As before we take $\varepsilon = \frac{1}{16\pi}$, $\gamma = 1$, $\tau = 1 \cdot 10^{-4}$, and we use an adaptive mesh with $h_{min} = \frac{1}{512}$ and $h_{max} = \frac{1}{16}$ which gives about 64000 mesh points. The tolerance for MINRES is set to be 10^{-10} as in the previous example.

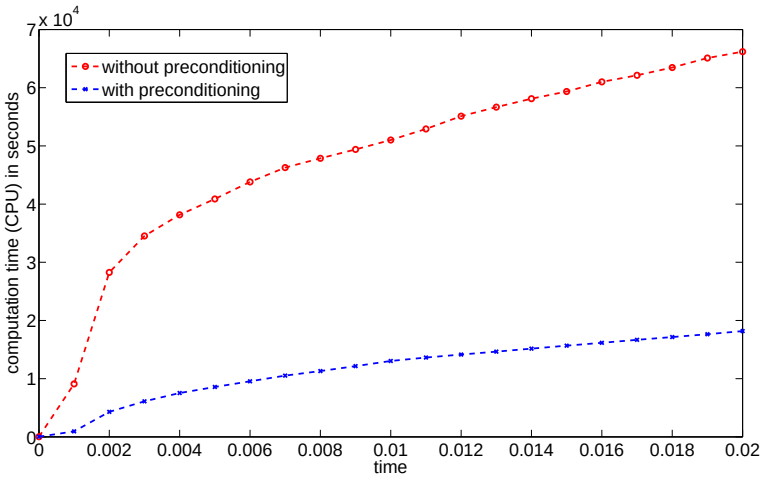

Figure 4.4: Computation times for vector-valued random data computation with and without preconditioning.

For this computation we use 10 steps of the Chebyshev smoother [1] rather than 5 Gauss-Seidel smoother steps. The Chebyshev smoother is rather cheap to apply and the preconditioning results obtained are very good. Figure 4.5 shows the average number of MINRES iterations per Newton iteration for the first 50 time-steps. The reduction in the number of iterations for the computation with preconditioning is always more than 10 times lower than without preconditioning. The computation time also reduces substantially when preconditioning is used, see Figure 4.6.

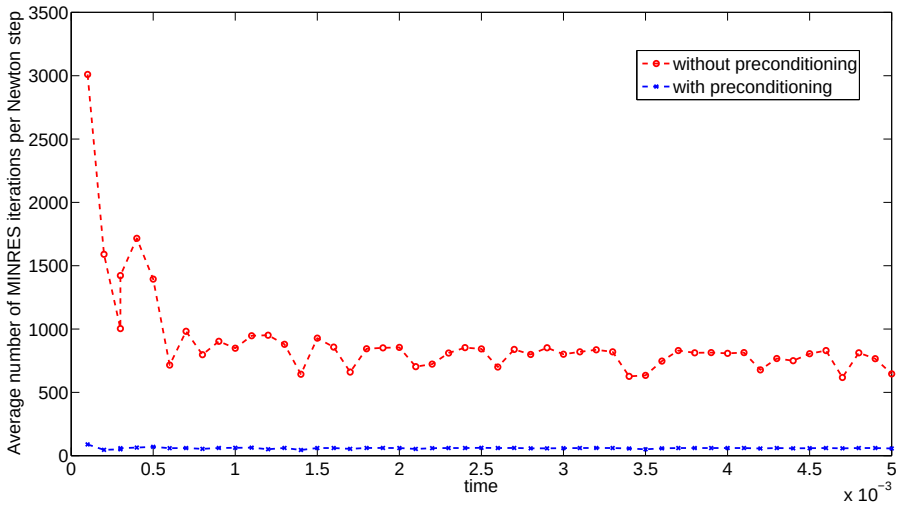

Figure 4.5: Average number of MINRES iterations for vector-valued volume conserved Allen-Cahn with ellipses as initial data.

In [22] computations were carried out using the software deal.II which comes with an interface for using the Trilinos library. The results were very similar, however, the differences in the computation times between preconditioned and non-preconditioned computations were slightly larger. Especially for three dimensional examples preconditioning reduced the computation time to about 25% of the unpre-

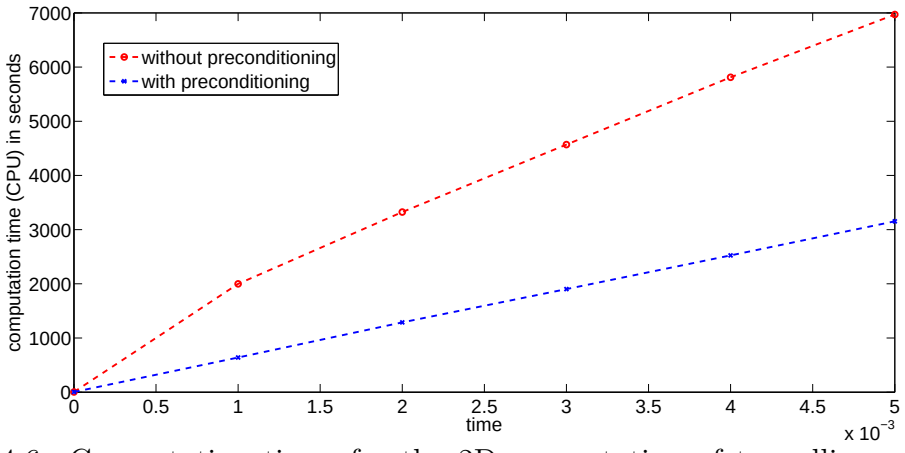

Figure 4.6: Computation times for the 2D computation of two ellipses with and without preconditioning.

conditioned computation. With ALBERTA we did not manage use AMG for three dimensional computations since the matrix that needs to be copied into CRS format requires too much storage.

In this chapter we have only presented a few computations. In conclusion, we have found that MINRES preforms very well. For the scalar Allen-Cahn problem it is not strictly necessary to use preconditioning as the number of MINRES iterations is relatively low due to good initial data provided by the previous Newton iteration. For the vector-valued Allen-Cahn equation preconditioning becomes more important. Especially for large problems, e.g. very large number of mesh points or large number of phases, the preconditioning strategy proposed in this chapter reduces computation times significantly. Depending on the problem under consideration one can work out the best strategy for solving the linear system.

Chapter 5

Applications

The phase field model was first introduced to address problems in materials science. More recently it has been used in various other fields including biology, geology and image processing. In this chapter we focus on three extensions of the classical phase field model. First, we consider an application to problems in structural topology optimisation where the non-local Allen-Cahn equation is coupled to a linear elasticity equation. Second, we introduce anisotropy to the model. This is an important feature for applications in materials science since most materials exhibit anisotropic behaviour. Finally, we use the Allen-Cahn equation to solve problems in image processing. We discuss image segmentation and denoising of grayscale and colour images and image inpainting for binary and grayscale images.

5.1 Structural topology optimisation

Structural topology optimisation denotes problems of finding optimal material distributions in a given design domain subject to certain criteria. It has become a standard tool of engineering design, in particular in structural mechanics, see e.g. [13]. There are two different problems of importance: (a) the maximisation of material stiffness at given mass, and (b) the minimisation of mass while keeping a certain stiffness. We consider only the first approach which is known as the minimal compliance problem and is today well understood with respect to its mathematical formulation, see [2] for an overview. Various successful numerical techniques have been proposed which rely on sensitivity analysis, mathematical programming, homogenisation, see [13] for an overview, or more recently on level-set and phase field methods [3, 116]. While level-set methods have become an accepted tool in structural topology optimisation, the use of phase field methods in this field has not yet become popular. There are only a few approaches considered, see [116, 30, 111]. These approaches use the Cahn-Hilliard equation which is obtained by taking the H^{-1} gradient flow of the Ginzburg-Landau energy (1.1). This is a fourth order

equation and hence the computational costs of solving this equation are very high. We use the volume conserved Allen-Cahn equation which is easier to solve and gives results that are very similar to the ones obtained using the Cahn-Hilliard equation.

5.1.1 Phase field formulation

We consider a structural topology optimisation problem of a statically loaded linear elastic structure. The goal is to compute the material distribution in a given bounded design domain $\Omega \subset \mathbb{R}^d$.
The material distribution is described by the phase field variable u which is 1 in the void and -1 if material is present. We prescribe a given mass by using the volume constraint $\fint_\Omega u = m$ where $m \in (-1, 1)$. We now assume a linear elastic material with an elasticity tensor $\mathcal{C}_1$ and we model the void with a very small elasticity tensor $\mathcal{C}_2$ where we later choose $\mathcal{C}_2 = \varepsilon^2 \mathcal{C}_1$ but other choices are possible. In the interfacial region we interpolate the elastic properties and set

$$\mathcal{C}(u) = \mathcal{C}_1 + \tfrac{1}{2}(1+u)(\mathcal{C}_2 - \mathcal{C}_1)\,.$$

We now denote by $\mathbf{v} : \Omega \to \mathbb{R}^d$ the displacement vector and by $\mathcal{E}(\mathbf{v}) := \frac{1}{2}(\nabla \mathbf{v} + \nabla \mathbf{v}^t)$ the strain tensor. Assuming that the outer forces are given by a linear functional F on the Sobolev space $\mathbf{H}^1 := H^1(\Omega)^d$ the goal in classical structural topology optimisation is to minimise the mean compliance $F(\mathbf{v})$ subject to $\fint_\Omega u(x)dx = m$ and

$$\langle \mathcal{E}(\mathbf{v}), \mathcal{E}(\boldsymbol{\eta}) \rangle_{\mathcal{C}(u)} = F(\boldsymbol{\eta}) \tag{5.1}$$

which has to hold for all $\boldsymbol{\eta} \in \mathbf{H}^1(\Omega)$ such that $\boldsymbol{\eta} = \mathbf{0}$ on a given non-empty Dirichlet boundary Γ_D. Here we use the notation

$$\langle \mathcal{A}, \mathcal{B} \rangle_{\mathcal{C}} := \fint_\Omega \mathcal{A} : \mathcal{C}\mathcal{B}$$

where the :–product of matrices $\mathcal{G}$ and $\mathcal{H}$ is given as $\mathcal{G} : \mathcal{H} := \sum_{i,j=1}^d \mathcal{G}_{ij}\mathcal{H}_{ij}$.
The outer forces F can be given for example by a boundary traction on $\Gamma_F \subset \partial\Omega \backslash \Gamma_D$ and in this case we have

$$F(\boldsymbol{\eta}) = \int_{\Gamma_F} \mathbf{f} \cdot \boldsymbol{\eta} \tag{5.2}$$

where $\mathbf{f} : \Gamma_F \to \mathbb{R}^d$ describes outer forces acting on the structure. The strong

formulation of (5.1) with F of the form (5.2) is now given as

$$\begin{aligned} -\nabla \cdot [\mathcal{C}(u)\mathcal{E}(\mathbf{v})] &= 0 && \text{in } \Omega\,, \\ \mathbf{v} &= \mathbf{0} && \text{on } \Gamma_D\,, \\ [\mathcal{C}(u)\mathcal{E}(\mathbf{v})] \cdot \nu &= \mathbf{f} && \text{on } \Gamma_F\,, \\ [\mathcal{C}(u)\mathcal{E}(\mathbf{v})] \cdot \nu &= \mathbf{0} && \text{on } \partial\Omega \setminus (\Gamma_D \cup F_F)\,. \end{aligned}$$

In the above formulation the problem is ill-posed and unwanted checkerboard patterns and mesh dependencies are well-known phenomena, see [109].
A possible regularisation is to add a perimeter penalisation to the functional which penalises length for $d = 2$ and area if $d = 3$ for the interface between material and void. This regularisation in particular avoids checkerboard patterns if spatial discretisation parameters tend to zero, see [70, 96].
In phase field approaches such a penalisation can be modelled with the help of the Ginzburg-Landau energy $E(u)$, see (1.1). It is well known that this energy converges to a scalar multiple of the perimeter functional, see [89].
We now want to solve

$$\min J(u, \mathbf{v}) := E(u) + F(\mathbf{v}) \tag{5.3}$$

subject to (5.1) and $\fint_\Omega u(x)dx = m$. For a given u we can compute a unique $\mathbf{v}(u)$ with $\mathbf{v}(u) = \mathbf{0}$ on Γ_D which solves (5.1). We can hence consider the reduced problem

$$\min \hat{J}(u) \quad \text{subject to} \quad \fint_\Omega u(x)dx = m \tag{5.4}$$

with the reduced functional

$$\hat{J}(u) := J(u, \mathbf{v}(u))\,.$$

In order to compute the first variation of the reduced functional $\hat{J}$ we apply a formal Lagrange approach, see e.g. Hinze et al. [73]. We therefore introduce the adjoint variable $\mathbf{p} : \Omega \to \mathbb{R}^d$ and define the Lagrangian

$$L(u, \mathbf{v}, \mathbf{p}) := E(u) + F(\mathbf{v}) - \langle \mathcal{E}(\mathbf{v}), \mathcal{E}(\mathbf{p}) \rangle_{\mathcal{C}(u)} + F(\mathbf{p})\,.$$

We now seek stationary states $(u, \mathbf{v}, \mathbf{p})$ of L. If the first variation for $(u, \mathbf{v}, \mathbf{p})$ vanishes we observe that $\mathbf{v}$ and $\mathbf{p}$ both solve (5.1). Assuming $\Gamma_D \neq \emptyset$ we obtain that (5.1) has a unique solution with Dirichlet data on Γ_D [120, Chapter 61] and we hence conclude $\mathbf{v} \equiv \mathbf{p}$. Using this we obtain

$$\tfrac{\delta \hat{J}}{\delta u}(u) = \tfrac{\delta L}{\delta u}(u, \mathbf{v}, \mathbf{p}) = \tfrac{\delta E}{\delta u}(u) - \langle \mathcal{E}(\mathbf{v}), \mathcal{E}(\mathbf{v}) \rangle_{\mathcal{C}'(u)}\,,$$

where $\frac{\delta \hat{J}}{\delta u}$, $\frac{\delta L}{\delta u}$ and $\frac{\delta E}{\delta u}$ denote the first variation with respect to u and $\mathbf{v}$ solves (5.1). As for the standard phase field model we now use a steepest descent approach in order to find (local) minima of (5.4). We use the L^2–gradient flow, where also the mass constraint $\fint_\Omega u = m$ has to be enforced. Note that in the context of topology optimisation the time variable is artificial and leads to a pseudo time-stepping approach. Using the obstacle potential (1.4) we obtain on an arbitrary time interval $(0,T)$:

$(\mathbf{P}_1)$ *Find* $u \in H^1(\Omega_T)$ *and* $\mathbf{v} \in L^\infty(0,T;\mathbf{H}^1(\Omega))$ *such that*

$$\begin{aligned}
&\fint_\Omega u(x,t)dx = m, u(.,0) = u_0, |u| \leq 1 \text{ a.e. in } \Omega_T, \mathbf{v} = \mathbf{0} \text{ a.e. on } \Gamma_D \times (0,T)\,,\\
&(\varepsilon \partial_t u + \tfrac{\gamma}{\varepsilon}\psi_0'(u), \chi - u) + \gamma\varepsilon(\nabla u, \nabla(\chi - u)) \geq \tfrac{1}{2}\langle \mathcal{E}(\mathbf{v}), \mathcal{E}(\mathbf{v})(\chi - u)\rangle_{\mathcal{C}_2 - \mathcal{C}_1}\,,\\
&\langle \mathcal{E}(\mathbf{v}), \mathcal{E}(\boldsymbol{\eta})\rangle_{\mathcal{C}(u)} = F(\boldsymbol{\eta})
\end{aligned}$$

which has to hold for almost all t *and all* $\chi \in H^1(\Omega)$ *with* $|\chi| \leq 1$ *and* $\fint_\Omega \chi = m$ *and all* $\boldsymbol{\eta} \in \mathbf{H}^1(\Omega)$ *such that* $\boldsymbol{\eta} = \mathbf{0}$ *on the Dirichlet boundary* Γ_D.

Stationary states of $(\mathbf{P}_1)$ fulfil the first order necessary conditions for (5.3).

5.1.2 Discretisation

In this section we describe how we solve $(\mathbf{P}_1)$ numerically. We use the notation from 2.4.1. In addition to that, we employ a quadrature formula $\langle \mathcal{A}, \mathcal{B}\rangle_{\mathcal{C}}^h$ in place of $\langle \mathcal{A}, \mathcal{B}\rangle_{\mathcal{C}}$, with the property that $\langle \mathcal{A}, \mathcal{B}\rangle_{\mathcal{C}}^h = \langle \mathcal{A}, \mathcal{B}\rangle_{\mathcal{C}}$ for piecewise affine linear integrands $\mathcal{A} : \mathcal{C}\mathcal{B}$.

Taking a fixed time step $\tau = t_n - t_{n-1}$ we obtain the following finite element approximation of $(\mathbf{P}_1)$:

$(\mathbf{P}_1^h)$ *Given* $u_h^{n-1} \in \mathcal{K}_h^m$ *find* $(u_h^n, \mathbf{v}_h^n) \in \mathcal{K}_h^m \times (S_h)^d$ *such that*

$$\begin{aligned}
\mathbf{v}_h^n &= \mathbf{0} \text{ on } \boldsymbol{\Gamma}_D\,,\\
\langle \mathcal{E}(\mathbf{v}_h^n), \mathcal{E}(\boldsymbol{\eta})\rangle_{\mathcal{C}(u_h^{n-1})}^h &= F(\boldsymbol{\eta}) \quad \forall\ \boldsymbol{\eta} \in (S_h)^d \text{ with } \boldsymbol{\eta} = \mathbf{0} \text{ on } \Gamma_D\,, \qquad (5.5)\\
(\tfrac{\varepsilon}{\tau}(u_h^n - u_h^{n-1}) - \tfrac{\gamma}{\varepsilon}u_h^n, \chi - u_h^n)_h &+ \gamma\varepsilon(\nabla u_h^n, \nabla(\chi - u_h^n))\\
&\geq \tfrac{1}{2}\langle \mathcal{E}(\mathbf{v}_h^n), \mathcal{E}(\mathbf{v}_h^n)(\chi - u_h^n)\rangle_{\mathcal{C}_2 - \mathcal{C}_1}^h \ \ \forall \chi \in \mathcal{K}_h^m. \qquad (5.6)
\end{aligned}$$

As (5.5) is independent of u_h^n we use a preconditioned conjugate gradient solver to compute $\mathbf{v}_h^n$ from this equation, see also [62, 60]. As in Chapter 2 we can reformulate (5.6) with Lagrange multipliers $\mu_h \in S_h$ and $\lambda \in \mathbb{R}$:

Given $(u_h^{n-1}, \mathbf{v}_h^n) \in \mathcal{K}_h^m \times (S_h)^d$, *find* $u_h^n \in \mathcal{K}_h^m$, $\mu_h \in S_h$ *and* $\lambda \in \mathbb{R}$ *such that*

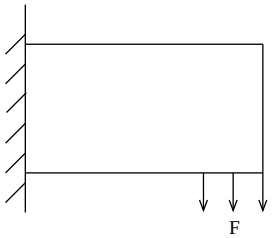

Figure 5.1: The design domain for a cantilever beam

$$(\tfrac{\varepsilon^2}{\tau}-\gamma)(u_h^n,\chi)_h+\gamma\varepsilon^2(\nabla u_h^n,\nabla\chi)+(\mu_h,\chi)_h-\lambda(1,\chi)$$
$$=\tfrac{\varepsilon^2}{\tau}(u_h^{n-1},\chi)_h+\tfrac{\varepsilon}{2}\langle\mathcal{E}(\mathbf{v}_h^n),\mathcal{E}(\mathbf{v}_h^n)\chi\rangle_{\mathcal{C}_2-\mathcal{C}_1}^h \quad \forall\chi\in S_h, \tag{5.7}$$
$$\fint_\Omega u_h^n=m, \tag{5.8}$$
$$(\mu_j)_-\geq 0,\ (\mu_j)_+\geq 0,\ |u_j|\leq 1, \tag{5.9}$$
$$(u_j+1)(\mu_j)_-=(u_j-1)(\mu_j)_+=0 \quad \forall\ j\in\mathcal{J}. \tag{5.10}$$

To solve (5.7)-(5.10) we apply the PDAS-method.

5.1.3 Numerical simulations

In this section we present a numerical simulation for a cantilever beam geometry, see Figure 5.1. We pose Dirichlet boundary conditions on the left boundary Γ_D and a vertical force is acting at the bottom of its free vertical edge. We take $\Omega = (-1,1)\times(0,1)$, and hence $\Gamma_D = \{(-1,y)\in\mathbb{R}^2 : y\in[0,1]\}$. The force F is acting on $\Gamma_F := \{(x,0)\in\mathbb{R}^2 : x\in[0.75,1]\}$ and is defined by $\mathbf{f}(x)=(0,250)^T$ for $x\in\Gamma_F$. In our computations we use an isotropic elasticity tensor $\mathcal{C}_1$ of the form $\mathcal{C}_1\mathcal{E}=2\mu_1\mathcal{E}+\lambda_1(tr\mathcal{E})I$ with the Lamé constants $\lambda_1=\mu_1=5000$ and choose $\mathcal{C}_2=\varepsilon^2\mathcal{C}_1$ in the void. We initialise the order parameter u with random values between -0.1 and 0.1 which ensures that we approximately have the same proportion of material and void, i.e. $m\approx 0$. We set the interfacial parameters $\varepsilon=\frac{1}{16\pi}$ and $\gamma=1$ and we take the minimal diameter of all elements $h_{min}=\frac{1}{128}$ and the maximal diameter $h_{max}=\frac{1}{16}$. The time-step is chosen as $t=6.25\cdot 10^{-6}$.
Figure 5.2 shows the results obtained where the state at $t=0.160$ appears to be a numerical steady state.
In [20] the volume conserved Allen-Cahn and the Cahn-Hilliard model are used for this numerical simulation. Using a very similar set of data it was found that the optimal shape is almost the same. However, the evolution towards this shape is very different. For the Allen-Cahn approach the final structure evolves directly from the random initial state within the same spatial scale whereas for the Cahn-Hilliard approach the evolution follows a coarsening process from fine scale structures to

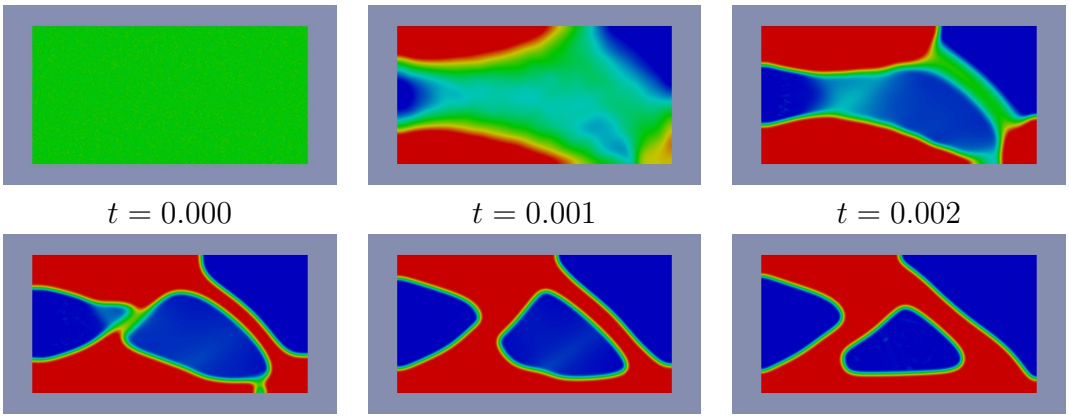

Figure 5.2: Allen-Cahn results for the cantilever beam computation at various times; material in red and void in blue.

coarser scales. This results from the spinodal decomposition in the early evolution. For structural topology optimisation only the final state is of interest and the computations in [20] demonstrate that the Cahn-Hilliard model can be replaced by a volume conserved Allen-Cahn equation which reduces computational costs considerably and makes the phase field approach more efficient.

5.1.4 Multi-structural topology optimisation

The phase field approach described above can be generalised for multi-material structural topology optimisation. Zhou and Wang [116] used multi-phase Cahn-Hilliard equations for this purpose. We demonstrate that the non-local vector-valued Allen-Cahn equation can be used instead. Very similar to the scalar case we can consider the minimisation problem

$$\min J(\boldsymbol{u}, \mathbf{v}) := E(\boldsymbol{u}) + F(\mathbf{v})$$

subject to $\langle \mathcal{E}(\mathbf{v}), \mathcal{E}(\mathbf{v}) \rangle_{\mathcal{C}(\boldsymbol{u})} = F(\mathbf{v})$ and $\fint_\Omega \boldsymbol{u} = \boldsymbol{m}$. The elasticity tensor $\mathcal{C}(\boldsymbol{u})$ is defined as $\mathcal{C}(\boldsymbol{u}) = \sum_{i=1}^{N} \mathcal{C}_i u_i$ where $\mathcal{C}_i$ is the elasticity tensor of the material represented by the i-th phase.

We can use the same formal Lagrangian approach for this minimisation problem as before to obtain the following variational problem:

Find $\boldsymbol{u} : \Omega \times [0,\infty) \to \mathbb{R}^N$ *and* $\mathbf{v} : \Omega \times [0,\infty) \to \mathbb{R}^d$ *such that*

$$\fint_\Omega \boldsymbol{u}(x,t)dx = \boldsymbol{m}, \boldsymbol{u}(.,0) = \boldsymbol{u}_0, \boldsymbol{u} \geq \mathbf{0}, \quad a.e., \sum_{i=1}^{N} u_i = 1, \mathbf{v} = \mathbf{0} \quad a.e. \text{ on } \Gamma_D \times (0,\infty), \tag{5.11}$$

$$(\varepsilon \partial_t u_i, \chi - u_i) + \gamma\varepsilon(\nabla u_i, \nabla(\chi - u_i)) + \tfrac{\gamma}{\varepsilon}((W\boldsymbol{u})_i, \chi - u_i) \geq \langle \mathcal{E}(\mathbf{v}), \mathcal{E}(\mathbf{v})(\chi - u_i)\rangle_{\mathcal{C}_i} \tag{5.12}$$

$$\langle \mathcal{E}(\mathbf{v}), \mathcal{E}(\boldsymbol{\eta})\rangle_{\mathcal{C}(\boldsymbol{u})} = F(\boldsymbol{\eta}) \tag{5.13}$$

which has to hold for all $i \in \{1, ..., N\}$ *and for almost all* t *and all* $\chi \in H^1(\Omega)$ *with* $|\chi| \leq 1$ *and* $\fint_\Omega \chi = m$ *and all* $\boldsymbol{\eta} \in \mathbf{H}^1(\Omega)$ *such that* $\boldsymbol{\eta} = \mathbf{0}$ *on a given Dirichlet boundary* Γ_D.

This problem is then discrete in time and space and the primal-dual active set strategy is used to solve the modified vector-valued Allen-Cahn equation with volume constraints.

In structural topology optimisation the 120° angle condition at triple junctions is not in all cases realistic. In the following we consider a system consisting of hard material, soft material and void. When all these three structures meet at a triple point 120° angles would suggest that the soft and hard material 'break apart'. This is not realistic and can be overcome by adjusting the matrix W in the multi-obstacle potential. Assuming that the hard material is described by u_1, the soft material by u_2 and the void by u_3 we take

$$W = \begin{pmatrix} 0 & -0.1 & -1 \\ -0.1 & 0 & -1 \\ -1 & -1 & 0 \end{pmatrix}$$

which forces the angle at the void to be larger than the other two angles.

We use the same cantilever beam geometry as for the scalar case, see Figure 5.1. The force acting on Γ_F is again defined as $\mathbf{f}(x) = (0, 250)^T$ if $x \in \Gamma_F$ and $\mathbf{0}$ otherwise. In our computations we use 40% hard material, 20% soft material and 40% void. For the hard material (associated with phase 1) we use the Lame constants $\lambda_1 = \mu_1 = 5000$; for the soft material (associated with phase 2) we choose $\mathcal{C}_2 = \frac{1}{2}\mathcal{C}_1$ and for the void we take $\mathcal{C}_2 = (2\varepsilon)^2\mathcal{C}_1$. We set $\gamma = 1$, $\tau = 6.25 \times 10^{-6}$ and use an adaptive mesh with $h_{min} = \frac{1}{128}$ and $h_{max} = \frac{1}{8}$. We initialise the order parameter $\boldsymbol{u}$ with random values such that the sum constraint is fulfilled and the proportions of hard material, soft material and void are as required. Figure 5.3 shows the results obtained, where the state at $t = 0.330$ appears to be a numerical steady state.

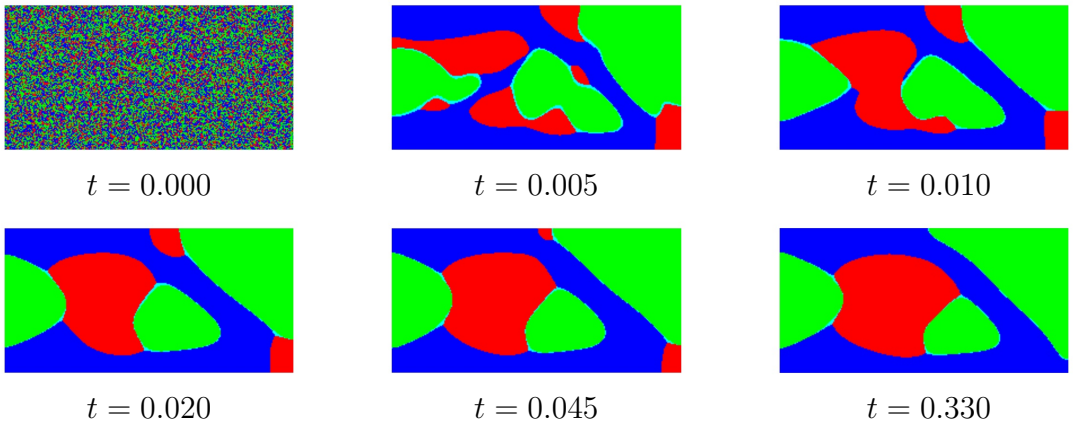

Figure 5.3: Results for the cantilever beam computation at various times; hard material in blue, soft material in red and void in green.

5.2 Anisotropy

Up to now we considered only isotropic motion by mean curvature. All properties of the materials involved were homogeneous in all directions which resulted in circles and spheres as optimal shapes. However, most materials exhibit anisotropic behaviour which means that one or more of their physical properties are directionally dependent. Hence optimal shapes can include corners or edges. In this section we discuss the incorporation of anisotropy into the Allen-Cahn model.

5.2.1 Anisotropic Allen-Cahn variational inequality

Surface energy anisotropy was first included in phase field models by Kobayashi [80] to describe dendritic crystal growth. We recall that the Ginzburg-Landau energy (1.1) does not depend on the direction of ∇u. Replacing the gradient term in (1.1), we get

$$E(u) := \int_\Omega (\varepsilon A(\nabla u) + \tfrac{1}{\varepsilon}\psi(u))dx \tag{5.14}$$

where $A \in C^2(\mathbb{R}^d)$ is a strictly convex function with the following properties:

(i) A is homogeneous of degree two, that is $A(\lambda \mathbf{p}) = \lambda^2 A(\mathbf{p})$ for $\lambda > 0$ and $\mathbf{p} \in \mathbb{R}^d$;

(ii) $A(\mathbf{p}) \geq 0$ for $\mathbf{p} \in \mathbb{R}^d \setminus \{\mathbf{0}\}$.

This problem is anisotropic, see e.g. [112], and taking the gradient flow of this energy we obtain the corresponding Allen-Cahn variational inequality

$$\varepsilon(\partial_t u, \chi - u) + \varepsilon(A'(\nabla u), \nabla(\chi - u)) + \tfrac{1}{\varepsilon}(\psi_0'(u), \chi - u) \geq 0, \tag{5.15}$$

which has to hold for almost all t and all $\chi \in H^1(\Omega)$ with $|\chi| \leq 1$.

McFadden et al. [86], Wheeler and McFadden [117], Bellettini and Paolini [10] used formal asymptotics to prove the conjecture that the anisotropic Allen-Cahn equation with smooth potential ψ approximates the anisotropic mean curvature flow, which reads

$$V = -H_\gamma \gamma(\varsigma) \tag{5.16}$$

where $\gamma := \sqrt{2A}$ is the anisotropic interface energy density, ς is the unit normal of the interface Γ and H_γ is the anisotropic mean curvature of Γ which is defined as

$$H_\gamma(x) = \nabla_\Gamma \cdot D\gamma(\varsigma(x))$$

for all $x \in \Gamma$. Note that for $\gamma(\mathbf{p}) = |\mathbf{p}|$ we obtain $H_\gamma = \nabla_\Gamma \cdot \varsigma(x)$ which is the mean curvature. Elliott and Schätzle [49] proved that solutions of the anisotropic Allen-Cahn equation with double obstacle potential, i.e. of the variational inequality (5.15), converge to the anisotropic mean curvature flow.
Anisotropy is normally visualised by using the Frank diagram $\mathcal{F}$ and the Wulff shape $\mathcal{W}$:

$$\mathcal{F} = \{\mathbf{p} \in \mathbb{R}^d : \gamma(\mathbf{p}) \leq 1\}, \quad \mathcal{W} = \{\mathbf{q} \in \mathbb{R}^d : \gamma^*(\mathbf{q}) \leq 1\},$$

where γ^* is the dual of γ, which is given by

$$\gamma^*(\mathbf{q}) = \sup_{\mathbf{p} \in \mathbb{R}^d \setminus \{0\}} \frac{\mathbf{p} \cdot \mathbf{q}}{\gamma(\mathbf{p})}.$$

For a fixed volume, the boundary of the (rescaled) Wulff shape is the energetically optimal shape of the interface under the anisotropic energy (5.14). For the choice $\gamma(\mathbf{p}) = |\mathbf{p}|$, i.e. for the isotropic case, we have that $\mathcal{F} = \mathcal{W} = \{\mathbf{p} \in \mathbb{R}^d : |\mathbf{p}| \leq 1\}$ is the closed unit ball. Typical choices for anisotropy are the discrete l^r-norms for $1 \leq r \leq \infty$,

$$\gamma(\mathbf{p}) = \|\mathbf{p}\|_{l^r} = \left(\sum_{k=1}^{d} |p_k|^r \right)^{\frac{1}{r}},$$

with the obvious modification for $r = \infty$. For our problems, however, we need γ to be sufficiently smooth and hence regularised versions of the l^r-norms should be used.

5.2.2 Discretisation and primal-dual active set method

In the following we will discretise (5.15) using implicit Euler in time and finite elements in space and then apply the primal-dual active set method derived in Chapter 2. We use the same notation as before. Furthermore, we use that $\psi_0'(u) = -u$. The fully discrete problem reads as follows:

Given $u_h^{n-1} \in \mathcal{K}_h$ *find* $u_h = u_h^n \in \mathcal{K}_h$ *such that*

$$(\tfrac{\varepsilon}{\tau}(u_h - u_h^{n-1}) - \tfrac{1}{\varepsilon}u_h, \chi - u_h)_h + \varepsilon(\nabla A'(\nabla u_h), \nabla(\chi - u_h)) \geq 0 \;\; \forall \chi \in \mathcal{K}_h.$$

We can reformulate this variational problem using a Lagrange multiplier $\mu_h \in S_h$ in the same way as for the isotropic Allen-Cahn equation and we obtain:
Find $u_h \in S_h$ *and* $\mu_h \in S_h$ *such that*

$$(\tfrac{\varepsilon^2}{\tau} - 1)(u_h, \varphi)_h + \varepsilon^2(A'(\nabla u_h), \nabla\varphi) + (\mu_h, \varphi)_h = \tfrac{\varepsilon^2}{\tau}(u_h^{n-1}, \varphi)_h \;\; \forall \varphi \in S_h\,, \tag{5.17}$$

$$(\mu_j)_- \geq 0,\;\; (\mu_j)_+ \geq 0,\;\; |u_j| \leq 1, \tag{5.18}$$

$$(u_j + 1)(\mu_j)_- = (u_j - 1)(\mu_j)_+ = 0 \quad \forall\; j \in \mathcal{J}. \tag{5.19}$$

As in (2.37) the complementarity condition can be rewritten as

$$\mathcal{H}(u_j, \mu_j) := \mu_j - c\left[\max(0, \tfrac{\mu_j}{c} + (u_j - 1)) + \min(0, \tfrac{\mu_j}{c} + (u_j + 1))\right] = 0 \qquad \forall j \in \mathcal{J}. \tag{5.20}$$

We now consider the system (5.17) - (5.20) as a problem of finding a root of $\boldsymbol{F}(\underline{u}, \underline{\mu}, \lambda) = \mathbf{0}$ by using a semi-smooth Newton method

$$\boldsymbol{G}(\underline{u}^k, \underline{\mu}^k, \lambda^k)((\underline{u}^{k+1}, \underline{\mu}^{k+1}, \lambda^{k+1}) - (\underline{u}^k, \underline{\mu}^k, \lambda^k)) = -\boldsymbol{F}(\underline{u}^k, \underline{\mu}^k, \lambda^k)$$

where $\boldsymbol{G}$ is a slanting function for $\boldsymbol{F}$. For $\mathcal{H}$ we can use the slanting function defined in (2.40), (2.41). Hence we only need to find a slanting function for (5.17). Using that $\frac{d}{du}(\nabla \cdot A'(\nabla u))v = \nabla \cdot A''(\nabla u)\nabla v$ and applying the semi-smooth Newton method to (5.17) gives

$$\begin{aligned}((\tfrac{\varepsilon^2}{\tau} - 1)(u^{k+1} - u^k), \varphi)_h + \varepsilon^2(A''(\nabla u^k)\nabla(u^{k+1} - u^k), \nabla\varphi) + (\mu^{k+1} - \mu^k, \varphi)_h = \\ \tfrac{\varepsilon^2}{\tau}(u_h^{n-1}, \varphi)_h - ((\tfrac{\varepsilon^2}{\tau} - 1)u^k, \varphi)_h - \varepsilon^2(A'(\nabla u^k), \nabla\varphi) - (\mu^k, \varphi)_h.\end{aligned} \tag{5.21}$$

Defining $M := (\chi_i, \chi_j)_h$ and $S := (A''(\nabla u^k)\nabla\chi_i, \nabla\chi_j)$ we derive for $\boldsymbol{F}$ the slanting function

$$\boldsymbol{G}(\underline{u}, \underline{\mu}, \lambda) = \begin{pmatrix} (\tfrac{\varepsilon^2}{\tau} - \gamma)M + \gamma\varepsilon^2 S & M \\ \mathcal{G}_u(\underline{u}, \underline{\mu}) & \mathcal{G}_\mu(\underline{u}, \underline{\mu}) \end{pmatrix}. \tag{5.22}$$

Since A is homogeneous of degree two and hence in particular A' is homogeneous of degree one, it follows from Euler's homogeneous function theorem [98] that $A''(\mathbf{p}) \cdot$

$\mathbf{p} = A'(\mathbf{p})$ for all $\mathbf{p} \in \mathbb{R}^d \setminus \{\mathbf{0}\}$. Using this in (5.21) we obtain

$$((\tfrac{\varepsilon^2}{\tau} - 1)u^{k+1}, \varphi)_h + \varepsilon^2(A''(\nabla u^k)\nabla u^{k+1}, \nabla\varphi) + (\mu^{k+1}, \varphi)_h = \tfrac{\varepsilon^2}{\tau}(u_h^{n-1}, \varphi)_h. \quad (5.23)$$

The resulting algorithm now reads as follows:

0. Set $k = 0$ and initialise $\mathcal{A}_0^{\pm}$.

1. Define $\mathcal{I}_k = \mathcal{J} \setminus (\mathcal{A}_k^+ \cup \mathcal{A}_k^-)$.
Set $u_j^k = \pm 1$ for $j \in \mathcal{A}_k^{\pm}$ and $\mu_j^k = 0$ for $j \in \mathcal{I}_k$.

2. Solve the discrete PDE (5.23) to obtain u_j^k for $j \in \mathcal{I}_k$:

$$(\tfrac{\varepsilon}{\tau} - \tfrac{1}{\varepsilon})m_j u_j^k + \varepsilon \sum_{i \in \mathcal{I}_k} s_{ij} u_i^k = \tfrac{\varepsilon}{\tau} m_j u_j^{n-1} + \varepsilon(\sum_{i \in \mathcal{A}_k^-} s_{ij} - \sum_{i \in \mathcal{A}_k^+} s_{ij}) \qquad \forall j \in \mathcal{I}_k. \quad (5.24)$$

3. Determine μ_j^k for $j \in \mathcal{A}_k^{\pm}$ using (5.17):

$$\mu_j^k = -(\tfrac{\varepsilon^2}{\tau} - 1)u_j^k - \varepsilon^2 \tfrac{1}{m_j} \sum_{i \in \mathcal{J}} s_{ij} u_i^k + \tfrac{\varepsilon^2}{\tau} u_j^{n-1}.$$

4. Set $\mathcal{A}_{k+1}^+ := \{j \in \mathcal{J} : u_j^k + \frac{\mu_j^k}{c} > 1\}$, $\mathcal{A}_{k+1}^- := \{j \in \mathcal{J} : u_j^k + \frac{\mu_j^k}{c} < -1\}$.

5. If $\mathcal{A}_{k+1}^{\pm} = \mathcal{A}_k^{\pm}$ goto 6, otherwise set $k = k + 1$ and goto 1.

6. If $\max_{j \in \mathcal{J}}(u_j^{k-1} - u_j^k) > tol$ set $k = k + 1$ and goto 1, otherwise stop.

Remark 5.2.1. *Note that the algorithm does not necessarily terminate when the active and inactive sets stop to change. Our numerical computations show that if we take $tol = 10^{-7}$ we need around 2-5 additional iterations. The question whether the active and inactive sets remain unchanged after we reach step 6 for the first time is still open. Our numerical computations suggest that once optimal active/inactive sets are found the sets do not change any more.*

5.2.3 Numerical simulations

For anisotropies in two space dimensions one often uses the representation of $\mathbf{p} = (p_x, p_y)^T$ in polar coordinates, i.e. $\mathbf{p} = |\mathbf{p}|(\cos\theta, \sin\theta)$ where $\tan\theta = \frac{p_y}{p_x}$. Then we can write the anisotropy function $\gamma(\mathbf{p})$ as follows:

$$\gamma(\mathbf{p}) = \gamma(|\mathbf{p}|(\cos\theta, \sin\theta)) = |\mathbf{p}|\gamma(\cos\theta, \sin\theta) = |\mathbf{p}|\tilde{\gamma}(\theta).$$

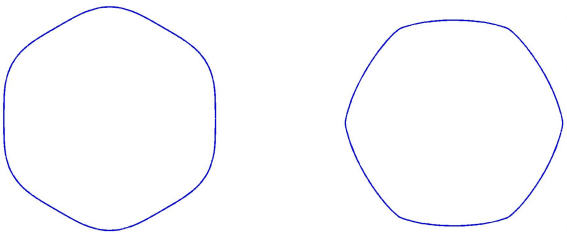

Figure 5.4: Frank diagram and Wulff shape for (5.25)

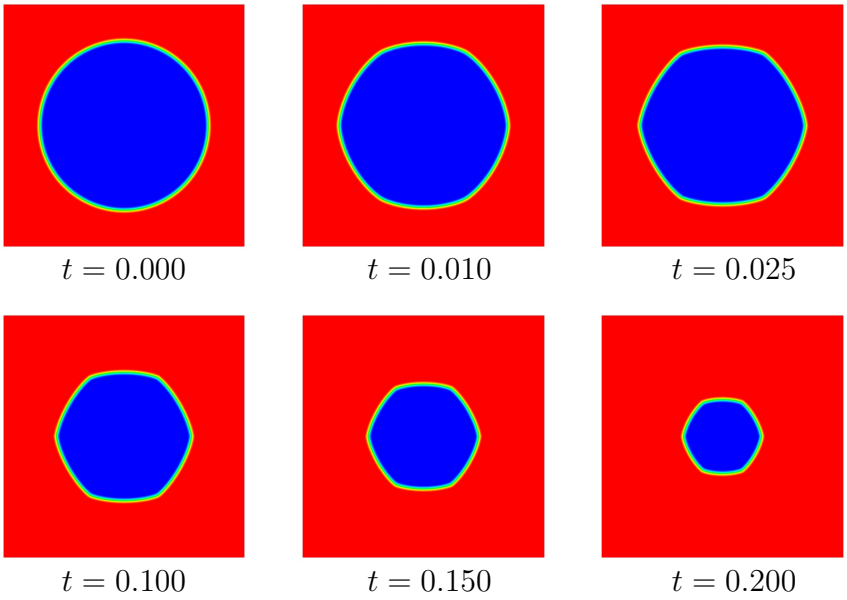

Figure 5.5: Anisotropic Allen-Cahn with anisotropy function (5.25)

For this representation the Frank diagram corresponds to the polar diagram of $\tilde{\gamma}(\theta)^{-1}$ and the Wulff shape can be parameterised as

$$x(\theta) = \tilde{\gamma}(\theta)\cos\theta - \tilde{\gamma}'(\theta)\sin\theta,$$
$$y(\theta) = \tilde{\gamma}(\theta)\sin\theta + \tilde{\gamma}'(\theta)\cos\theta,$$

see [69] for a proof of this statement and further details.
One standard example for anisotropic mean curvature flow is to take the anisotropy function

$$\tilde{\gamma}(\theta) = 1 + 0.028\cos(6\theta) \tag{5.25}$$

for which the Frank diagram and the Wulff shape are shown in Figure 5.4. We recall that $A(\mathbf{p}) = \frac{1}{2}|\mathbf{p}|^2\tilde{\gamma}^2$. We use this anisotropy for our first computation. We start with a circle of radius 0.7 which is centred at the middle of the domain $\Omega = (-1, 1)^2$. The circle quite quickly evolves into a hexagon with rounded corners, the Wulff shape of (5.25), and then shrinks, see Figure 5.5. The hexagon disappears at $t = 0.250$.

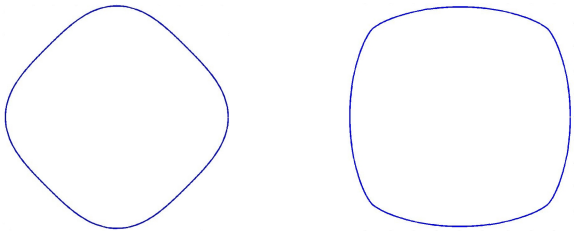

Figure 5.6: Frank diagram and Wulff shape for (5.26)

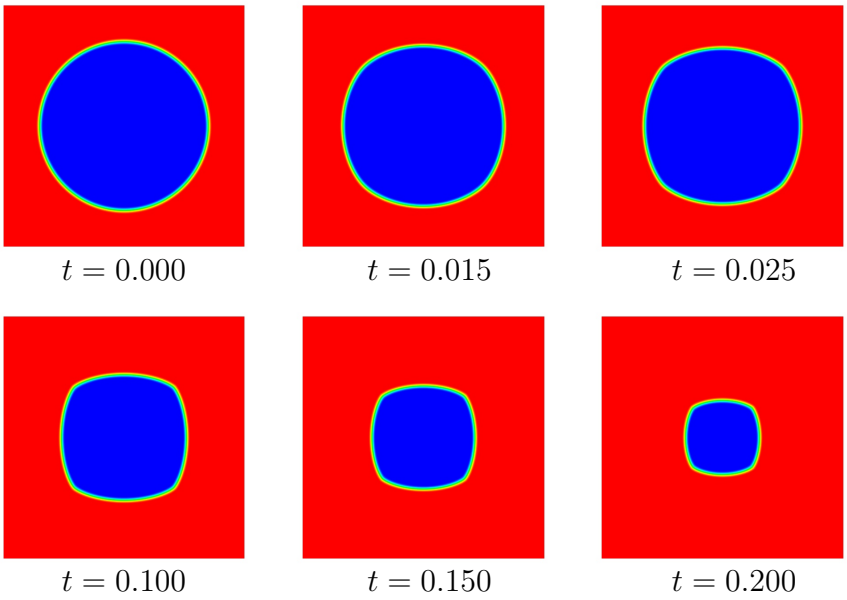

Figure 5.7: Anisotropic Allen-Cahn with anisotropy function (5.26)

For the second computation we use the anisotropy function

$$\tilde{\gamma}(\theta) = 1 - 0.06\cos(4\theta). \tag{5.26}$$

Figure 5.6 shows the Frank diagram and the Wulff shape of (5.26). This function leads to a regularised square under anisotropic mean curvature flow, see Figure 5.7. It disappears at $t = 0.253$.
For both computations we used the following set of parameters: $\varepsilon = \frac{1}{16\pi}, h_{min} = \frac{1}{512}, h_{max} = \frac{1}{32}, \tau = 1 \cdot 10^{-4}$.
The third computation is an example in three space dimensions, $\Omega = (-1, 1)^3$. For the anisotropy function we use the regularised l^1-norm

$$\gamma(\mathbf{p}) = \sum_{i=1}^{3} [\delta_1^2 |\mathbf{p}|^2 + p_i^2(1 - \delta_1^2)]^{\frac{1}{2}} \tag{5.27}$$

where we take $\delta_1 = 0.1$. The discretisation parameters are chosen to be $\tau = 1 \cdot 10^{-4}, h_{min} = \frac{1}{256}, h_{max} = \frac{1}{32}$ and we set the interfacial parameter $\varepsilon = \frac{1}{16\pi}$. We start

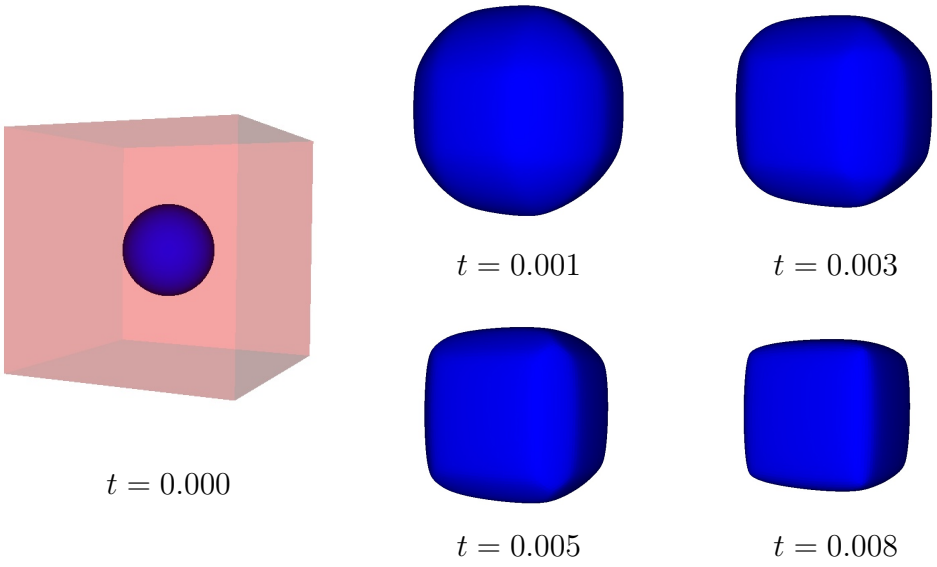

Figure 5.8: Anisotropic Allen-Cahn equation in three space dimensions

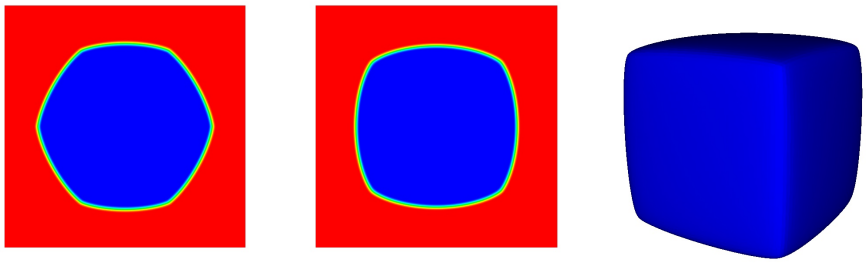

Figure 5.9: Anisotropic volume conserved Allen-Cahn for various anisotropic energy density functions γ; (5.25), (5.26) and (5.27) from left to right.

the computation with a sphere of radius 0.4 and centre at the origin. It gradually evolves into a cube with rounded edges while shrinking at the same time, see Figure 5.8.

All these computations can also be done using the volume conserved Allen-Cahn equation. In this case the Wulff shape is obtained for a fixed area/volume, i.e. that of the circle/sphere from the initial data u_0. Figure 5.9 shows the steady states obtained for the three anisotropy functions considered previously.

It is also possible to extend the vector-valued Allen-Cahn equation to the anisotropic case [58]. Here one could also consider the materials to have different anisotropic behaviours. This however remains to be studied.

5.3 Image processing

Image processing is used to preprocess an image and convert it into a form more suitable for further analysis. Examples of such operations include reduction of image

noise, increasing sharpness, detecting contours of objects in the image but also filling in missing information. In this section we will discuss two interesting problems in image processing: image segmentation and image inpainting.
Image segmentation refers to the process of partitioning the original image into some meaningful regions. Most commonly segmentation is used to detect physical objects from images. Some of the practical application fields of image segmentation are medicine, astronomy, microscopy and face or fingerprint recognition.
Image inpainting is the process of reconstructing missing parts of damaged images based on the information obtained from the surrounding areas. Digital inpainting was inspired by the real inpainting process of image restoration artists. Important applications of digital inpainting include for example the digital restoration of ancient paintings, the restoration of aged or damaged photographs or films and text or object removal in images.

5.3.1 Image segmentation and denoising

The Mumford-Shah functional, which was first proposed in [90] as a way to pose the general problem of image segmentation, is one of the best known models in image segmentation and is the basis of many algorithms. Given a domain $\Omega \subset \mathbb{R}^2$ and an image $I : \Omega \longrightarrow \mathbb{R}$, the Mumford-Shah method seeks to partition the domain Ω into several subdomains Ω_i separated by a set K of boundaries (sometimes also referred to as edges or discontinuities). The original image I is approximated by piecewise smooth functions u on $\Omega \setminus K$ which are discontinuous along the set of edges K. The pair (K, u) is obtained by minimising the functional

$$MS(K,u) = \int_{\Omega\setminus K} |\nabla u|^2 dx + \beta \int_K d\sigma + \alpha \int_\Omega (u-I)^2 dx \tag{5.28}$$

where α and β are positive constants. The first term minimises the variation of u and promotes its smoothness, the second term minimises the length of interfaces and determines the location of the boundaries K and the third term controls the quality of the approximation of I by u. The third term is often referred to as the fidelity or fitting term. The coefficients α and β are scale and contrast parameters. An overview of the Mumford-Shah model can be found for example in [97]. In practice it has proved difficult to compute a solution to this problem. Many variations of the model have been proposed since its first formulation. Mumford and Shah themselves proposed a reduced form of the problem, the so called minimal partition problem. They restrict u to piecewise constant functions where u is constant on each connected region Ω_i. The minimising values are then the averages of I across each region Ω_i. Chan and Vese [36, 37] use a level set algorithm to minimise this

reduced Mumford-Shah problem. Phase field models and in particular the Allen-Cahn equation have also been used for image segmentation [12, 77, 53]. Recalling that the Ginzburg-Landau free energy is defined as

$$E(u) := \int_\Omega (\tfrac{\gamma\varepsilon}{2}|\nabla u|^2 + \tfrac{\gamma}{\varepsilon}\psi(u))dx$$

we note that the first term of this equation is identical (up to a scaling constant) to the first term in (5.28). The second term in the Ginzburg-Landau energy reduces the width and the length of interfaces between phases and hence has a very similar role to the second term in (5.28). In the following we will use the vector-valued Allen-Cahn equation and we combine it with fitting terms similar to the third term in (5.28). This method was proposed by Kay and Tomasi [77] and is based on the level set approach by Chan and Vese [37]. Kay and Tomasi use a multigrid algorithm to solve the modified vector-valued Allen-Cahn equation.

Modified Allen-Cahn equation for grayscale images

To introduce the basic concept of the method, let us first assume that we want to partition the original grayscale image $I : \Omega \longrightarrow [0, 1]$ into two segments. For this purpose we can use the scalar Allen-Cahn equation. For simplicity we further assume that the potential ψ is smooth with global minima at 0 and 1. For the double obstacle potential the same heuristics can be used, the only difference being that instead of the Allen-Cahn equation one obtains the Allen-Cahn variational inequality. Now consider the following functional

$$E_s(u, c_1, c_2) = \int_\Omega (\tfrac{\gamma\varepsilon}{2}|\nabla u|^2 + \tfrac{\gamma}{\varepsilon}\psi(u)) + \alpha[u(I - c_1)^2 + (1 - u)(I - c_2)^2]dx \quad (5.29)$$

where we have added two fitting terms to the Ginzburg-Landau energy. The same fitting terms have been used in [37] combined with a level set method and they can be directly related to the reduced Mumford-Shah problem.
Minimising the energy functional $E_s(u, c_1, c_2)$ with respect to u and taking the L_2–gradient flow gives the modified Allen-Cahn equation

$$\varepsilon u_t = \varepsilon\Delta u - \tfrac{1}{\varepsilon}\psi'(u) - \alpha(I - c_1)^2 + \alpha(I - c_2)^2.$$

Keeping u fixed in (5.29) and minimising $E_s(u, c_1, c_2)$ with respect to the constants c_1 and c_2 it is easy to express these constants as functions of u by

$$c_1 = \frac{\int_\Omega Iu}{\int_\Omega u} \quad \text{and} \quad c_2 = \frac{\int_\Omega I(1-u)}{\int_\Omega (1-u)}.$$

Hence these constants represent the average of I on $\operatorname{supp} u$ and $\operatorname{supp}(1-u)$ respectively. The segmented image $\tilde{I}$ is then obtained by setting

$$\tilde{I} = c_1 u + c_2(1-u)$$

where u can be rounded such that it only attains values of 0 and 1. This is also called the 'rounded composite'.
In order to achieve a simultaneous segmentation of the image I into $N \geq 2$ pieces we use the vector-valued Allen-Cahn model introduced in Chapter 3. Similar to (5.29) we add a fidelity term to the free energy (3.1) and obtain

$$E_s(\boldsymbol{u}) := \int_\Omega \left(\tfrac{\gamma\varepsilon}{2}|\nabla \boldsymbol{u}|^2 + \tfrac{\gamma}{\varepsilon}\psi(\boldsymbol{u}) + \alpha \boldsymbol{u} \cdot \boldsymbol{F}(\boldsymbol{c}, I) \right) dx \tag{5.30}$$

where

$$F_i(\boldsymbol{c}, I) = (I - c_i)^2, \;\; c_i = \frac{\int_\Omega I u_i}{\int_\Omega u_i} \;\; \text{for all } i = 1, ..., N. \tag{5.31}$$

In the following we treat the variables c_i for $i = 1, ..., N$ as constants, since otherwise the first variation of the last term in the energy $E_s(\boldsymbol{u})$ would lead to additional terms in (5.32). Taking the L^2–gradient flow of the energy $E_s(\boldsymbol{u})$ and taking ψ to be the multi-obstacle potential as defined in (3.2) with W being the identity matrix we obtain the following variational inequality:

$$\varepsilon(\tfrac{\partial \boldsymbol{u}}{\partial t}, \boldsymbol{\chi} - \boldsymbol{u}) + \gamma\varepsilon(\nabla \boldsymbol{u}, \nabla(\boldsymbol{\chi} - \boldsymbol{u})) - \tfrac{\gamma}{\varepsilon}(\boldsymbol{u}, \boldsymbol{\chi} - \boldsymbol{u}) + \alpha(\boldsymbol{F}(\boldsymbol{c}, I), \boldsymbol{\chi} - \boldsymbol{u}) \geq 0 \tag{5.32}$$

which has to hold for almost all t and all $\boldsymbol{\chi} \in \mathcal{G}$.
We discretise (5.32) in time using an implicit Euler scheme. We assume that the constants c_i for $i = 1, ..., N$ in the fidelity term are known. More precisely, we update $\boldsymbol{c}$ in each time-step iteration after having computed $\boldsymbol{u}^n$ and use the updated $\boldsymbol{c}$ in the next time-step $n+1$. For the discretisation in space we use piecewise linear finite elements as before. Furthermore, we introduce Lagrange multipliers $\boldsymbol{\mu}$ and Λ for the inequality constraints $\boldsymbol{u} \geq \boldsymbol{0}$ and the sum constraint $\sum_{i=1}^N u_i = 1$ of the vector-valued Allen-Cahn equation. Taking a fixed time-step $\tau = t_n - t_{n-1}$ we obtain the following problem:
Find $\boldsymbol{u}_h = \boldsymbol{u}_h^n \in \boldsymbol{S}_h$, $\boldsymbol{\mu}_h \in \boldsymbol{S}_h$, *and* $\Lambda \in S_h$ *such that*

$$\begin{aligned} \tfrac{\varepsilon^2}{\tau}(\boldsymbol{u}_h, \boldsymbol{\varphi})_h - \gamma(\boldsymbol{u}_h, \boldsymbol{\varphi})_h + \gamma\varepsilon^2(\nabla \boldsymbol{u}_h, \nabla \boldsymbol{\varphi}) - (\boldsymbol{\mu}_h, \boldsymbol{\varphi})_h - (\Lambda \mathbf{1}, \boldsymbol{\varphi})_h \\ = \tfrac{\varepsilon^2}{\tau}(\boldsymbol{u}_h^{n-1}, \boldsymbol{\varphi})_h - \alpha(\boldsymbol{F}(\boldsymbol{c}, I_h), \boldsymbol{\varphi}) \quad \forall \boldsymbol{\varphi} \in \boldsymbol{S}_h \,, \end{aligned} \tag{5.33}$$

$$\sum_{i=1}^N (u_i)_j = 1, \;\; \boldsymbol{\mu}_j \geq 0, \;\; \boldsymbol{u}_j \geq 0, \;\; (\boldsymbol{u}_j, \boldsymbol{\mu}_j) = 0 \quad \forall \; j \in \mathcal{J} \tag{5.34}$$

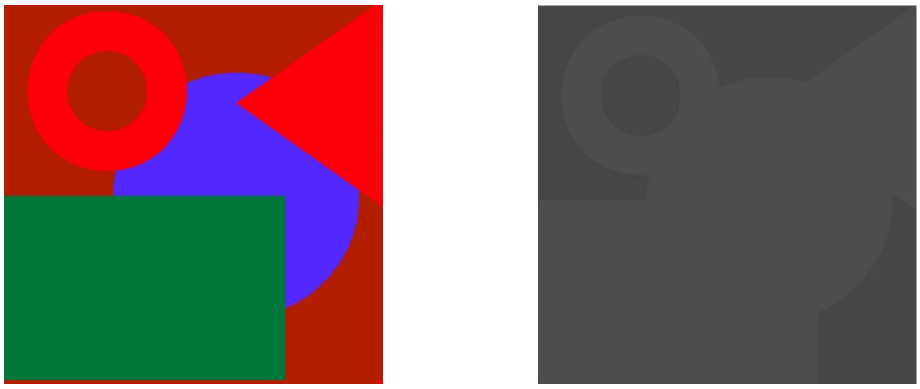

Figure 5.10: Colour image and corresponding grayscale image, converted using the MATLAB routine rgb2gray

where

$$F_i(\boldsymbol{c}, I_h) = (I_h - c_i)^2, \quad c_i = \frac{\int_\Omega I_h (u_h^{n-1})_i}{\int_\Omega (u_h^{n-1})_i} \quad \text{for all } i = 1, ..., N.$$

For this problem we can apply the primal-dual active set method for the vector-valued Allen-Cahn variational inequality as introduced in Chapter 3.
For the post-processing it is useful to round the values of all the components of $\underline{\boldsymbol{u}}$ such that one of them (the dominant component) equals 1 and all the others are set to equal 0 at any given node $j \in \mathcal{J}$. The rounded composite $\tilde{I}$ is then obtained by taking

$$\tilde{I}_j = \sum_{i=1}^{N} c_i (u_i)_j$$

at each node $j \in \mathcal{J}$.

Segmentation of colour images

Most of the pictures and photographs we are dealing with are coloured. While it is possible to transform them into a grayscale image some information will get lost and in the worst case segments get lost, see Figure 5.10.
Colour images can be represented in different colour spaces, the most common one being the RGB colour space. We only consider RGB images but in principle the method is not limited to this space. In the RGB space, colour is represented by the RGB triplets; any colour in the gamut of the RGB colour space can be created by mixing a certain amount of red, green and blue light. Hence a colour image has 3 data channels, each of which can be thought of as a 'grayscale' image. It may seem natural to perform the image segmentation on each channel individually, but this does not take into account that the information from each channel has a certain correlation. Another problem would be how to combine the resulting three

segmentations.
There has been some work on colour image segmentation using PDEs. A model introduced by Meyer [88] for grayscale image segmentation has been extended to colour image segmentation by Aujol and Kang [5]. Tomasi and Kay [77] modified the fidelity term in the modified vector-valued Allen-Cahn equation to take into account multi channel data. We will follow their approach.
Let $\mathbf{I} : \Omega \longrightarrow [0,1]^d$ be an image with $d > 1$ data channels or colours. Tomasi and Kay [77] proposed to incorporate the multi-channel information into the modified vector-valued Allen-Cahn model by modifying the fidelity term (5.31) as follows

$$F_i(\mathbf{c}, \mathbf{I}) = \sum_{l=1}^{d} (I_l - c_{il})^2, \; c_{il} = \frac{\int_\Omega I_l u_i}{\int_\Omega u_i} \quad \text{for all } i = 1, ..., N. \tag{5.35}$$

We can use the same discretisation as for the grayscale image segmentation and apply the primal-dual active set method to obtain the segments $u_1, ..., u_N$. For the post-processing we find the dominant phase in each node and we set it to 1 while all the other phases are set to 0. Then we get for each channel $l = 1, ..., d$ the rounded composite $\tilde{I}_l$

$$(\tilde{I}_l)_j = \sum_{i=1}^{N} c_{il} (u_i)_j$$

for all $j \in \mathcal{J}$.

Numerical examples for image segmentation

The first computation is a grayscale image consisting of two concentric circles. About 60% of random noise with amplitude 0.15 was added to the original image. We use the modified vector-valued Allen-Cahn equation with $N = 3$ to perform the segmentation. Figure 5.11 shows the original image, the 3 segments and the rounded composite. The noise has been removed completely during the segmentation process. The parameters for this computation are chosen as follows: $\varepsilon = \frac{1}{16\pi}, \gamma = 1, \tau = 1 \cdot 10^{-4}, h_{min} = \frac{1}{512}, h_{max} = \frac{1}{64}, \alpha = 2000$. The steady state is attained after 32 time-steps at $t = 0.0032$. We use an adaptive mesh as before with the only difference being that for the image data we do not use interpolation when we refine but use a projection instead where a newly created node is assigned the value of one of its neighbours. This is done to avoid creating spurious gradients, see [77] for details. Tomasi and Kay [77] also propose to use a more natural length scale and set ε to be the size of a pixel. We found that we did not need this in our computations.
As initial data for the order parameters u_1, u_2 and u_3 we use information from the original image. Since the original image itself already consists of values between 0 and 1 we took u_1 to equal a half of the value of I at the corresponding node,

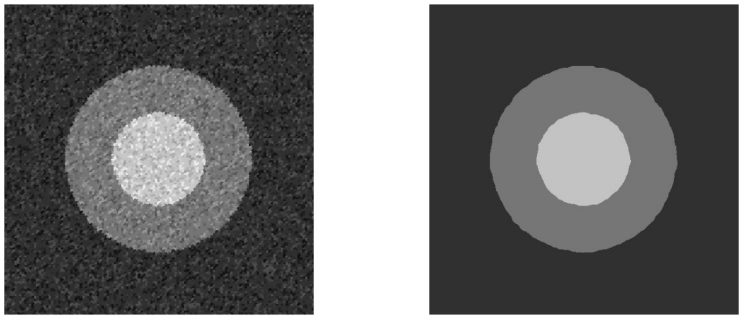

Original image (left) and rounded composite (right)

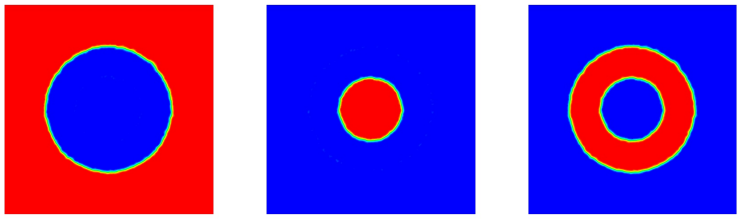

Segmentation result for $N = 3$

Figure 5.11: Segmentation of two concentric circles.

and we set $u_2 = 1.5u_1$ and $u_3 = 1.0 - u_1 - u_2$. This is somehow ad hoc and other choices work as well. One could also start with random data for $\boldsymbol{u}$ as long as the components sum up to 1 in each node. However, when we did this the computations took longer and sometimes the image was not segmented properly, i.e. one of the order parameters converged to 0 everywhere. For our choice of initial data this does not happen. Moreover, the constants c_1, c_2 and c_3 are, with this choice of initial data, sufficiently different such that the corresponding phases converge to the gray-value closest to these constants. This is also why constant initial data, i.e. setting $u_1 \equiv \frac{1}{3}$ is not suitable and may not lead to a satisfactory result.

For the next computation we use a colour image where we added about 50% of random noise with amplitude 0.15 (where the values of the image have been converted to be in the space $[0, 1]^3$). We use $N = 4$ and set the other parameters to be $\varepsilon = \frac{1}{16\pi}, \gamma = 1, \tau = 1 \cdot 10^{-4}, h_{min} = \frac{1}{512}, h_{max} = \frac{1}{64}$ and $\alpha = 8000$. Figure 5.12 shows the segmentation we obtained using the modified vector-valued Allen-Cahn model. All the segments are identified correctly and the colours match the original picture, see Figure 5.10 (left). The steady state is obtained at about $t = 0.020$, i.e. after 200 time-step iterations. However, a very good segmentation is already obtained much earlier after about 30 - 50 time-steps.

For the third computation we use a 'real' colour image and set $N = 10$. We obtain good segmentations (see Figure 5.13) using the following set of parameters for the Allen-Cahn equation: $\varepsilon = \frac{1}{16\pi}, \gamma = 1, \tau = 1 \cdot 10^{-4}, h_{min} = \frac{1}{256}, h_{max} = \frac{1}{64}$. We use two different values for the parameter α and obtain two segmentations that are roughly similar, but do have some differences. For larger α finer structures can be detected

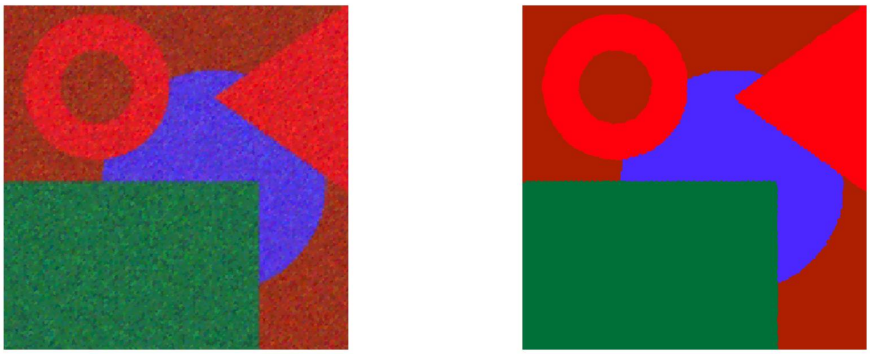

Original noisy image (left) and rounded composite (right)

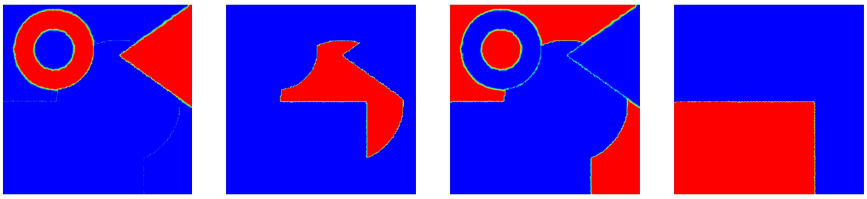

Segmentation result for $N = 4$

Figure 5.12: Segmentation of a noisy colour image.

and the colours seem a bit more realistic whereas for smaller α the segmentation is coarser. Depending on the purpose of the segmentation one can tune the parameter α such that one obtains a more suitable segmentation. Both segmentations were obtained at $t = 0.025$ after 250 iterations.

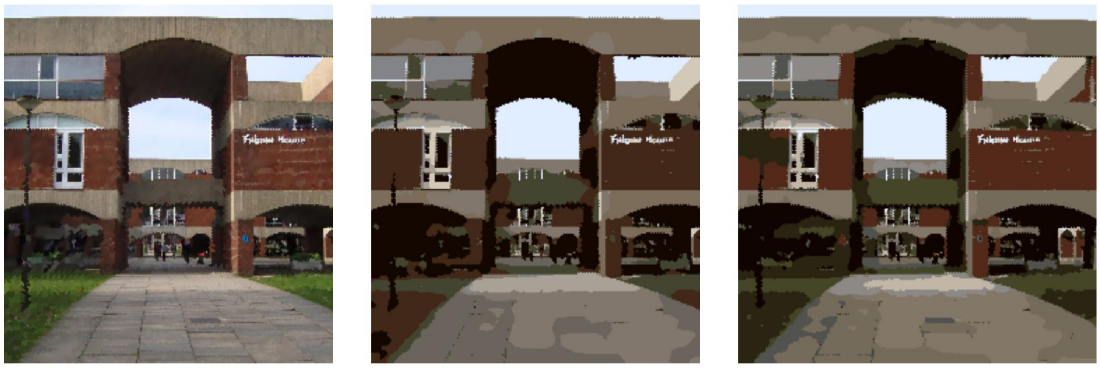

Figure 5.13: Original image (left) and rounded composite for $\alpha = 20000$ (middle) and $\alpha = 30000$ (right).

For the initial data we use a similar method as for the grayscale image. The image $\mathbf{I}$ consists of three channels I_r, I_g, I_b, each of which can be interpreted as a grayscale image. First we take the average over these three channels and then we take suitable fractions of this average to be the initial data for u_i for $i = 1, ..., N-1$. We need to set u_N such that the sum of all the components of $\boldsymbol{u}$ adds up to 1. We found that

this method works well and convergence was achieved reasonably quickly. Other choices of initial data are of course possible.
One of the drawbacks of the method is that sometimes even small changes in colour (for example sun versus shade) are detected as different segments and the difference between the colours becomes exaggerated. Another problem is that for the current formulation of the segmentation algorithm one has to specify the number of segments in advance. It would of course be desirable to have an algorithm that can change the number of segments depending on the processed image.

5.3.2 Inpainting

Image inpainting is the filling in of damaged or missing parts of an image with the use of information from the surrounding areas. Given an image $I : \Omega \longrightarrow \mathbb{R}$, the problem is to reconstruct the original image u in the damaged domain $D \subset \Omega$ which is called the inpainting domain. We are especially interested in non-texture inpainting, i.e. the inpainting of structures like edges and uniformly coloured areas in the image rather than texture.
Image inpainting for digital image processing was first introduced by Bertalmio et al. [17]. They used partial differential equations to extend the graylevels at the boundary of the damaged domain continuously into the interior. They used the nonlinear partial differential equation $u_t = \nabla^{\perp} u \cdot \nabla \Delta u$ which is solved inside the inpainting domain D using information from a small strip around D. In subsequent works variational models have been used which were originally derived for image denoising, deblurring and segmentation. In contrast to previous approaches these variational algorithms are applied to the whole domain Ω and hence several damaged domains in the image can be dealt with simultaneously. The general form for such a variational approach is

$$\min_{u \in B_1} \left(J(u) = R(u) + \tfrac{1}{2} \|\alpha(I-u)\|^2_{B_2} \right), \tag{5.36}$$

where B_1 and B_2 are Banach spaces on Ω, $R : B_1 \longrightarrow \mathbb{R}$ is a regularising term and α is the characteristic function of $\Omega \setminus D$ multiplied by a large constant. Depending on the choice of the regularising term $R(u)$ and the spaces B_1 and B_2 various approaches have been developed. The best known model is the total variation (TV) model, where $R(u) = \int_\Omega |\nabla u| dx$ is the total variation of u, $B_2 = L^2(\Omega)$ and B_1 is the space of functions of bounded variations, see e.g. [105, 104, 35]. Other variational models are for example the Euler elastica model [38], the active contour model [114] which is based on the Mumford-Shah segmentation problem, but also higher order variational approaches. A third order approach is the Curvature Driven Diffusion method [34] which performs very well at connecting level lines across a large inpainting domain.

The fourth order Cahn Hilliard equation has also been used successfully [18, 29]. We use the Allen-Cahn equation as the regularising term and it turns out that the results we obtain are comparable to the ones obtained for the Cahn-Hilliard approach whilst being more cost efficient. For an overview and a comparison of the most common mathematical models for local non-texture image inpainting the reader is referred to [33, 18].

Modified Allen-Cahn equation

Instead of using the fourth-order Cahn-Hilliard equation we propose to use the Allen-Cahn equation. We take the Ginzburg-Landau free energy as the regularising term $R(u)$ in (5.36) and obtain

$$J(u) = \int_\Omega \tfrac{\varepsilon}{2}|\nabla u|^2 + \tfrac{1}{\varepsilon}\psi(u) + \tfrac{1}{2}|\alpha(I-u)|^2 dx,$$

where α is defined as

$$\alpha(x) = \begin{cases} 0 & \text{if} \quad x \in D\,, \\ \alpha_0 & \text{if} \quad x \in \Omega \setminus D\,. \end{cases}$$

Minimising this functional using an L^2 gradient flow and taking ψ to be the double obstacle potential leads to the modified Allen-Cahn problem

Find $u \in H^1(\Omega_T)$ such that $u(.,0) = u_0$, $|u| \leq 1$ a.e. in Ω_T and

$$\varepsilon(\partial_t u, \chi - u) + \varepsilon(\nabla u, \nabla(\chi - u)) + \tfrac{1}{\varepsilon}(\psi_0'(u), \chi - u) - (\alpha(I-u), \chi - u) \geq 0 \quad (5.37)$$

which has to hold for almost all t and all $\chi \in H^1(\Omega)$ with $|\chi| \leq 1$.
We can discretise this problem in time using an implicit Euler scheme and in space using linear finite elements and then we are in the situation where we can apply the primal-dual active set strategy. This is straight forward and is therefore omitted.

Numerical examples for image inpainting

First we present some computations for binary images, i.e. most of the image is black and white. Since we have defined the double obstacle potential to have local minima at -1 and 1 we rescale grayscale (and binary) images such that $I : \Omega \longrightarrow [-1, 1]$. Alternatively, we could change the potential to have local minima at 0 and 1.
For the initial value u_0 one can choose $u_0 \equiv I$ on $\Omega \setminus D$ and $u_0 \equiv 0$ on D. For the inpainting of binary images we set $\varepsilon = \frac{1}{32\pi}, \tau = 1 \cdot 10^{-5}$, and $\alpha_0 = 10^5$. The element size in the adaptive mesh is set to have the maximal diameter of all elements $h_{max} = \frac{1}{64}$ and the minimal diameter of all elements $h_{min} = \frac{1}{512}$.

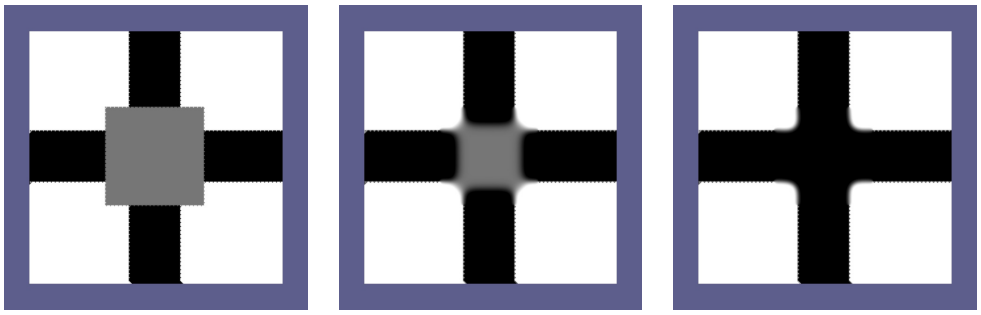

Figure 5.14: Original image with inpainting region in gray (left), intermediate inpainting result after 40 time-step iterations (middle) and final inpainting result after 100 time step iterations (right).

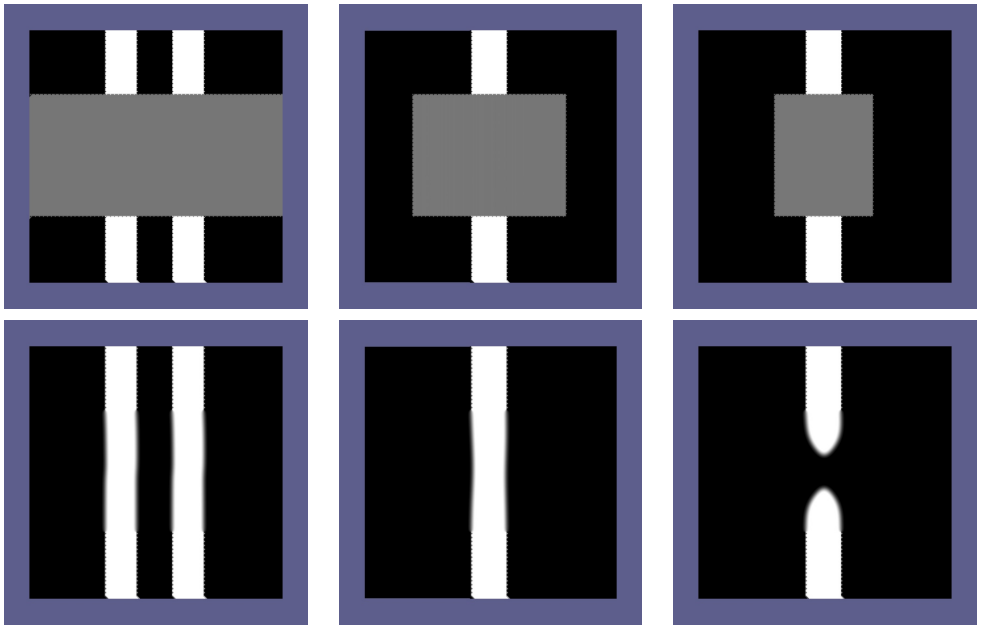

Figure 5.15: First row: Original images with inpainting region in gray; Second row: Inpainting results obtained after 150 time-step iterations (left picture), 500 time-step iterations (middle picture), 110 time-steps (right picture).

Figure 5.14 shows how the inpainting algorithm works. The gray region in the left picture represents the inpainting domain. Gradually the image is 'inpainted' from the boundary towards the middle of the inpainting region. The picture on the right is obtained after 100 time-step iterations.
Figure 5.15 shows some further inpainting computations. In each of the three computations the gray region denotes the inpainting region. For the first two computations the algorithm works very well and combines the lines. In the last computation the inpainting region is not wide enough and the algorithm does not manage to connect the line. One could of course set a new inpainting region over the area where the line is dissected and use the inpainting algorithm again. This effect is known to occur for TV inpainting and other second order variational approaches. The Curvature Driven Diffusion method by Chen and Shen [34] overcomes this problem by modify-

ing the TV inpainting model such that large curvatures inside the inpainting domain are penalised.

The examples presented above have also been used in [18, 29] where a modified Cahn-Hilliard model is applied. The results are comparable to our results, however, in general more iterations are needed for the Cahn-Hilliard approach. For the inpainting of the cross in Figure 5.14 the Cahn-Hilliard approach needs 1000 time-step iterations in [18] and 1200 iterations in [29]. However, with the Cahn-Hilliard approach a steady state is reached which is not always the case with the Allen-Cahn model - at least one may not obtain the best inpainting result. For the first two straight line examples in Figure 5.15 the inpainting result corresponds to the steady state. For the third computation in that figure the segments keep moving further away and a steady state is reached when the gap between the two segments is about the size of the original inpainting domain. For the inpainting of the cross the movement also continues and the corners in the middle of the cross become more rounded (which does also happen with the Cahn-Hilliard method). In contrast to the Cahn-Hilliard model the Allen-Cahn model we are using does not preserve mass. Outside the inpainting region this mass constraint is not necessary since variations from the original image are penalised. Inside the inpainting domain mass conservation is only useful when it is known in advance how much mass there should be, which of course is not the case. One way out of this could be to use the Allen-Cahn model as we did in this section and to enforce a volume constraint once the inpainting region is filled. Depending on the size of the inpainting region one could roughly estimate how long it will take to inpaint it.

Another difference in the Cahn-Hilliard approach is that a two-step method is used. First the interfacial parameter ε is chosen relatively large in order to reconnect shapes across larger regions. The second step uses the results of the first step and continues the computation with a much smaller value of ε in order to sharpen the edges. We found that we did not need a two-step method. Even with ε small the algorithm managed to reconnect shapes across relatively large regions.

Both the Allen-Cahn and the Cahn-Hilliard model are very well suited for binary images where the two local minima in the potential are chosen to correspond to the two colours. A practical application of binary image inpainting is the deconvolution of barcodes [52]. The data obtained from scanning is incomplete and noisy and hence needs to be recovered. For grayscale images this approach can still be used but might not always give the best results. In [29] the authors suggest a modified TV model for grayscale images where the H^{-1} norm is used to minimise the TV term.

We use the same Allen-Cahn approach as for binary images and show two examples of grayscale image inpainting. For the first computation we use a picture of Beachy

Head. The light house has been marked on the picture with a black circular line. We would like to remove this marking and restore the original picture. Using the time-step $\tau = 1 \cdot 10^{-5}$, the mesh size $h_{min} = \frac{1}{512}$ and $h_{max} = \frac{1}{64}$ and the fidelity parameter $\alpha_0 = 1000$ we obtain the inpainting result shown in Figure 5.16. For the interfacial parameter we use two values, we set $\varepsilon = \frac{1}{16\pi}$ for $t \leq 7 \cdot 10^{-5}$ and $\varepsilon = \frac{1}{32\pi}$ for $t > 7 \cdot 10^{-5}$. The inpainting result in Figure 5.16 is obtained after only 10 time-steps. The initial data in the inpainting domain is set to be 0 where we have transformed the picture to have values between -1 and 1.

Figure 5.16: Original image with inpainting (or damaged) region in black (left) and inpainting result after 10 time-step iterations (right).

For the second computation we use a picture with black text written on it. We want to remove the text and set the inpainting domain to be exactly the space filled by the text. Time step and mesh sizes are the same as before and we use again $\alpha_0 = 1000$. This time we switch from $\varepsilon = \frac{1}{16\pi}$ to the smaller interfacial parameter $\varepsilon = \frac{1}{32\pi}$ at $t = 1.4 \cdot 10^{-4}$. Figure 5.17 shows the inpainting result at $t = 2.1 \cdot 10^{-4}$, i.e. after 21 iterations.

In both computations the inpainting domain is filled in adequately. The marking or text is removed completely and replaced by information that fits into the image. Due to the diffusion term in the Ginzburg Landau energy the image becomes a bit blurred outside the inpainting domain. One possibility to get rid of this is to take the inpainting result and only use it for the inpainting domain. For the rest of the image we can take the original image and thus get rid of the blurring. In this work we are more interested in applications of the Allen-Cahn equation and hence we do not pursue this issue further. The inpainting results we show correspond exactly to what we obtained by applying the algorithm described in this section.

Figure 5.17: Original image with black text to be removed (left) and inpainting result after 21 time-step iterations (right).

Chapter 6

Conclusions

In this thesis we used a primal-dual active set method to solve Allen-Cahn variational inequalities. One of the key advantages of this method is that it reduces the problem to solving a linear system only on the interface rather than solving a nonlinear system on the whole domain. Furthermore, we investigated linear solvers and preconditioning strategies, which improve efficiency of the proposed method. Local convergence of the method was shown analytically and in practice we found that the method converged for all of the problems we considered.

There is of course scope for further research and improvement. An adaptive time-step strategy might speed up computations further, since small time-steps only seem to be needed when the active sets change quickly. However, iterative solvers converge faster for smaller time-steps where a good initial value is provided by the previous time-step or Newton iteration.

Computations could also be accelerated by using inexact solving in Newton iterations. Recalling that the vectors $\underline{u}^k$ and $\underline{\mu}^k$ are only needed to obtain the new active and inactive sets for the next Newton iteration, they do not have to be exact. Once the optimal active sets are found $\underline{u}^k$ should be calculated more precisely. This strategy can speed up computations if one finds that $\underline{u}^k$ does not need to be too precise in order to determine the active sets correctly. For this thesis we felt that it was more important to find an efficient linear algebra solver first before considering inexact solving.

In the current version of the primal-dual active set method for solving Allen-Cahn variational inequalities we are restricted to piecewise linear finite elements since we use mass lumping. It would be interesting to investigate whether the method can be modified as to allow for higher order finite elements.

A different area for improvement is the software used for implementation. While ALBERTA has the advantage of handling adaptive finite elements, it does not provide many linear algebra solvers. Due to the matrix structure in ALBERTA the usage of most external libraries is only possible when the matrix is first converted to a dif-

ferent format. We have used external libraries and we found that although it is not difficult to combine external software packages with ALBERTA, there is still some loss in efficiency due to additional memory requirements. Instead of using space adaptivity one might also consider using a uniform mesh where mass and stiffness matrix can be calculated easily and only need minimal storage. Since the linear system is solved only on the inactive set, the dimension of this system does not increase. Even though the vectors of coefficients, $\underline{\boldsymbol{u}}, \underline{\boldsymbol{\mu}}$ and $\underline{\Lambda}$ are a lot bigger and need more storage space, they can be updated very easily on the active sets and hence should not slow down computations. Another advantage of a uniform mesh is that one not only saves the time needed to assemble the system matrix in each time-step but one also needs to initialise the preconditioner only once at the beginning of the computation. For the practical use of this strategy a suitable computational environment is needed. Since the computations in this thesis were implemented using the adaptive finite element toolbox ALBERTA we did not consider uniform meshes. Further improvements to the computation time could be made by using parallel computing. During the last decade more and more software has become available which facilitates computations in parallel. This however, was not the objective of this work and needs to be investigated in future projects.

Phase field models have been used in various areas of research. We presented some important applications where phase field models are used as regularising terms. Most of the literature in this context seems to focus on the Cahn-Hilliard equation. We showed that for some problems we can replace this fourth order equation by the second order (non-local) Allen-Cahn equation which makes computations more efficient. There are of course many other interesting problems and extensions to the classical Allen-Cahn model and we hope that with this thesis we provided an efficient method that can be extended to more general problems.

Bibliography

[1] Adams, M., Brezina, M., Hu, J., and Tuminaro, R. Parallel multigrid smoothing: polynomial versus Gauss-Seidel. *J. Comp. Phys. 188* (2003), 593–610.

[2] Allaire, G. *Optimization by the Homogenization Method.* Springer, 2002.

[3] Allaire, G., Jouve, F., and Toader, A.-M. Structural optimization using sensitivity analysis and a level-set method. *J. Comput. Phys. 194* (2004), 363–393.

[4] Allen, S., and Cahn, J. A microscopic theory for antiphase boundary motion and its application to antiphase domain coarsening. *Acta Metall. 27* (1979), 1084–1095.

[5] Aujol, J.-F., and Kang, S. Color image decomposition and restoration. *J. Vis. Commun. Image Represent. 17*, 4 (2006), 916–928.

[6] Ayra, S., Malamatos, T., and Mount, D. M. Space-efficient approximate Voronoi diagrams. *Proc. 34th ACM Symp. on Theory of Computing* (2002), 732–730.

[7] Barrett, J. W., and Blowey, J. F. An error bound for the finite element approximation of a model for phase seperation of a multi-component alloy. *IMA J. Num. Analysis 16* (1996), 257–287.

[8] Barrett, J. W., and Blowey, J. F. Finite element approximation of a model for phase separation of a multi-component alloy with non-smooth free energy. *Num. Math. 77* (1997), 11–34.

[9] Barrett, J. W., Nürnberg, R., and Styles, V. Finite element approximation of a phase field model for void electromigration. *SIAM J. Num. Analysis 42* (2004), 738–772.

[10] Bellettini, G., and Paolini, M. Anisotropic motion by mean curvature in the context of Finsler geometry. *Hokkaido Math. J. 25* (1996), 537–566.

[11] Bellettini, G., Paolini, M., and Verdi, C. γ-convergence of discrete approximations to interfaces with prescribed mean curvature. *Rend. Atti. Naz. Linci.* (1990).

[12] Beneš, M., Chalupecký, V., and Mikula, K. Geometrical image segmentation by the Allen-Cahn equation. *Appl. Num. Math. 51* (2004), 187–205.

[13] Bensoe, M., and Sigmund, O. *Topology Optimization.* Springer, 2003.

[14] Benzi, M., Golub, G. H., and Liesen, J. Numerical solution of saddle point problems. *Acta Numer. 14* (2005), 1–137.

[15] Bergounioux, M., Ito, K., and Kunisch, K. Primal-dual strategy for constrained optimal control problems. *SIAM J. Control Optim. 37*, 4 (1999), 1176–1194.

[16] Bergounioux, M., and Kunisch, K. Primal-dual active set strategy for state constrained optimal control problems. *Comput. Optim. Appl. 22*, 2 (2002), 193–224.

[17] Bertalmio, M., Sapiro, G., Caselles, V., and Ballester, C. Image inpainting. In *Siggraph 2000, Computer Graphics Proceedings* (2000), ACM Press/Addison Wesley Longman, pp. 417–424.

[18] Bertozzi, A., Esedoglu, S., and Gillette, A. Inpainting of binary images using the Cahn-Hilliard equation. *IEEE Trans. Image Proc. 16*, 1 (2007), 285–291.

[19] Blank, L., Butz, M., and Garcke, H. Solving the Cahn-Hilliard variational inequality with a semi-smooth Newton method. Preprint SPP1253-09-02, to appear in ESAIM: COCV.

[20] Blank, L., Garcke, H., Sarbu, L., Srisupattarawanit, T., Styles, V., and Voigt, A. Phase-field approaches to structural topology optimization. To be pubished in: Hoffmann, K. H., and Leugering, G. (Eds): Optimization with Partial Differential Equations, Birkhäuser, 2010.

[21] Blank, L., Garcke, H., Sarbu, L., and Styles, V. Primal-dual active set methods for Allen-Cahn variational inequalities with non-local constraints. Submitted, Preprint SPP1253-09-01.

[22] Blank, L., Sarbu, L., and Stoll, M. Preconditioning for Allen-Cahn variational inequalities with non-local constraints. Submitted, Preprint 11/2010, University of Regensburg.

[23] Blowey, J. F., and Elliott, C. M. The Cahn-Hilliard gradient theory for phase separation with non-smooth free energy. I: Mathematical analysis. *European J. Appl. Math. 2*, 3 (1991), 233–280.

[24] Blowey, J. F., and Elliott, C. M. The Cahn-Hilliard gradient theory for phase separation with non-smooth free energy. II: Numerical analysis. *European J. Appl. Math. 3* (1992), 147–179.

[25] Blowey, J. F., and Elliott, C. M. Curvature dependent phase boundary motion and parabolic double obstacle problems. *IMA Vol. Math. Appl. 47* (1993), 19–60.

[26] Braess, D. *Finite Elemente*, 3 ed. Springer, 2003.

[27] Brandt, A., McCormick, S., and Ruge, J. *Sparsity and its applications*. Cambridge University Press, 1984, ch. Algebraic multigrid (AMG) for sparse matrix equations.

[28] Bronsard, L., and Reitich, F. On three-phase boundary motion and the singular limit of a vector-valued Ginzburg-Landau equation. *Arch. Rat. Mech. Anal. 124* (1993), 355–379.

[29] Burger, M., He, L., and Schönlieb, C.-B. Cahn-Hilliard inpainting and a generalization for grayvalue images. *SIAM J. Imaging Sci. 2*, 4 (2009), 1129–1167.

[30] Burger, M., and Stainko, R. Phase-field relaxation of topology optimization with local stress constraints. *SIAM J. Control Optim. 45* (2006), 1447–1466.

[31] Caginalp, G., and Socolovsky, E. Phase field computations of single-needle crystals, crystal growth, and motion by mean curvature. *SIAM J. Scientific Comp. 15* (1994), 106–126.

[32] Cao, F. *Geometric Curve Evolution and Image Processing*. No. 1805 in Lecture Notes in Mathematics. Springer, 2003.

[33] Chan, T., and Shen, J. Mathematical models for local non-texture inpaintings. *SIAM J. Appl. Math. 62*, 3 (2001), 1019–1043.

[34] Chan, T., and Shen, J. Non-texture inpainting by curvature driven diffusions (CDD). *J. Visual Comm. Image Rep. 12*, 4 (2001), 436–449.

[35] Chan, T., and Shen, J. Variational restoration of non-flat image features: models and algorithms. *SIAM J. Appl. Math. 61*, 4 (2001), 1338–1361.

[36] Chan, T., and Vese, L. Image segmentation using level sets and the piecewise-constant Mumford-Shah model. Tech. rep., 00-14, UCLA, 2000.

[37] Chan, T., and Vese, L. Active contours without edges. *IEEE Trans. Image Process. 10*, 2 (2001), 266–277.

[38] Chan, T. F., Kang, S. H., and Shen, J. Euler's elastica and curvature-based inpainting. *SIAM J. Appl. Math. 63*, 2 (2002), 564–592.

[39] Chen, X., Elliott, C. M., Gardiner, A. R., and Zhao, J. J. Convergence of numerical solutions to the Allen-Cahn equation. *Applicable Analysis 69* (1998), 47–56.

[40] Chen, X., Nashed, Z., and Qi, L. Smoothing methods and semismooth methods for nondifferentiable operator equations. *SIAM J. Numer. Anal. 38*, 4 (2001), 1200–1216.

[41] Davis, T. A. *UMFPACK Version 5.2.0 User Guide.* University of Florida, November 2007.

[42] Davis, T. A., and Duff, I. *An unsymmetric-pattern multifrontal method for sparse LU factorization.* Rutherford Appleton Laboratory, 1993.

[43] Deckelnick, K., Dziuk, G., and Elliott, C. M. Computation of geometric partial differential equations and mean curvature flow. *Acta Numerica 14* (2005), 139–232.

[44] Dolcetta, I. C., Vita, S. F., and March, R. Area-preserving curve-shortening flows: from phase separation to image processing. *Interfaces Free Bound. 4* (2002), 325–343.

[45] Elliott, C. M. Approximation of curvature dependent interface motion. In *State of the Art in Numerical Analysis* (1997), I. Duff and G. A. Watson, Eds., Clarendon Press, Oxford, pp. 407–440.

[46] Elliott, C. M., and Gardiner, A. R. Double obstacle phase field computations of dendritic growth. *University of Sussex CMAIA Research report 96-19* (1996).

[47] Elliott, C. M., and Luckhaus, S. A generalised diffusion equation for phase separation of a multi-component mixture with interfacial free energy. SFB256 University Bonn, Preprint 195, 1999.

[48] Elliott, C. M., and Ockendon, J. R. *Weak and variational methods for moving boundary problems.* Pitman, London, 1982.

[49] Elliott, C. M., and Schätzle, R. The limit of the anisotropic double-obstacle Allen-Cahn equation. *Proc. Roy. Soc. Edinburgh 126* (1996), 1217–1234.

[50] Elliott, C. M., and Styles, V. Computations of bi-directional grain boundary dynamics in thin films. *J. Comput. Phys. 187* (2003), 524–543.

[51] Elman, H. C., Silvester, D. J., and Wathen, A. J. *Finite elements and fast iterative solvers: with applications in incompressible fluid dynamics.* Numerical Mathematics and Scientific Computation. Oxford University Press, New York, 2005.

[52] Esedoglu, S. Blind deconvolution of bar code signals. *Inverse Problems 20* (2004), 121–135.

[53] Esedoglu, S., and Tsai, Y.-H. Threshold dynamics for the piecewise constant Mumford-Shah functional. *J. Comput. Phys. 211*, 1 (2006), 367–384.

[54] Evans, L. C. *Partial Differential Equations.* AMS, 1998.

[55] Falgout, R. An introduction to algebraic multigrid. Tech. Rep. UCRL-JRNL-220851, LLNL, 2006.

[56] Garcke, H., Ito, K., and Kohsaka, Y. Linearized stability analysis of stationary solutions for surface diffusion with boundary conditions. *SIAM J. Math. Anal. 36*, 6 (2005), 1031–1056.

[57] Garcke, H., Nestler, B., Stinner, B., and Wendler, F. Allen-Cahn systems with volume constraints. *Math. Models Methods Appl. Sci. 18*, 8 (2008), 1347–1381.

[58] Garcke, H., Nestler, B., and Stoth, B. On anisotropic order parameter models for multi–phase systems and their sharp interface limits. *Physica D 115* (1998), 87–108.

[59] Garcke, H., Nestler, B., and Stoth, B. A multi phase field concept: Numerical simulations of moving phase boundaries and multiple junctions. *SIAM J. Appl. Math. 60* (1999), 295–315.

[60] Garcke, H., Nürnberg, R., and Styles, V. Stress and diffusion induced interface motion: Modelling and numerical simulations. *European J. Applied Math. 18* (2007), 631–657.

[61] Garcke, H., and Styles, V. Bi-directional diffusion induced grain boundary motion with triple junctions. *Interfaces and Free Boundaries 6*, 3 (2004).

[62] Garcke, H., and Weikard, U. Numerical approximation of the Cahn-Larché equation. *Numer. Math. 100* (2005), 639–662.

[63] Gee, M., Siefert, C., Hu, J., Tuminaro, R., and Sala, M. ML 5.0 smoothed aggregation user's guide. Tech. Rep. SAND2006-2649, Sandia National Laboratories, 2006.

[64] Golub, G. H., and Meurant, G. Matrices, moments and quadrature. In *Numerical analysis 1993 (Dundee, 1993)*, D. F. Griffiths and G. A. Watson, Eds. Longman Sci. Tech.

[65] Gräser, C. Globalization of nonsmooth Newton methods for optimal control problems. In *Numerical Mathematics and Advanced Applications: Proceedings of ENUMATH 2007* (2008), K. Kunisch, G. Of, and O. Steinbach, Eds., Springer, pp. 605–612.

[66] Gräser, C., and Kornhuber, R. Multigrid methods for obstacle problems. *J. Comput. Math. 27* (2009), 1–44.

[67] Gräser, C., and Kornhuber, R. Nonsmooth Newton methods for set-valued saddle point problems. *SIAM J. Numer. Anal. 47*, 2 (2009), 1251–1273.

[68] Grisvard, P. *Elliptic problems in nonsmooth domains*. Pitman, 1985.

[69] Gurtin, M. E. *Thermomechanics of evolving phase boundaries in the plane*. Clarendon Press, Oxford, 1993.

[70] Haber, R., Jog, C., and Bensøe, M. A new approach to variable topology shape design using a constraint on perimeter. *Struct. Multidisc. Optim. 11* (1996), 1–12.

[71] Heroux, M., Bartlett, R., Howle, V., Hoekstra, R., Hu, J., Kolda, T., Lehoucq, R., Long, K., Pawlowski, R., Phipps, E., Salinger, A., Thornquist, H., Tuminaro, R., Willenbring, J., and Williams, A. An Overview of Trilinos. Tech. Rep. SAND2003-2927, Sandia National Laboratories, 2003.

[72] Hintermüller, M., Ito, K., and Kunisch, K. The primal-dual active set strategy as a semismooth Newton method. *SIAM J. Optim. 13*, 3 (2003), 865–888.

[73] Hinze, M., Pinnau, R., Ulbrich, M., and Ulbrich, S. *Optimization with PDE Constraints*. Mathematical Modelling: Theory and Applications. Springer-Verlag, New York, 2008.

[74] Hruska, C., Leykekhman, D., Pinzon, D., Shay, B., and Foisy, J. The shortest enclosure of two connected regions in a corner. *Rocky Mountain J. Math. 31*, 1 (2001), 437–482.

[75] Hutchings, M., Morgan, F., Ritore, M., and Ros, A. Proof of the double bubble conjecture. *Annals of Math. 155*, 2 (2002), 459–489.

[76] Ito, K., and Kunisch, K. Semi-smooth Newton methods for variational inequalities of the first kind. *M2AN Math. Model. Numer. Anal. 37*, 1 (2003), 41–62.

[77] Kay, D., and Tomasi, A. Colour image segmentation by the vector-valued Allen-Cahn phase-field model: a multigrid solution. *IEEE Trans. Image Proc. 18* (2007), 2330–2339.

[78] Keller, C., Gould, N., and Wathen, A. Constraint Preconditioning for Indefinite Linear Systems. *SIAM J. Matrix Anal. Appl 21*, 4 (2000), 1300–1317.

[79] Kikuchi, F., Nakazato, K., and Ushijima, T. Finite element approximation of a nonlinear eigenvalue problem related to MHD equilibria. *Japan J. Appl. Math. 1*, 2 (1984), 369–403.

[80] Kobayashi, R. Modelling and numerical simulation of dendritic crystal growth. *Physica D 63* (1993), 410–423.

[81] Kornhuber, R. Monotone multigrid methods for elliptic variational inequalities I. *Num. Math. 69* (1994), 167–184.

[82] Kornhuber, R. Monotone multigrid methods for elliptic variational inequalities I. *Num. Math. 69* (1994), 167–184.

[83] Kornhuber, R. Monotone multigrid methods for elliptic variational inequalities II. *Num. Math. 72*, 4 (1996), 481–499.

[84] Kornhuber, R., and Krause, R. On multigrid methods for vector-valued Allen-Cahn equations. In *Domain Decomposition Methods in Science and Engineering*, Herrera, I. et al., Ed. UNAM, Mexico City, Mexico, pp. 307–314.

[85] Lions, J. *Quelques Méthodes de Résolution des Problèmes aux Limites Nonlinéaires*. Dunod, 1969.

[86] McFadden, G. B., Wheeler, A. A., Braun, R. J., Coriell, S. R., and Sekerka, R. F. Phase-field models for anisotropic interfaces. *Phys. Rev. E 48*, 3 (1993), 2016–2024.

[87] Meyer, C., Rösch, A., and Tröltzsch, F. Optimal control problems of PDEs with regularized pointwise state constraints. *Comput. Optim. Appl. 33* (2006), 209–228.

[88] Meyer, Y. Oscillating patterns in image processing and nonlinear evolution equations. In *Proc. 15th Dean Jacqueline B Lewis Memorial Lectures* (2001), vol. 22 in University Lecture Series.

[89] Modica, L. The gradient theory of phase transitions and the minimal interface criterion. *Arch. Rat. Mech. Anal. 98* (1987), 123–142.

[90] Mumford, D., and Shah, J. Optimal approximation by piecewise smooth functions and associated variational problems. *Commun. Pure Appl. Math. 42* (1989), 577–685.

[91] Murphy, M. F., Golub, G. H., and Wathen, A. J. A note on preconditioning for indefinite linear systems. *SIAM J. Sci. Comput 21*, 6 (2000), 1969–1972.

[92] Neitzel, I., and Tröltzsch, F. On regularization methods for the numerical solution of parabolic control problems with pointwise state constraints. *ESAIM: COCV 15*, 2 (2009), 426–453.

[93] Nocedal, J., and Wright, S. J. *Numerical optimization*, second ed. Springer Series in Operations Research and Financial Engineering. Springer, New York, 2006.

[94] Nochetto, R. H., Paolini, M., and Verdi, C. Sharp error analysis for curvature dependent evolving fronts. *Math. Models Methods Appl. Sci. 3* (1993), 711–723.

[95] Nochetto, R. H., Paolini, M., and Verdi, C. A dynamic mesh algorithm for curvature dependent evolving interfaces. *J. Comp. Physics 123* (1996), 296–310.

[96] Petersson, J. Some convergence results in perimeter-controlled topology optimization. *Computer Meth. Appl. Mech. Eng. 171* (1999), 123–140.

[97] Petitot, J. An introduction to the Mumford-Shah segmentation model. *J. Physiol. - Paris 35*, 3 (2003), 335–342.

[98] Philip, W. E. A slight extension of Euler's theorem on homogeneous functions. In *Proc. of the Edinburgh Math. Soc.* (1900), vol. 18, pp. 101–102.

[99] Qi, H. D. A regularized smoothing newton method for box constrained variational inequality problems with p_0–functions. *SIAM J. Optim. 10* (1999), 315–330.

[100] Reed, M., and Simon, B. *Methods of modern mathematical physics I: Functional analysis.* Academic Press, 1980.

[101] Richtmyer, R. D., and Morton, K. W. *Difference Methods for initial-value problems*, 2 ed. Interscience publishers, 1967.

[102] Rodrigues, J. F., and Santos, L. On a constrained reaction-diffusion system related to multiphase problems. *Discr. cont. dyn. sys. 25*, 1 (2009), 299–319.

[103] Rubinstein, J., and Sternberg, P. Nonlocal reaction diffusion equations and nucleation. *IMA J. Appl. Math. 48* (1992), 249–264.

[104] Rudin, L. I., and Osher, S. Total variation based image restoration with free local constraints. In *Proc. 1st IEEE ICIP* (1994).

[105] Rudin, L. I., Osher, S., and Fatemi, E. Nonlinear total variation based noise removal algorithms. *Physica D 60* (1992), 259–268.

[106] Ruge, J. W., and Stüben, K. Algebraic multigrid. In *Multigrid methods*, vol. 3 of *Frontiers Appl. Math.* SIAM, Philadelphia, PA, 1987, pp. 73–130.

[107] Sarbu, L. Numerische Lösungen der Allen-Cahn Gleichung zur Simulation von Grenzflächenevolutionen. Master's thesis, University of Regensburg, Germany, 2008.

[108] Schmidt, A., and Siebert, K. G. *Design of Adaptive Finite Element Software, The Finite Element Toolbox ALBERTA.* Lecture Notes in Computational Science and Engineering. Springer, 2005.

[109] Sigmund, O., and Petersson, J. Numerical instabilities in topology optimization: A survey on procedures dealing with checkerboards, mesh-dependencies and local minima. *Struct. Multidisc. Optim. 16* (1998), 68–75.

[110] Stoll, M., and Wathen, A. Combination preconditioning and the Bramble–Pasciak$^+$ preconditioner. *SIAM J. Matrix Anal. Appl 30*, 2 (2008), 582–608.

[111] Takezawa, A., Nishiwaki, S., and Kitamura, M. Shape and topology optimization based on the phase field method and sensitivity analysis. *J. Comp. Physics 229*, 7 (2010), 2697–2718.

[112] Taylor, J., and Cahn, J. Linking anisotropic sharp and diffuse surface motion laws via gradient flows. *J. Statist. Phys. 77*, 1-2 (1994), 183–197.

[113] Tröltzsch, F. *Optimale Steuerung partieller Differentialgleichungen: Theorie, Verfahren und Anwendungen.* Vieweg Verlag, Wiesbaden, 2005.

[114] Tsai, A., Yezzi, A., and Willsky, A. Curve evolution implementation of the Mumford-Shah functional for image segmentation, denoising, interpolation and magnification. *IEEE Trans. Image Proc. 10*, 8 (2001), 1169–1186.

[115] Von Neumann, J. Metal interfaces. In *American Society for Metals* (1952), Cleveland, pp. 108–110.

[116] Wang, M., and Zhou, S. Phase field: A variational method for structural topology optimization. *Comput. Model. Eng. Sci. 6* (2004), 547–566.

[117] Wheeler, A. A., and McFadden, G. A ξ-vector formulation of anisotropic phase-field models: 3-D asymptotics. *European J. Appl. Math. 7* (1996), 367–381.

[118] Wilson, R. J. *Introduction to Graph Theory.* Pearson Education Ltd, 1996.

[119] Young, T. An essay on the cohesion of fluids. *Phil. Trans. R. Soc. Lond. 95* (1805), 65–87.

[120] Zeidler, E. *Nonlinear functional analysis and its applications IV: Applications to mathematical physics.* Springer, New York, 1988.